creative commons
COMMONS DEED

저작자표시-비영리-변경금지 2.0 대한민국

이용자는 아래의 조건을 따르는 경우에 한하여 자유롭게

- 이 저작물을 복제, 배포, 전송, 전시, 공연 및 방송할 수 있습니다.

다음과 같은 조건을 따라야 합니다:

저작자표시. 귀하는 원저작자를 표시하여야 합니다.

비영리. 귀하는 이 저작물을 영리 목적으로 이용할 수 없습니다.

변경금지. 귀하는 이 저작물을 개작, 변형 또는 가공할 수 없습니다.

- 귀하는, 이 저작물의 재이용이나 배포의 경우, 이 저작물에 적용된 이용허락조건을 명확하게 나타내어야 합니다.
- 저작권자로부터 별도의 허가를 받으면 이러한 조건들은 적용되지 않습니다.

저작권법에 따른 이용자의 권리는 위의 내용에 의하여 영향을 받지 않습니다.

이것은 이용허락규약(Legal Code)을 이해하기 쉽게 요약한 것입니다.

Disclaimer

dCollection

Ph.D. Dissertation of Engineering

Evaluation of the Hydroelasticity Effect for LNG CCS and Prediction of Sloshing Pressure

LNG CCS에 대한 유탄성 효과 평가 및 슬로싱 하중 예측에 대한 연구

February 2022

Graduate School of Engineering
Seoul National University
Naval Architecture & Ocean Engineering

Han-Baek Ju

Evaluation of the hydroelasticity effect for LNG CCS and prediction of sloshing pressure

LNG CCS에 대한 유탄성 효과 평가 및 슬로싱 하중 예측에 대한 연구

지도교수 장 범 선

이 논문을 공학박사 학위논문으로 제출함

2022년 1월

서울대학교 대학원

조선해양공학과

주 한 백

주한백의 공학박사 학위논문을 인준함

2022년 1월

위 원 장 남 보우 (인)

부위원장 장 범선 (인)

위 원 김 도균 (인)

위 원 김 유일 (인)

위 원 권 승민 (인)

Abstract

As environmental regulations have become more onerous, the demand for LNG and LNG carriers has increased. The LNG cargo containment system (LNG CCS) is one of the most important facilities in LNG carriers, and many membrane types of the LNG CCS have been developed so far. Traditionally, sloshing model tests are performed and a series of statistical approaches are used to obtain design sloshing pressures. Then, these design loads are utilized to analyze the strength assessment of the LNG CCS. In a sloshing model test, a flat and almost rigid plate, instead of a real model, is used to represent the LNG CCS, and thus, the hydroelasticity effect cannot be considered. In the present study, the effect of hydroelasticity on sloshing pressure was investigated by fluid–structure interaction simulation. In a series of fluid hitting simulations, it was found that the hydroelasticity effect on sloshing pressure is significant. Thus, on that basis, an LNG CCS strength assessment procedure for consideration of the hydroelasticity effect is suggested herein. In a sloshing model test, however, the number of design sloshing pressures yielded is large, which imposes a considerable time burden on LNG CCS strength assessment. In fact, the burden increases when performing a fluid–structure interaction simulation that considers the hydroelasticity effect. Therefore, a screening process by which to judge the importance of given design sloshing pressures in advance and, thereby, reduce their number as applied in LNG CCS structural design, is proposed herein. There is still insufficient information,

either on the history of sloshing pressures actually generated in LNG tanks or on the history of the stress response of insulation panels. Directly attaching sensors to the inside of a membrane or insulation panel is practically difficult. Alternatively, it is feasible to measure the response of the hull structure supporting an LNG CCS. A method of predicting the sloshing pressure and hot spot stress response of an insulation panel from the measured stress data of the supporting structure is suggested herein. The predicted sloshing pressure result is indeed helpful to understanding the actual sloshing pressure level. From this result, the reasonableness of the design sloshing pressure used in LNG CCS design also can be judged. In these ways, the predicted stress response can be used to monitor the structural integrity of an LNG CCS in real time.

Keywords: LNG CCS, sloshing pressure, hydroelasticity, fluid-structure interaction, strength assessment, structure monitoring.

Student Number: 2016-21141

LIST OF CONTENTS

Chapter 1. Introduction..... 13

1.1. Research background.....13

1.2. Research objective 17

Chapter 2. Strength assessment of LNG CCS considering the hydroelasticity effect 19

2.1. Introduction 19

2.2. Validation of LNG CCS fluid−structure interaction simulation 24

2.2.1. Description of wet drop simulation 26

2.2.2. Description of wet drop test 34

2.2.3. Comparison of wet drop simulation and wet drop test 37

2.3. Investigation of hydroelasticity effect on sloshing pressure ..42

2.3.1. Description of water hitting simulation 44

2.3.2. Selection of water column dimensions and properties 47

2.3.3. Hydroelasticity effect on sloshing pressure 54

2.3.3.1. Selection of pressure calculation regions 55

2.3.3.2. Results for flat-rigid plate model..... 56

2.3.3.3. Results for flat-flexible CCS model..... 64

2.4. Structural safety assessment procedure for LNG CCS considering hydroelasticity effect.....72

2.4.1. Suggested correction factors and empirical formulas for estimation of hyodrelasticity effect..... 73

2.4.2. Suggested LNG CCS structural safety assessment procedure considering hydroelasticity effect..... 81

2.5. Conclusions.....88

Chapter 3. Screening of design sloshing pressure using impulse superposition method 92

3.1. Introduction 92

3.2. Description of finite element model 94

3.3. Application of screening procedure 96

3.3.1. Generation of design sloshing pressure 96

3.3.2. Calculation of unit load response 97

3.3.3. Selection of critical design sloshing pressure..... 101

3.4. Conclusions.....108

Chapter 4. Prediction of sloshing pressure and LNG CCS structural response 109

4.1. Introduction 109

4.2. Prediction of sloshing pressure and LNG CCS structural response using impulse/space superposition method 114

4.2.1. Impulse/space superposition method..... 114

4.2.2. Prediction of sloshing pressure..... 118

4.2.2.1. Stress response of unit pressure..... 120

4.2.2.2. Stress response of sloshing pressure 121

4.2.2.3. Correlation between $[\boldsymbol{\delta}(\boldsymbol{t})]$ and $\{\boldsymbol{\sigma}(\boldsymbol{t})\}$..... 123

4.2.3. Prediction of hot spot stress response 135

4.3. Prediction of sloshing pressure and LNG CCS structural response using mode superposition method 141

4.3.1. Mode superposition method..... 142

4.3.2. Prediction of sloshing pressure 145
4.3.2.1. Calculation of response corresponding to applied load 145
4.3.2.2. Prediction of applied load corresponding to measured structural response 150
4.3.3. Prediction of hot spot stress response 156

4.4. Application of suggested method 158
4.4.1. Application: analysis for uniform/discrete pressure distribution 160
4.4.2. Application: analysis for continuous pressure distribution 170
4.4.3. Subdivision of pressure prediction region 189

4.5. Conclusions 199

Chapter 5. Summary of research 201

5.1. Conclusions 201

5.2. Limitations and future works 202

LIST OF FIGURES

Fig. 1. General procedure for strength assessment of LNG CCS .21
Fig. 2. KC-1 type LNG CCS FE model 26
Fig. 3. Boundary conditions of LNG CCS FE model 28
Fig. 4. Boundary conditions and dimensions of fluid domain 29
Fig. 5. Selected coupling region of LNG CCS 32
Fig. 6. Coupling between primary layer and fluid domain 33
Fig. 7. Structural response of primary layer 33
Fig. 8. Wet drop test rig 35
Fig. 9. Wet drop test specimen 35
Fig. 10. Location of pressure gauges in wet drop test 37
Fig. 11. Pressure gauge used in wet drop test 37
Fig. 12. Selected regions for pressure calculation in wet drop simulation 39
Fig. 13. Pressure profile calculated from wet drop simulation 41
Fig. 14. Pressure profile calculated from wet drop simulation(coupling direction: compressure with tension) 42
Fig. 15. Water hitting simulation model 45
Fig. 16. Motion of fluid and LNG CCS after impact 45
Fig. 17. Boundary conditions of flat-flexible CCS model 46
Fig. 18. Variables for definition of water column 48
Fig. 19. Correlation between water column height and applied pressure 50
Fig. 20. Selected water column dimensions 53
Fig. 21. Selected regions for pressure calculation 56
Fig. 22. Determination of rising time from pressure profile 57
Fig. 23. Comparison of raw data and filtered data(case1) 57
Fig. 24. Summarized peak pressure results for flat-rigid plate

cases 59
Fig. 25. Summarized rising time results for flat-rigid plate cases 61
Fig. 26. Pressure profiles according to selected region 62
Fig. 27. Pressure profiles according to deadrise angle.....63
Fig. 28. Summarized peak pressure results for flat-flexible CCS cases 66
Fig. 29. Summarized rising time results for flat-flexible CCS cases 68
Fig. 30. Pressure profiles according to selected region 70
Fig. 31. Pressure profiles according to deadrise angle.....71
Fig. 32. Calculated correction factors in 1x1 region 76
Fig. 33. Flowchart of LNG CCS strength assessment considering hydroelasticity effect 83
Fig. 34. Validation model(detached model) 85
Fig. 35. Comparison of pressure result(water hitting simulation) 86
Fig. 36. Locations for displacement calculation 87
Fig. 37. Results comparison(case1) 87
Fig. 38. Results comparison(case2) 88
Fig. 39. Results comparison(case3) 88
Fig. 40. Impulse superposition method 93
Fig. 41. LNG CCS FE model 95
Fig. 42. Boundary conditions of LNG CCS FE model 96
Fig. 43. Generated design sloshing pressures 97
Fig. 44. Selected unit load(pressure) 97
Fig. 45. Loaded area and location of hot spot 98
Fig. 46. Calculated stress response at hot spot.....99
Fig. 47. Unit load responses(vertical crushing) 100

Fig. 48. Unit load responses(shear failure) 100
Fig. 49. Calculated time history of stress response..... 102
Fig. 50. Comparison of peak stress..... 103
Fig. 51. Predicted hot spot stress responses for design sloshing pressures(vertical crushing)..... 104
Fig. 52. Predicted hot spot stress responses for design sloshing pressures(shear failure)..... 104
Fig. 53. Predicted hot spot stress responses for corrected design sloshing pressures(vertical crushing) 105
Fig. 54. Predicted hot spot stress responses for corrected design sloshing pressure(shear failure) 106
Fig. 55. Modal effective mass fraction of LNG CCS model 108
Fig. 56. Overall procedure for sloshing pressure and hot spot stress response prediction..... 113
Fig. 57. Impulse superposition method..... 115
Fig. 58. Impulse/space superposition method..... 116
Fig. 59. Impulse/space superposition method for multiple responses 117
Fig. 60. LNG CCS model..... 119
Fig. 61. Sloshing pressure prediction regions and stress measurement locations 119
Fig. 62. Stress responses of unit pressure 122
Fig. 63. Stress responses of sloshing pressure..... 122
Fig. 64. Schematic of superposition of unit pressure response. 123
Fig. 65. Application of high resolution to stress response..... 126
Fig. 66. Schematic of curvature constraint condition..... 134
Fig. 67. Selected locations for stress response comparison..... 136
Fig. 68. Comparison of vertical stress in PUF 136
Fig. 69. Selected locations for stress response prediction..... 137

Fig. 70. Loading conditions for calculation of hot spot stress response of unit pressure 138
Fig. 71. Calculated hot spot stress reponse of unit pressure 139
Fig. 72. Calculated modal effective mass fraction 143
Fig. 73. Applied pressure 146
Fig. 74. Calculated modal amplitude ($\{\boldsymbol{q}(\boldsymbol{t})\}$) 147
Fig. 75. Calculated velocity of modal amplitude ($\{\dot{\boldsymbol{q}}(\boldsymbol{t})\}$) 147
Fig. 76. Calculated acceleration of modal amplitude ($\{\ddot{\boldsymbol{q}}(\boldsymbol{t})\}$) 148
Fig. 77. Comparison of stress responses 149
Fig. 78. Calculated modal amplitude ($\{\boldsymbol{q}(\boldsymbol{t})\}$) 154
Fig. 79. Calculated velocity of modal amplitude ($\{\dot{\boldsymbol{q}}(\boldsymbol{t})\}$) 155
Fig. 80. Calculated acceleration of modal amplitude ($\{\ddot{\boldsymbol{q}}(\boldsymbol{t})\}$) 155
Fig. 81. Predicted sloshing pressure using mode superposition method 156
Fig. 82. Prediction of stress response using mode superposition method 157
Fig. 83. Selected load cases for analysis..... 161
Fig. 84. Pressure application regions and stress measurement locations..... 161
Fig. 85. Predicted sloshing pressure(Case1)..... 163
Fig. 86. Predicted sloshing pressure(Case2)..... 163
Fig. 87. Predicted sloshing pressure(Case3)..... 164
Fig. 88. Predicted sloshing pressure(Case4)..... 164
Fig. 89. Predicted sloshing pressure(Case5)..... 165
Fig. 90. Predicted sloshing pressure(Case6)..... 165
Fig. 91. Predicted hot spot stress response(Case2) 167
Fig. 92. Predicted sloshing pressure(peak) 168
Fig. 93. Predicted sloshing pressure(rising time) 169
Fig. 94. Predicted stress response(peak) 169

Fig. 95. Predicted stress response(rising time) 170
Fig. 96. FSI analysis model 171
Fig. 97. Model dimensions for FSI analysis..... 171
Fig. 98. Two deadrise angles of water block 172
Fig. 99. Boundary conditions for structure domain 173
Fig. 100. Boundary condition for fluid domain 174
Fig. 101. Fluid motion in FSI analysis(Case1) 175
Fig. 102. Calculated impact pressure(Case1) 176
Fig. 103. Predicted sloshing pressure(Case1) 178
Fig. 104. Predicted sloshing pressure(Case2) 179
Fig. 105. Predicted sloshing pressure(Case3) 179
Fig. 106. Predicted sloshing pressure(Case4) 180
Fig. 107. Predicted sloshing pressure(Case5) 180
Fig. 108. Accuracy of pressure prediction(Uniform/discrete pressure distribution, Case2)..... 181
Fig. 109. Accuracy of pressure prediction(Continuous pressure distribution(FSI), Case2) 182
Fig. 110. Predicted stress reponse(PUF σ_z) using impulse/space superposition method 184
Fig. 111. Predicted stress response(PUF σ_z) using mode superposition method 185
Fig. 112. Predicted sloshing pressure(peak) 186
Fig. 113. Predicted sloshing pressure(rising time) 186
Fig. 114. Predicted stress response(peak) using impulse/space superposition method 187
Fig. 115. Predicted stress response(rising time)using impulse/space superposition method..... 187
Fig. 116. Predicted stress response(peak) using mode superposition method 188

Fig. 117. Predicted stress response(rising time) using mode superposition method 188
Fig. 118. Subdivided pressure prediction region 189
Fig. 119. Pressure prediction results(subdivided/Case1) 192
Fig. 120. Pressure prediction results(subdivided/Case2) 193
Fig. 121. Accuracy of pressure prediction(subdivided/Case1) . 194
Fig. 122. Accuracy of pressure prediction(subdivided/Case2) . 194
Fig. 123. Stress response prediction results(subdivided/Case1) 195
Fig. 124. Stress response prediction results(subdivided/Case2) 196
Fig. 125. Stress response prediction results(original/Case1) ... 197
Fig. 126. Stress response prediction results(original/Case2) ... 198

LIST OF TABLES

Table 1. Types of material properties 28
Table 2. Comparison of pressure results 39
Table 3. Information on generated water columns 54
Table 4. Correction factors of peak pressure (C_{R-P}) for KC-1 type LNG CCS(1x1 region) 76
Table 5. Correction factors of rising time (C_{R-T}) for KC-1 type LNG CCS(1x1 region) 76
Table 6. Generated cases for verification of Level III method 85
Table 7. Design sloshing pressures 92
Table 8. Selected critical design sloshing pressures 106
Table 9. Natural frequency of LNG CCS model 107
Table 10. Comparison of two approaches(prediction of sloshing pressure) 159
Table 11. Comparison of two approaches(prediction of stress in CCS) 160
Table 12. Generated cases for FSI analysis 177

Chapter 1. Introduction

1.1. Research Background

The design sloshing pressure used for strength assessment of LNG CCS is generally obtained from sloshing model test. In the sloshing model test, the LNG tank is assumed to be a simple flat plate so that the hydroelasticity effect of LNG CCS cannot be taken into account. The design sloshing pressures are values that do not include the hydroelasticity effect.

In various ship classifications or practical design stages, the design sloshing pressures are applied to the strength assessment of LNG CCS as it is. The static analysis is adopted using only peak value of design sloshing pressure or the transient analysis is performed by additionally considering the rising time. In a simpler way, the dynamic amplification factor(DAF) value is sometimes utilized to consider the dynamic effect. This process does not take into account the hydroelasticity effect, which has a significant effect on sloshing pressure. Therefore, it can be lead to conservative design of LNG CCS.

In the present study, the hydroelasticiy effect of sloshing pressure is investigated in detail and LNG CCS strength assessment is proposed in consideration of the hydroelasticity effect using fluid-structure interaction analysis. To implement the sloshing phenomenon, water hitting model with water column as a collider is introduced. Various types of sloshing pressures are generated while changing the velocity and shape of the water column. Based on the

results of a series of water hitting simulations, it is confirmed that the hydroelasticity effect has a significant effect on the peak value and rising time of sloshing pressure.

The water hitting simulation requires a lot of computational time. As a method to replace the time-consuming fluid-structure interaction analysis, empirical formulas for the correction factor (the quantitative indicator of the hydroelasticity effect) is made. Given design sloshing pressure can be corrected using the empirical formulas. The hydroelasticity effect is considered indirectly by performing transient analysis using a corrected design sloshing pressure.

More sophisticated structural design of LNG CCS can be achieved through proposed strength assessment of LNG CCS considering the hydroelasticity effect. In the future, it can be applied not only to the structural design of LNG CCS but also to the development of new types of LNG CCS.

The design sloshing pressures determined from the sloshing model test have various rising times and peak values. The number of loaded area from which design sloshing pressures are obtained is several. In the process of deriving the design sloshing pressures, the effect of structural response of LNG CCS is not reflected. It is difficult to determine which pressures are critical from a structural point of view only with the design sloshing pressure data. Performing finite element(FE) analysis for all given design sloshing pressures take a lot of time and, in particular, when fluid-structure interaction analysis is introduced in order to consider the hydroelasticity effect,

the burden increases.

In the present study, the process for judging the importance of given sloshing pressures is suggested using the impulse superposition method. A triangular impulse is applied to the loaded area where the design sloshing pressures are obtained to calculate stress at the hot spot in insulation panel. Using this unit load response, the hot spot stress from the design sloshing pressures can be simply inferred without finite element analysis. Finally, for each failure mode, the most critical design sloshing pressure is selected. Design efficiency is improved by performing detailed finite element analysis only on the design sloshing pressures selected by screening process.

So far, information on sloshing pressure time history and stress response time history of insulation panel generated in actual LNG tanks have not been clearly identified. There is a limit in the judgement of whether the design sloshing pressures obtained from the sloshing model test is appropriate and the level of fatigue damage in the insulation panel. Due to the structural characteristics of LNG CCS, it is not realistic to measure the pressure and stress by placing sensors on the membrane or inside the insulation panel. Alternatively, the stress of the hull structure supporting LNG CCS can be measured.

Thus, in this study, the procedure for predicting sloshing pressure and stress response of insulation panel using the measured stress data on supporting structure is proposed. Since the sloshing pressure is applied by the specific area, the impulse superposition method is adopted to predict the sloshing pressure. In order to consider the effect of the sloshing pressures on several regions, the concept of

space superposition is additionally introduced. The relationship between the measured stress, the stress generated by the unit pressure, and the sloshing pressure acting on membrane is derived through the mathematical formulation of the impulse/space superposition method. The least square method is adopted to calculate the sloshing pressure.

A method of calculating the actual hot spot stress of insulation panel using the predicted sloshing pressure and the hot spot stress of insulation system caused by the unit pressure is proposed. In addition, a method of estimating hot spot stress of insulation panel by applying the mode superposition method is suggested.

From the predicted sloshing pressure time history, it is possible to identify the peak level and the range of rising time of actually occurring sloshing pressure. The validity of the design sloshing pressure currently used can be verified.

From the predicted stress time history, vertical crushing, shear failure and fatigue damage calculations of LNG CCS can be carried out in real time. It means that the monitoring of structure integrity of LNG CCS is possible in real time.

1.2. Research objective

This study consists of three chapters. The research objective for each chapter is organized as follows.

Chapter 2. Strength assessment of LNG CCS considering the hydroelastictiy effect

- Determine design sloshing pressures generally from sloshing model test
- Use the design sloshing pressures directly to static or transient analysis.
- Not include the hydroelasticity effect in the conventional approach.
- May lead to the conservative structure design of LNG CCS

➢ Suggest the method to consider the hydroelasticity effect in LNG CCS strength assessment

➢ Investigate the hydroelasticity effect on design sloshing pressures in detail

Chapter 3. Screening of design sloshing pressure using impulse superposition method

- Perform strength assessment of LNG CCS for all given design sloshing pressures
- Require a significant amount of computation time

➢ Suggest the screening process to reduce the number of design sloshing pressure to consider

Chapter 4. Prediction of sloshing pressure and LNG CCS structural response

- Lack of information on sloshing pressure history and hot spot stress response history occurring in actual LNG tank
- Difficult to attach the sensors directly to membrane and insulation panel

➢ Suggest the method to predict sloshing pressure from stress response on supporting structure

➢ Propose the method to estimate hot spot stress response of LNG CCS

Chapter 2. Strength assessment of LNG CCS considering the hydroelasticity effect

2.1. Introduction

With the rapid growth of LNG demand in the global market, orders for LNG carriers have steadily increased. When constructing LNG carriers, one of the most important issues is the design of the LNG cargo containment system (LNG CCS). Among the several types of LNG CCS, the membrane type is the most widely used in LNG carriers. Several kinds of membrane-type LNG CCS, e.g. Mark III, NO96, KC-1, and SOLIDUS, have been developed so far in consideration of insulation performance, manufacturing efficiency and structural integrity (Jeong and Shim [1], Jeong et al. [2], Jin et al. [3], Kim et al. [4]).

Generally, the design sloshing loads are obtained from the sloshing model test. The sloshing model test contains many uncertainties, e.g. scale law and the effect of gas compressibility and surface tension; thus, a number of researchers have tried to design more reliable sloshing model tests (Kimmoun et al. [5], Kuo et al. [6], Brar and Singh [7]). Even though the sloshing model test is carried out with high precision, the LNG CCS model used in it is only a single, almost-rigid plate, which means that the effect of LNG CCS flexibility is ignored when selecting design sloshing pressure. In fact, an actual membrane-type LNG CCS is composed of thin layers and insulation panels, which are relatively flexible compared with a ship's hull. This feature makes the hydroelasticity effect on the design sloshing

pressure more significant. Many researchers studying the effect of hydroelasticity (e.g. Bereznitski [8], Stenius [9]) have verified that the role of hydroelasticity is significant in cases where the structure is a flexible body.

Classification bodies (ABS [10], Bureau veritas [11], DNVGL [12], Lloyd's [13]) have proposed the LNG CCS structural safety assessment procedure shown in Fig. 1. In the Level I method, a static analysis is conducted using the peak value of design sloshing pressure obtained from the sloshing model test, and then the dynamic amplification factor (DAF) corresponding to the rising time is applied to estimate the structural response of the LNG CCS. In the Level II method, the dynamic effect is directly considered by performing a transient analysis wherein the design sloshing load is idealized as a triangular pulse. These two methods have limitations in terms of consideration of the hydroelasticity effect of the LNG CCS. In fact, there is a category in the guidance that implements LNG CCS structural safety assessment using fluid-structure interaction analysis named the Level III method; however, no exact procedure has yet been established. Looking at the fluid-structure interaction analysis model suggested by ABS, by additionally modeling the LNG domain, the interaction between LNG and the LNG CCS is realized (ABS [10]). The applied load in this fluid-structure interaction analysis model is the design sloshing pressure obtained from the sloshing model test; thus, the hydroelasticity effect on sloshing load is not reflected in the Level III method.

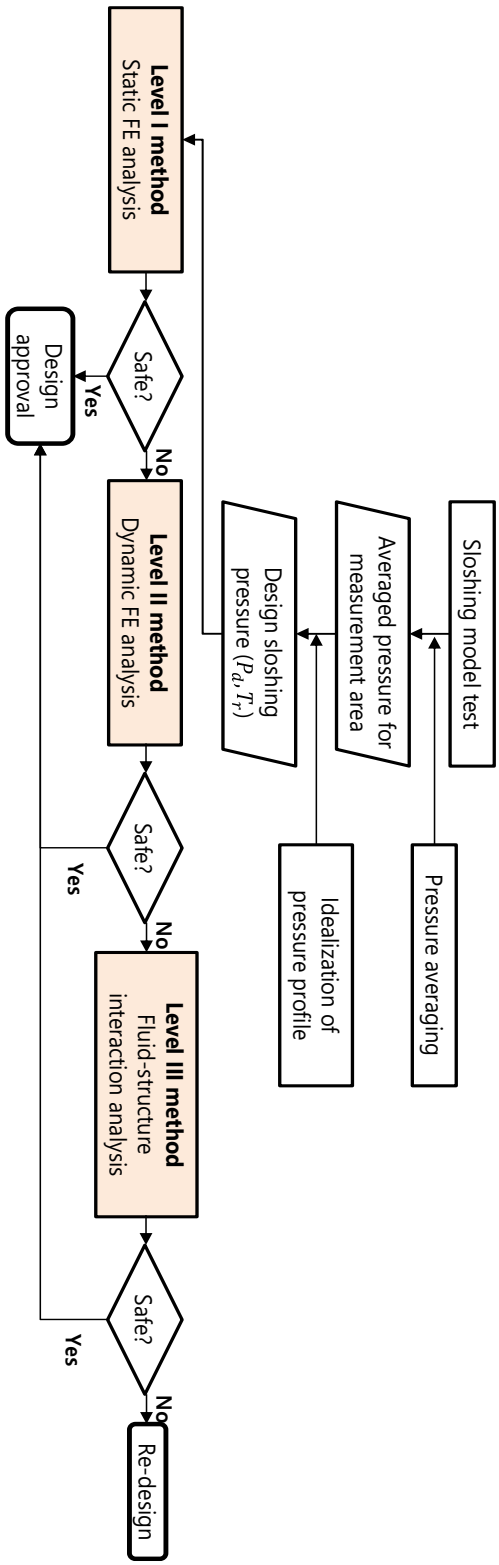

Fig. 1. General procedure for strength assessment of LNG CCS

There are some approaches to consideration of the hydroelasticity effect of LNG CCS that do not entail fluid-structure interaction analysis (Jin et al. [14], Wang and Kim [15], Lee et al. [16]). Jin et al. [14] indirectly considered the fluid-structure interaction effect by introducing a dashpot system; this, however, is a rough method compared with the fully coupled fluid-structure interaction analysis. Wang and Kim [15] performed a fluid-structure interaction analysis using a 2D model, but by this methodology, it is difficult to realize the sloshing phenomenon induced by the impact between the primary layer of the LNG CCS and the fluid. Lee et al.[16] took the fluid-structure interaction effect into account by calculating sloshing pressure through a global analysis and applying it to their structural model as an applied load. This is called one-way fluid-structure interaction analysis' and it should be noted that it does not consider the effect of structural behavior on the hydrodynamic force for each time step.

Therefore, investigation of the hydroelasticity effect on sloshing pressure by means of a fully coupled fluid-structure interaction analysis is necessary. As several fluid-structure interaction analysis methods have been developed and computing power increases, attempts have been made to realize fully coupled fluid-structure interaction analysis of LNG CCS (Kim et al. [17], Lee et al. [18]). Kim et al. [17] and Lee et al. [18] performed fluid-structure interaction analyses of the LNG CCS; then, they verified the validity of the analysis by comparing it with wet drop test results. However, they did not discuss how this analysis could be applied to structural

safety assessment of the LNG CCS.

If the hydroelasticity effect is large, the design sloshing pressure may be different from the pressure causing the maximum response of the actual structure (Faltinsen [19]). In order to evaluate the hydroelasticity effect on physically meaningful sloshing pressures, the interaction between the fluid motion in the LNG CCS and the structural response should be considered in real time such as 3D fully coupled sloshing simulation. However, this has technical limitations, and design sloshing pressure determination and structural safety assessment of LNG CCS are individually performed in the actual design of LNG CCS as shown in Fig. 1. In the present step, it was thought to be realistic to focus on the investigation of the hydroelasticity effect for the given design sloshing pressure obtained from sloshing model test.

In the present study, a three-dimensional (3D) KC-1-type LNG CCS was modeled, and a fully coupled fluid-structure interaction numerical simulation was performed using the commercial software LS-dyna. The applied sloshing load and the structural response of the LNG CCS were calculated simultaneously by using arbitrary Lagrange-Eulerian coupling and multi-material methods with the penalty coupling algorithm (Zeng [20], Aquelet et al. [21]). The numerical simulation was validated by comparison with a wet drop test carried out at Pusan National University in terms of the pressure on the primary layer of the LNG CCS. After validating the numerical simulation, a fluid-hitting model of the sloshing phenomenon was run. A total of two simulation models, namely the flat-rigid plate model

and the flat-flexible CCS model, were generated to investigate the hydroelasticity effect. The pressures calculated from each model were compared, based on which, correction factors representing the effect of hydroelasticity were derived (and are proposed herein). Ultimately, a membrane-type LNG CCS structural safety assessment procedure for consideration of the hydroelasticity effect was formulated (and is presented herein).

In the proposed procedure, there are two ways to consider the hydroelasticity effect of the LNG CCS. In one method, the hitting condition generating the design sloshing load is found from the flat-rigid plate model. By applying this hitting condition to the flat-flexible CCS model, structural safety assessment of the LNG CCS can be implemented. This method has the highest accuracy; however, it requires a repetitive, time-consuming fluid-structure interaction analysis. In order to reduce the burden of analysis, a method of LNG CCS structural safety assessment considering the hydroelasticity effect through transient analysis was additionally devised based on correction factors in the form of quantitative values of the hydroelasticity effect of the LNG CCS).

2.2. Validation of LNG CCS fluid-structure interaction simulation

There are a number of methods by which fully coupled fluid-structure interaction analysis can be performed. Among them, LS-dyna can calculate the behavior of fluids and the response of

structures simultaneously by means of the penalty coupling algorithm. This feature reduces calculation time and enhances analysis efficiency, since there is no need to consider the compatibility between the fluid solver and the structure solver. However, in LS-dyna, the fluid is assumed to be incompressible, and moreover, the penalty factor must be properly selected by users. If a too-small or too-large penalty factor is adopted in the simulation, numerical error might be generated. Due to those limitations, it is necessary to establish a more sophisticated numerical simulation technique from experiment results.

The LS-dyna fluid-structure interaction solver has been verified for various simple cases so far. Comparative validation was conducted for the pressure generated during rigid wedge drop (Cheon et al. [22]), and validation was also completed for the flat-stiffened plate (Truong et al. [23], Truong et al. [24]). When performing fluid-structure interaction analysis for LNG CCS, the effect of flexible insulation system composed of plywood and polyurethane foam should be additionally considered. Since the fluid-structure interaction analysis using full LNG CCS model as a structure domain has not been dealt with yet, comparison with actual experimental result is required. To that end, a wet drop test for the KC-1-type LNG CCS was carried out at Pusan National University, and the pressure profiles thus measured were compared with the numerical simulation results.

2.2.1. Description of wet drop simulation

For direct comparison between the wet drop test and the wet drop simulation, the KC-1-type LNG CCS specimen utilized in the wet drop test was selected as the structure model in the wet drop simulation. The KC-1-type LNG CCS consists of two membrane layers, insulation panels and mastic, as shown in Fig. 2. The membrane layer that is in contact with the LNG is called the primary layer, and the other is called the secondary layer. A single plywood layer exists between the two membrane layers. Several layers of plywood and polyurethane foam compose the insulation panels.

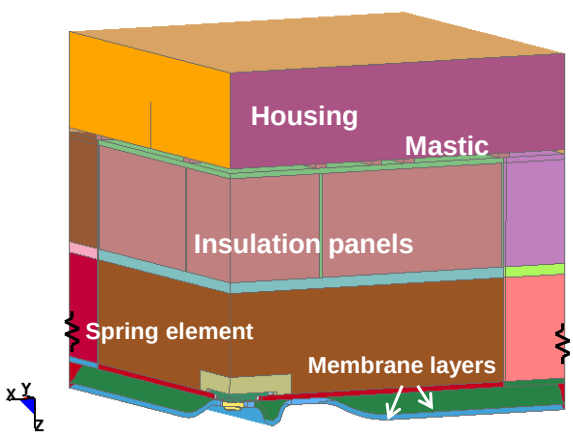

Fig. 2. KC-1 type LNG CCS FE model

The Belytscho-Tsay 2D shell element and a constant-stress 3D solid element are utilized to model the two membrane layers and insulation panels, respectively. According to the guidance for structural response analysis of the LNG CCS suggested by DNVGL [12], not only should multiple meshes be used in the thickness

direction of the plywood, but also, the shape function of each element should be larger than linear (e.g. a 4-node shell element and an 8-node solid element). These requirements can be met in the quasi-static analysis or transient analysis; however, it is demanding in the fully coupled fluid-structure interaction analysis. This research focused on the change of sloshing pressure according to the flexibility of the LNG CCS rather than the structural behavior of the LNG CCS. Therefore, it was sufficient to use a relatively simple finite element (FE) structural model.

The size of the shell element applied to the membrane layers is selected as 15mm by 15mm. This mesh size can represent the shape of corrugation geometry smoothly. The identical mesh size is applied to insulation panels and mastic for equivalencing of all parts. The friction effect induced by the in-plane load and the occurrence of a gap generated by vertical tension between the adjacent layers are disregarded. To reduce the computation time, symmetric boundary conditions are applied to each direction, and only a quarter model of the LNG CCS is used in the numerical simulation, as shown in Fig.3. An elastic spring element is added to the housing to reflect the same stiffness as the wet drop test specimen. Information on the material properties of each part of the LNG CCS is summarized in Table 1. Since it is difficult to accurately determine the plastic behavior of plywood and polyurethane foam, the occurrence of insulation panel failure was ignored in the simulation. The utilization of orthotropic elastic material properties for plywood and polyurethane foam is recommended in practice (DNVGL [12]).

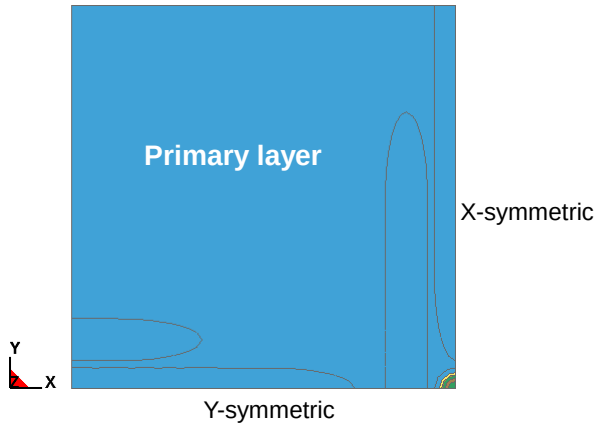

Fig. 3. Boundary conditions of LNG CCS FE model

Table 1. Types of material properties

	Membrane layers	Plywood	Polyurethane foam	Housing	Mastic
Types of material properties	Piecewise linear plastic	Orthotropic elastic	Isotropic elastic	Piecewise linear plastic	Perfectly plastic
Density (kg/m3)	7930	680	118	10410	1200
Elastic modulus (MPa)	190000	8900, 7500, 4100 (E11, E22, E33)	35	206000	2900
Yield stress (MPa)	205	-	-	355	15
Poisson's ratio	0.29	0.17	0.3	0.3	0.3

For fully coupled fluid-structure interaction analysis, the fluid domain containing the LNG CCS structure model should be generated. The breadth and width of the fluid domain are equal to the size of the water basin used in the wet drop test. The exact values for the dimensions of fluid domain are illustrated in Fig. 4. The all-fixed boundary condition is applied to the bottom and outer regions of the water domain, and a non-reflecting boundary condition is applied to the outer region of the air domain, as depicted in Fig. 4. The quarter model of the fluid domain is used with the symmetric boundary

condition, as is also the case with the LNG CCS model. Eulerian mesh is adopted to generate the fluid domain for prevention of mesh distortion. The spreading motion of water after an impact is realized by utilizing a multi-material method.

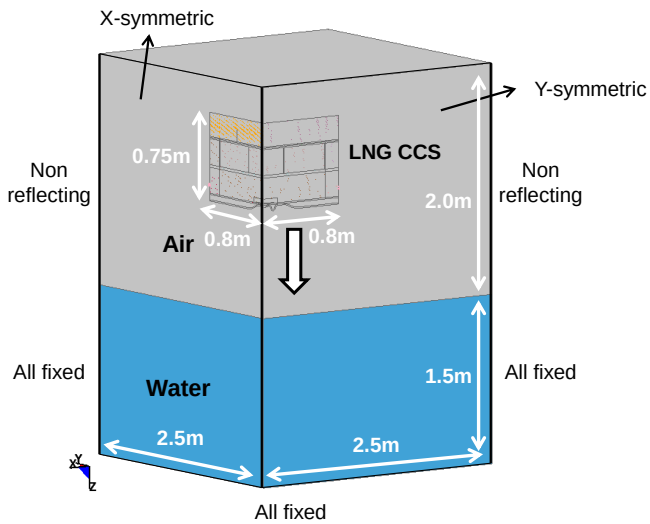

Fig. 4. Boundary conditions and dimensions of fluid domain

In the wet drop test, the LNG CCS model was dropped freely from 3m with zero incident angle. Since a large air domain is required to realize free fall of the LNG CCS in numerical simulations, the initial velocity of 7.65m/s was applied to the LNG CCS and the gravity effect was ignored. The pressure generated during impact is dominantly determined by the impact velocity, and the inertia effect by gravity is not significant. It was considered reasonable that the gravity effect is neglected in terms of analysis efficiency (Greenhow [25], Khabakhpasheva and Korobkin [26], Luo et al. [27]). The zero incident angle was adopted also for the wet drop simulation. Fine

mesh was used in the vicinity of the free surface, and a one-way bias meshing technique was adopted to reduce the total number of fluid elements. In order to ensure proper coupling of the LNG CCS with the fluid domain, the mesh size of the fluid domain should be small enough (Toshikawa and Yoshida [28]) and similar to that of LNG CCS (Cheon et al. [22]). When the mesh size of structure domain is considerably larger than that of fluid domain, leakage phenomenon may occur at impact. In the wet drop simulation, to satisfy these requirements, the fluid volume that the LNG CCS passes through had the same mesh size as the LNG CCS structure model. To calculate the pressure and motion of fluid, a linear polynomial model and the Gruneisen model of equation of state were applied to air and water, respectively (LSTC, [29]). The Gruneisen model is suitable for implementing phenomena, such as water impacts, that accompany large nonlinearity. The explicit formulas for the two equation of state models are expressed in Eq. (1) and Eq. (2). The coefficients of each equation of state were selected on the basis of previous researches (Truong et al. [23], Truong et al. [24]).

$$\mathrm{P} = C_0 + C_1\mu + C_2\mu^2 + C_3\mu^3 + (C_4 + C_5\mu + C_6\mu^2)E \cdots (1)$$

where,

P: pressure of fluid (Pa)

E: internal energy per unit volume (Pa)

$\mathrm{C_1}$~$\mathrm{C_6}$: coefficients ($C_4 = C_5 = 0.4$ and $C_0 = C_1 = C_2 = C_3 = C_6 = 0$)

μ: volumatic parameter $\left(= \frac{\rho}{\rho_0} - 1\right)$

$$\mathrm{P} = \frac{\rho_0 C^2 \mu \left(1 + \left(1 - \frac{\gamma_0}{2}\right)\mu - \frac{a}{2}\mu^2\right)}{\left(1 - (S_1 - 1)\mu - S_2 \frac{\mu^2}{\mu + 1} - S_3 \frac{\mu^3}{(\mu + 1)^2}\right)^2} + (\gamma_0 + a\mu)E \cdots (2)$$

where,

γ_0: Gruneisen gamma ($\gamma_0 = 0.35$)

$\mathrm{C}, S_1, S_2, S_3, \mathrm{a}$: coefficients ($\mathrm{C} = 1647, S_1 = 1.921, S_2 = -0.096, S_3 = 0$ and $\mathrm{a} = 0$)

$\mathrm{E}|_{t=0}$: initial internal energy per unit volume ($\mathrm{E}|_{t=0} = 2.895 \cdot 10^5 \mathrm{Pa}$)

In Eq. (2), the volumetric parameter μ is zero in the initial state. Thus, the initial pressure is calculated by multiplying γ_0 by the internal energy E0. It was confirmed that the calculated initial pressure was identical to atmospheric pressure. The effect of hydrostatic pressure was ignored, because the impact between the LNG CCS and water occurs on the free surface. The density of water and air were selected as $1000\mathrm{kg}/m^3$ and $1.025\mathrm{kg}/m^3$, respectively.

The insulation panel of the LNG CCS modeled by 3D solid mesh overlapped with the air domain in the initial state, as shown in Fig. 4. When applying coupling between the entire LNG CCS structural model and the fluid domain, a numerical error occurs. To avoid this problem, the housing and the primary layer surrounding the LNG CCS were set as one segment and then coupled to the fluid domain, as illustrated in Fig. 5. It can be seen that until the impact between the LNG CCS and the water occurred, only a small pressure acted on the LNG CCS by the effect of air. The default penalty coupling factor 0.1 recommended by LS-dyna was selected in the simulation, and it was

observed that there was no water leakage at the primary layer, as shown in Fig. 6. The impact between the LNG CCS and water was well represented, and the post-impact stress distribution on the LNG CCS also was acceptable. Fig. 7 shows the structural response of the primary layer after the impact. The stress is concentrated in the corrugated area; however, it is considerably smaller than the tensile strength. The maximum plastic strain occurs locally at the junction of the corrugation and the cap structure located in the center of the primary layer. The global plastic strain on the corrugation area is less than 2%, and thus, the membrane layer was considered to be structurally safe. Small stresses also were calculated in the plywood and polyurethane foam that make up the insulation panels. However, since the allowable stress of plywood or polyurethane foam is somewhat lower than that on general steel materials, quasi-static analysis or transient analysis with a precise structure model would be required for accurate structural safety assessment of insulation panels.

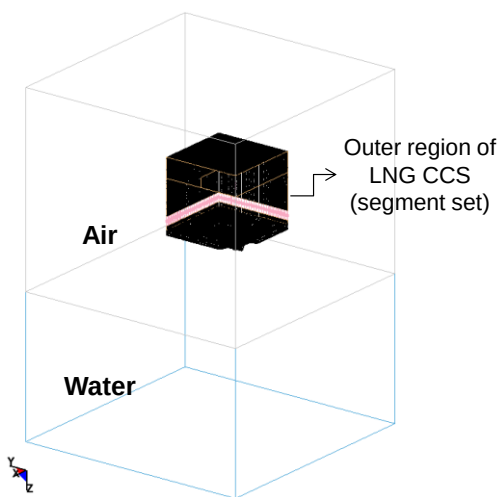

Fig. 5. Selected coupling region of LNG CCS

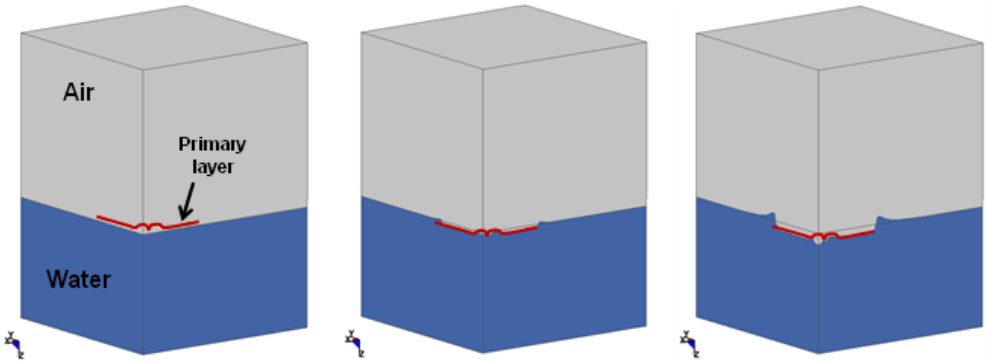

Fig. 6. Coupling between primary layer and fluid domain

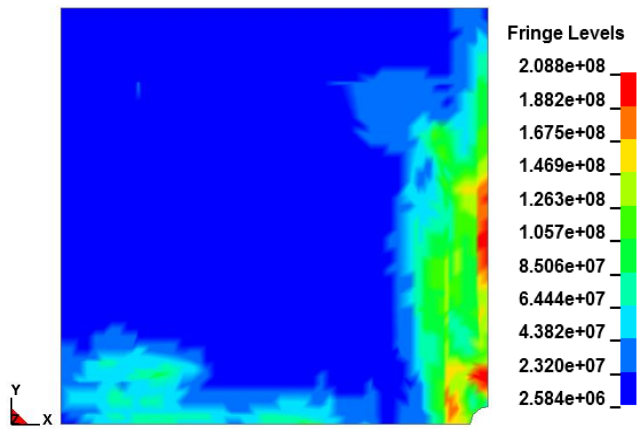

(a) V-M stress distribution (at instant of water entry)

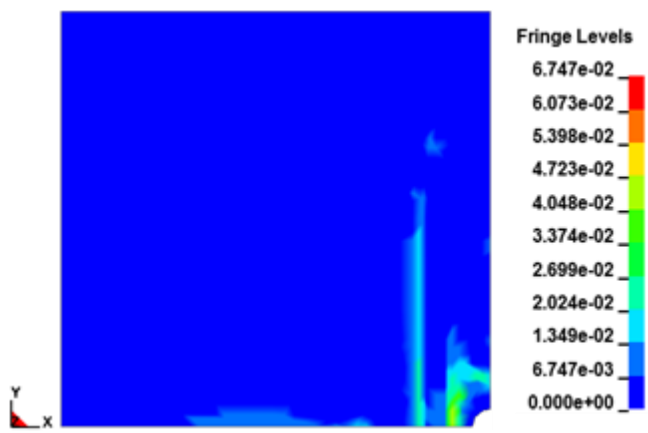

(b) Plastic strain distribution (at final simulation time)

Fig. 7. Structural response of primary layer

2.2.2. Description of wet drop test

The traditional sloshing model test for the LNG CCS is generally performed at a scale of 1/70 to 1/50. However, due to the scale effect, it is difficult to capture the high movement of fluid particles in this test. A wet drop test with a full-scale LNG CCS panel can be an alternative means of investigating the structural response of the LNG CCS to the sloshing phenomenon. Several researchers have studied the wet drop test with different specimen types and various drop conditions (Chung et al. [30], Chuang [31], Ahn and Kwon [32]). They concluded that the existence of corrugation, the flexibility of the LNG CCS, and an air cushion have a significant effect on the sloshing pressure or the structural response of the LNG CCS.

In this study, the wet drop test was carried out at the wet drop test research center of Pusan National University to understand the structural response of the KC-1-type LNG CCS. Fig. 8 depicts the wet drop test facility. There is a magnetic system for release of LNG CCS specimens and a linear motion (LM) guide system to reduce the friction effect during specimen drops. The maximum drop height of this facility is 4m. The total weight of the specimen was 1400kg, and it was dropped at a 3m height. The incident angle was set to 0 degrees. The specimen was exquisitely crafted to prevent any gap between the layers caused by its own weight under the hanging condition. The shape and properties of the specimen utilized in the wet drop test, shown in Fig. 9, were identical to those of the LNG CCS model in the wet drop simulation.

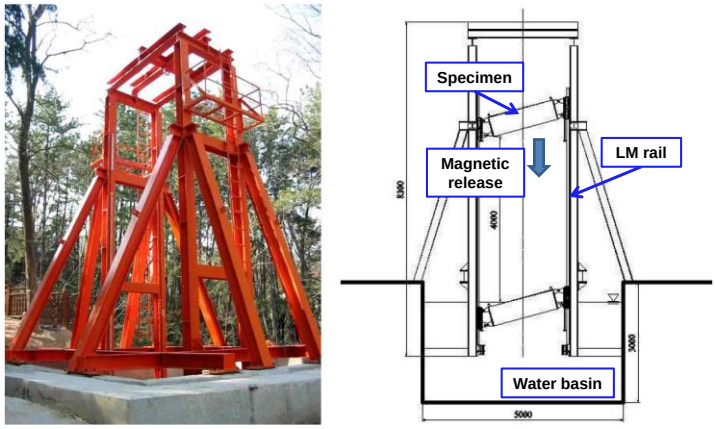

Fig. 8. Wet drop test rig

Fig. 9. Wet drop test specimen

In wet drop test, the impact pressure was measured on the two regions as illustrated in Fig. 10. The first region, P1, and the second region, P2, were located in the center and outer regions of the LNG CCS specimen, respectively. There were corrugation areas around P1, while the vicinity of P2 was neatly flat. A glued joint-type pressure gauge was attached to the rear side of the primary layer to prevent its damage. The pressure gauge is PS-50KAM536 model made by KYOWA's, and the maximum allowable measurement pressure is 50bar. Detailed photo of pressure gauge is illustrated in

Fig. 11. The pressure data was obtained at a sampling rate of 20kHz. Repetitive dropping of the LNG CCS specimen was performed to examine the cumulative damage to the LNG CCS. During the wet drop test, in the process of hanging the specimen, the gap between the layers constituting the specimen can occur. In order to prevent this phenomenon, several times of pre-drop at a low height were performed in advance.

The KC-1-type LNG CCS has large height of corrugation, and so the air cushion effect was observed at the region between the corrugation and the flat plate. After the 5th drop, consistent peak pressure was measured, and after the 10th drop, the corrugation buckling occurred. After the 30th drop, quite large permanent deformation of the insulation panel was visually observed. However, repetitive dropping is difficult to implement through numerical simulation. Thus the converged wet drop test pressure which is the value measured at the actual drop height case after several pre-drops and the pressure calculated from the single drop in the numerical simulation were compared. The time step for plotting of the pressure profile was 0.05ms, as correspondent to a sampling rate of 20kHz.

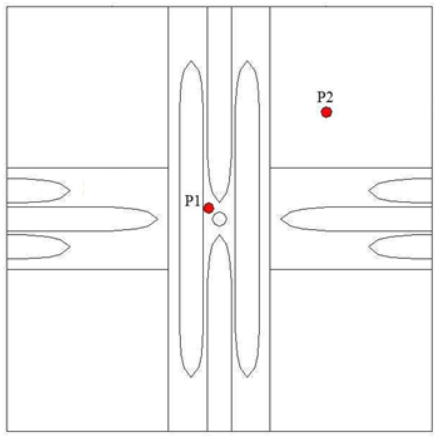

Fig. 10. Location of pressure gauges in wet drop test

Fig. 11. Pressure gauge used in wet drop test

2.2.3. Comparison of wet drop simulation and wet drop test

Verification of the LNG CCS fluid-structure interaction analysis was conducted by comparing its results with those of the wet drop test. This has limitations in terms of cost and time to perform experimental tests for various impact conditions. If the fluid-structure analysis of the LNG CCS is justified, LNG CCS design efficiency can be greatly improved. In addition to that, investigation of the hydroelasticity effect, which cannot be considered in the sloshing model test, becomes possible.

In the wet drop simulation, the selected region for pressure

calculation was the same as the location of the pressure gauge in the wet drop test, as shown in Fig. 12. The outer region corresponds to P2 in Fig. 10, since symmetric boundary conditions were applied to LNG CCS model. The two variables that most influenced the dynamic response of the LNG CCS were peak pressure (P_{max}) and rising time (t_r).

For direct comparison with the wet drop test, the shape of the actual LNG CCS was precisely modeled in the wet drop simulation. Corrugation of the primary layer was also reflected in the structure model. The existence of corrugation on the primary layer generated complex fluid motion, which is a controversial issue with regard to the sloshing phenomenon. It increased the noise and the uncertainty of the pressure result calculated from the LNG CCS fluid-structure interaction analysis. Trapped air between the LNG CCS and water, which induced an air cushion effect, was observed in the wet drop simulation. The thickness of the trapped air in the primary layer was uneven due to the existence of corrugation. Therefore, relatively more noise appeared in the pressure profile compared to the flat-stiffened plate results (Truong et al. [24]). In order to prevent numerical uncertainty induced by corrugation, only the coupling direction of compression is considered in wet drop simulation and 10-point average filter is applied to calculated results.

The rising time determined from the maximum and half maximum value of pressure profile changes sensitively to small noise as well as the overall shape of pressure profile. This leads to difficulty in selecting a proper rising time in the wet drop simulation. As an

alternative, comparison of duration time (t_d) instead of rising time was performed.

The wet drop test results and wet drop simulation results are summarized in Table 2. In both regions, the peak pressure and duration time were well matched.

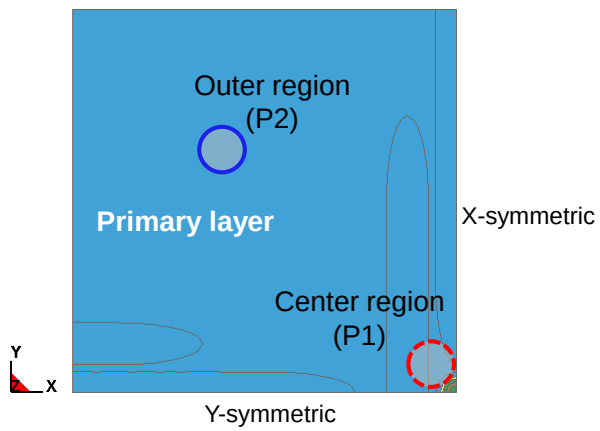

Fig. 12. Selected regions for pressure calculation in wet drop simulation

Table 2. Comparison of pressure results

		Wet drop test	Wet drop simulation
Center region (P1)	Peak pressure (bar)	**6.8**	**5.6**
	Duration time (ms)	**13.2**	**11.1**
Outer region (P2)	Peak pressure (bar)	**7.8**	**8.8**
	Duration time (ms)	**9.6**	**7.0**

The pressure profiles calculated from the wet drop simulation is shown in Fig. 13. For comparison of the pressure profiles, the results

obtained from the wet drop test are also illustrated. The time axis of the wet drop test pressure profile was corrected to show the two results in one figure. LNG CCS model is always coupled to the fluid domain composed of air and water, and coupling is performed in the normal direction of the outer region of LNG CCS (see Fig. 5). Since only coupling by compression is considered, negative pressure due to the suction effect does not appear in wet drop simulation.

The penalty coupling algorithm that assumes the contact phenomenon as a spring system and volume of fraction(VOF) method for dealing with multi-material problem was applied to the wet drop simulation. The contact force is determined by the penetration depth between the two objects in contact and penalty factor representing stiffness of spring system (Aquelet et al. [21], Aquelet and Souli [33]). There is a limit to accurately considering the characteristics of fluids using these methods. The occurrence of 2 peaks in the center region and sharp peak in the outer region are caused by numerical uncertainty. These numerical limitations notwithstanding, since the magnitude of pressure and the duration time of the pressure profile calculated from the wet drop simulation were acceptable, the numerical simulation could be used to investigate the hydroelasticity effect of the LNG CCS.

Both the effect of compression and tension are considered in the default setting provided by LS-dyna (Olovsson et al. [34]). The calculated results using default setting are illustrated in Fig. 14.

As soon as the water hits the structure, the flexible structure begins to vibrate and the gap between the primary layer and water

increases in a moment. Then the spring to model the coupling gives tensile force to represent the suction pressure. The suction effect is large at outer region(P2) where flexural rigidity is relatively small and it leads to the peak pressure underestimation and rapid pressure drop. In reality, the suction pressure is hard to happen due to the air-flow into the gap and high compressibility of the air. For the FSI simulation model including corrugation on primary membrane, it is appropriate to set the penalty coupling direction to only compression.

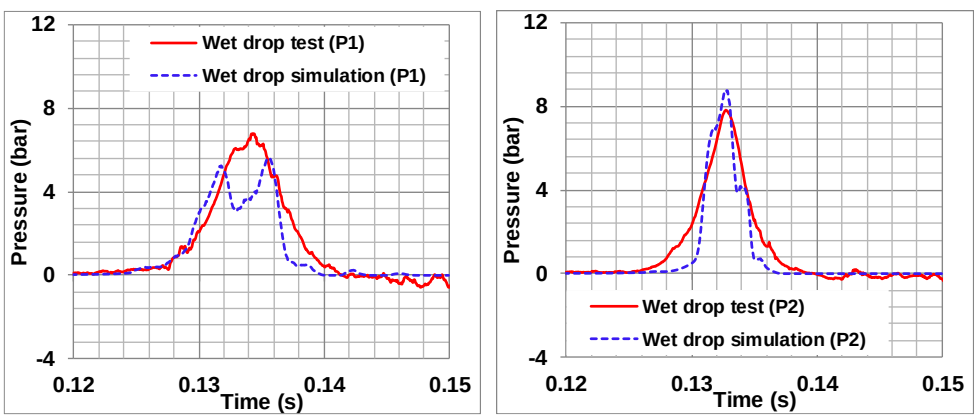

(a) center region (b) outer region

Fig. 13. Pressure profile calculated from wet drop simulation (penalty coupling direction: only compression)

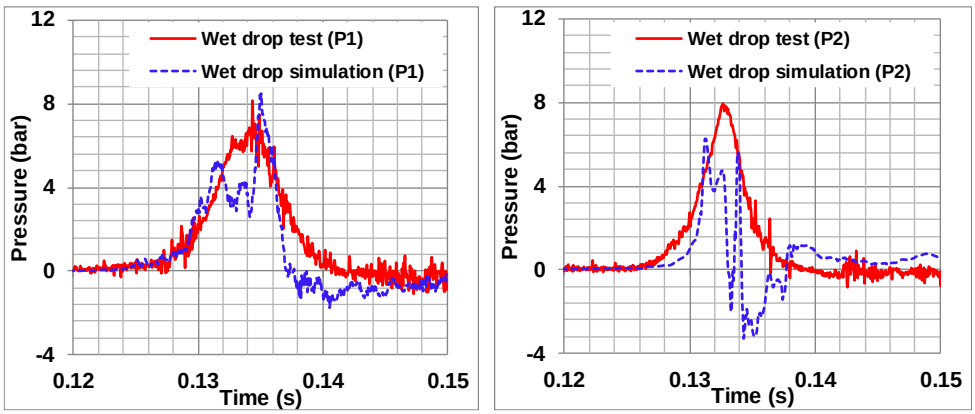

(a) center region (b) outer region

Fig. 14. Pressure profile calculated from wet drop simulation (coupling direction: compression with tension(default))

2.3. Investigation of hydroelasticity effect on sloshing pressure

The design sloshing pressure was obtained from a sloshing model test in which a scale model of the LNG tank was utilized. The LNG CCS structure was idealized to a single, flat and almost rigid plate in the sloshing model test. This means that the effect of hydroelasticity and corrugation cannot be considered in calculation of design sloshing pressures used to assess the structural safety of the LNG CCS.

A membrane-type LNG CCS composed of thin stainless membrane layers and insulation panels is much more flexible than a ship's hull; thus, the hydroelasticity effect was evident. Chung et al. [30] conducted a wet drop test with three different specimens, i.e., a rigid model, the MARK III model with a flat membrane, and the MARK III model with a corrugated membrane. They showed that the consideration of hydroelasticity and the existence of corrugation

reduce the peak pressure.

Complex fluid motion is generated when impact occurs on the primary layer due to the existence of corrugation. This affects sloshing pressure characteristics and structural response of insulation system. However, in the KC-1 LNG CCS, the corrugation distribution on primary layer is less dense than Mark III type and there is no closed area surrounded by corrugation. These features reduce the air pocket effect. In addition, since the large peak pressure would happen at low deadrise angle, its interruption effect of the corrugation on the fluid is also not significant. The effect caused by the fluid moving parallel to primary layer (Bogaert et al. [35], Malencia et al. [36]) is small in the impact condition where the deadrise angle is close to 0 degree. Thus, it could be judged that the corrugation effect is not highly critical in terms of structural safety assessment of KC-1 type LNG CCS.

In the present research, the corrugation effect was disregarded and the sheer effect of hydroelasticity was investigated using two different models: a flat-rigid plate model and a flat-flexible CCS model. In the flat model, since the section modulus is the same throughout the primary layer, high frequency oscillation of the primary layer does not occur and the rapid change of pressure profile during the impact hardly appeared. There is no uneven air cushion effect between the primary layer and water caused by the presence of corrugation. The hydroelasticity effect could be quantitatively defined by comparing the results of the two models.

2.3.1. Description of water hitting simulation

In the real sloshing phenomenon, fluid collides with the primary membrane layer of the LNG CCS with a specific shape and velocity. Many numerical approaches have been attempted to reproduce the sloshing model test (Chen [37], Loots et al. [38]). Most of them focused on fluid motion in the sloshing phenomenon, and have a limitation in their consideration of the flexibility of the LNG CCS. Therefore, a water hitting simulation was devised to realize the sloshing phenomenon considering the hydroelasticity effect, as shown in Fig. 15. In the water hitting simulation, unlike the wet drop simulation, the clamped boundary condition was applied to the top of the structure model, and the initial velocity was given to the water column. Also, the housing was removed from the KC-1-type LNG CCS structure model. In the wet drop simulation, after the impact between the LNG CCS and water occurred, the velocity of the LNG CCS decreased and the water accumulated, whereas in the water hitting simulation, the water column spread from the center to the outer region, and the LNG CCS was compressed like a spring with one end fixed. Fig. 16 depicts the fluid motion after the impact was generated. In a real ship structure, the top of the LNG CCS is connected to the inner hull. Since side stringers and web frames are attached to the inner hull, it is sufficiently stiffer than the insulation panels. Therefore, the structural behavior of the LNG CCS in water hitting simulation can reflect the actual phenomenon.

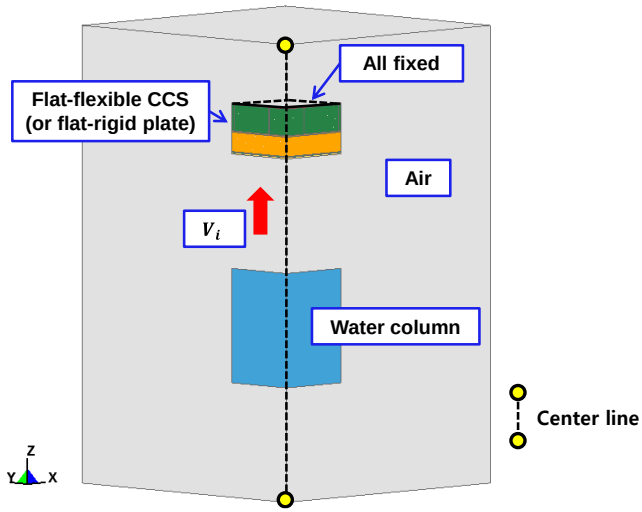

Fig. 15. Water hitting simulation model

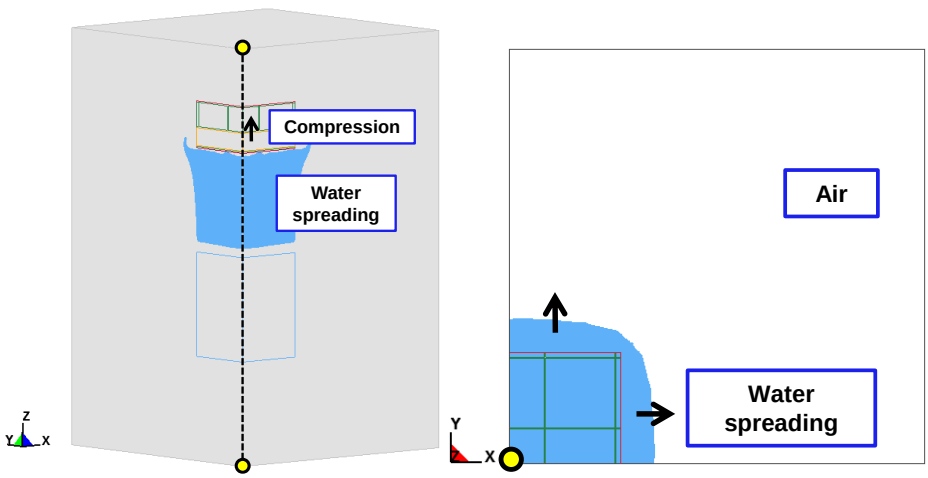

(a) Iso view (b) Top view

Fig. 16. Motion of fluid and LNG CCS after impact

The settings for the coupling between the fluid and the structure and material properties were equal to the wet drop simulation, as verified by the experimental test. A mesh size of 15mm by 15mm was applied to the entire KC-1-type LNG CCS model as well as to the water column and fluid domain that the water column passes

through. Since the primary layer of the LNG CCS was simplified as a flat-plate, the mesh was evenly generated, and the coupling between the LNG CCS model and the water column occurred smoothly. To reduce the calculation time, a quarter model of the LNG CCS and water column was used with the symmetric boundary condition in the same manner as in the wet drop simulation. The membrane-type LNG CCS was manufactured by the panel, and it was assembled with connecting members. The free boundary condition on the outer side of the LNG CCS is more realistic than the symmetric boundary condition. The boundary conditions of the flat-flexible CCS model used in the water hitting simulation are indicated in Fig. 17.

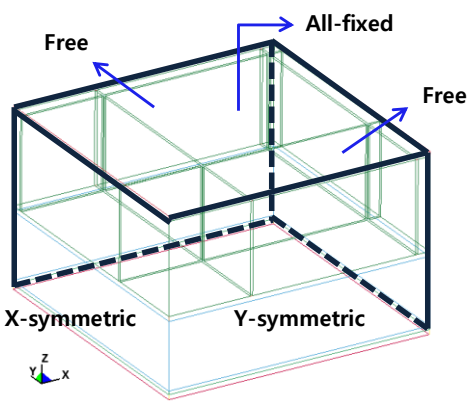

Fig. 17. Boundary conditions of flat-flexible CCS model

To observe the effect of hydroelasticity, the flat-rigid plate case was additionally simulated. In this case, only the structure model was changed, from a flat-flexible CCS to a flat-rigid plate, and the all-fixed boundary condition was applied to the entire flat-rigid plate. The size of the flat-rigid plate was equal to the size of the primary

layer. The pressure calculated from the flat-rigid plate case is corresponded to the sloshing model test result, and the hydroelasticity effect was not considered in this case. By comparing it with the flat-flexible CCS case result calculated under the same conditions, the hydroelasticity effect could be derived. From this, structural safety assessment of the LNG CCS can be more precisely carried out by applying the hydroelasticity effect to design sloshing pressure.

2.3.2. Selection of water column dimensions and properties

When the sloshing phenomenon occurs, several types of hitting modes are generated on the side flat regions and upper corner regions of the LNG CCS (DNVGL [12], Arai et al. [39]). Each hitting mode has a different impact velocity, incident angle and fluid shape. In the flat region, a certain lumped mass of LNG hits the primary layer of the LNG CCS at various incident angles and velocities. LNG rising up through flat region creates pressure on the upper corner region. The proper water column dimensions and properties should be determined to realize those kinds of general hitting modes.

In the upper corner region, the fluid volume rising up the side wall of LNG CCS causes sloshing phenomenon. The fluid cannot move in the vertical direction of the surface where the fluid and side wall contact. It is reasonable to apply a symmetric boundary condition to the water column surface in contact with the side wall of LNG CCS.

On the other hand, the sloshing phenomenon that occurs in the side flat region of LNG CCS is generated by fluid volumes having various shapes. Selecting the suitable shapes of the fluid volumes and consider its influence from experimental or numerical approach are quite controversial issue. In this research, focusing on the investigation of effect LNG CCS flexibility, the water column shape was simply assumed to be a wedge shape.

A total of five variables, specifically breadth (B), width (W), height(H), deadrise angle(β) and velocity of water column(V_i), were selected for the water hitting simulation, as shown in Fig. 18. The effect of incident angle could be considered by changing the deadrise angle of the water column. The differences in the fluid properties of LNG and water were neglected.

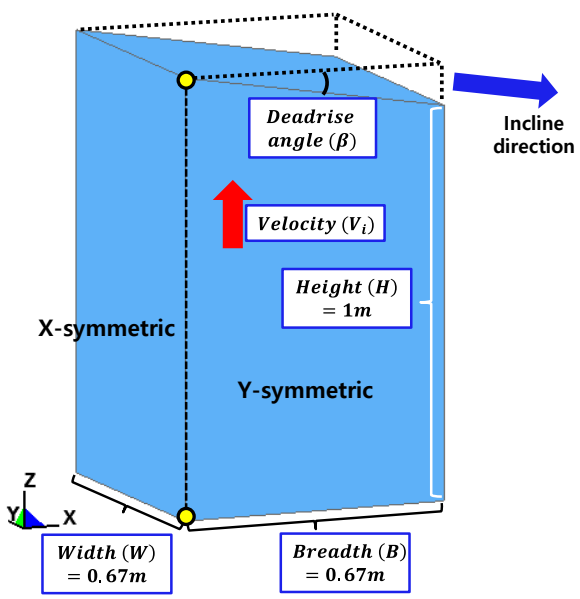

Fig. 18. Variables for definition of water column

The LNG CCS model applied to the water hitting simulation is one panel of the KC-1-type LNG CCS, which is the largest pressure measurement area in the sloshing model test. The obtained design sloshing pressure was applied evenly to the entire primary layer for the static or transient analysis. In order to generate pressure throughout the primary layer by water hitting, the breadth and width of the water column were selected so as to be equal to the same size of primary layer. In the water hitting simulation, the quarter model of one panel of KC-1 type LNG CCS was used with symmetric boundary conditions. Therefore, half length of the KC-1 type LNG CCS panel, 0.67m by 0.67m, was applied to the breadth and width of the water column.

The water spreading phenomenon was observed after the impact between the water column and the LNG CCS model. As the water spread, the hitting intensity changed at each position on the primary layer. The center region (P1) of the primary layer had a larger hitting intensity than did the outer region (P2). The larger the hitting intensity, the greater the pressure. This water spreading effect was taken into account in the water hitting simulation.

If the water column height increases with fixed breadth and width, its kinetic energy also increases. This leads to the increment of the pressure acting on the LNG CCS. The applied pressure does not increase gradually with respect to water column height, since the water column is not a rigid body object. Beyond a certain water column height, the influence of the water flow generated on the bottom of the water column is negligible for impact pressure. The

pressure change according to the height of water column was examined with the other conditions remaining fixed. The velocity of water column was selected as 7.65m/s and used in the wet drop simulation. Fig. 19 represents the correlation between the water column height and the averaged pressure of entire primary layer of the KC-1-type LNG CCS model. It can be seen that the pressure converged around 1m water column height. The standard value of water column height was chosen as 1m.

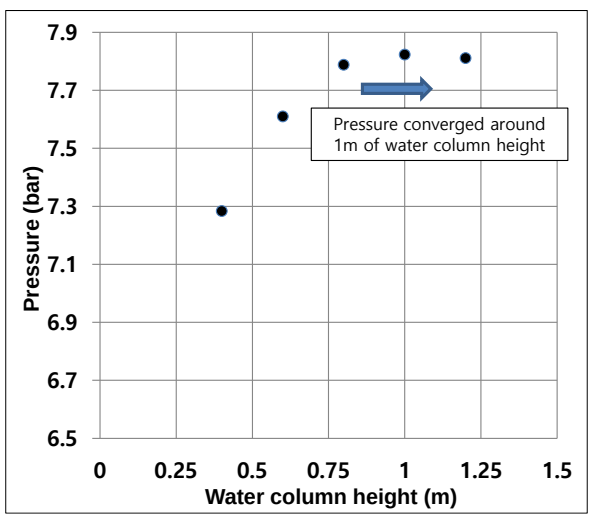

Fig. 19. Correlation between water column height and applied pressure

Fig. 20 illustrates the selected water column dimensions. The breadth, width and height of the water column were fixed among the five variables existing in the water hitting simulation. The fluid hitting the primary layer of the LNG CCS will have a diverse curved shape in the actual sloshing phenomenon. There is a limitation to the

consideration of all kinds of fluid shapes in numerical simulation. Therefore, the shape of water column was assumed as a cuboid type with an inclined plane. The remaining two variables, namely deadrise angle and velocity of water column, are considerably important factors for determination of the rising time and peak value of the pressure profile.

The contact between the primary layer of the LNG CCS and the water column does not occur simultaneously but sequentially, when the deadrise angle is larger than 0 degrees. The top of the inclined surface of the water column first contacted the primary layer, and then the contact area expanded in the incline direction, as shown in Fig. 18. The continuous contact made the time of peak pressure occurring in the primary layer different along the inclined direction. For instance, the peak pressure occurred earlier in the center region of primary layer(P1) than in the outer region(P2). The two locations are depicted in Fig. 20. Thus, the peak value of averaged pressure on the primary layer was reduced, and occurrence of peak pressure was delayed. This effect increases as the deadrise angle of the water column increases.

In several actual sloshing model tests, the impact conditions for various incident angles were observed, which varied the rising time of the measured sloshing pressures. Rising times and peak values tend to be inversely proportional to each other in measured sloshing pressures. Typical design sloshing pressures have rising times between 1ms and 10ms. A total of four deadrise angles, 0°, 4°, 7°

and 10°, were chosen in the water hitting simulation to cover the general range of design sloshing pressure rising time. When the deadrise angle is 0°, a pressure profile with a rising time close to 1ms was obtained. As the deadrise angle increases, the rising time increased, and a rising time of about 8 to 10ms appeared at 10° of deadrise angle.

The velocity of water column has a direct influence on the peak value of impact pressure. From the change of the deadrise angle and the velocity of the water column, several types of pressure profile defined by rising time and peak value can be produced. Since the velocity of water column also affects rising time, it is difficult to control rising time and peak value of impact pressure independently. In order to contain the peak values of the KC-1-type LNG CCS design sloshing pressures that exist between 4 to 20bar, a total of four velocities (i.e. 7.65, 8.65, 9.65, and 10.65m/s) were adopted in the water hitting simulation.

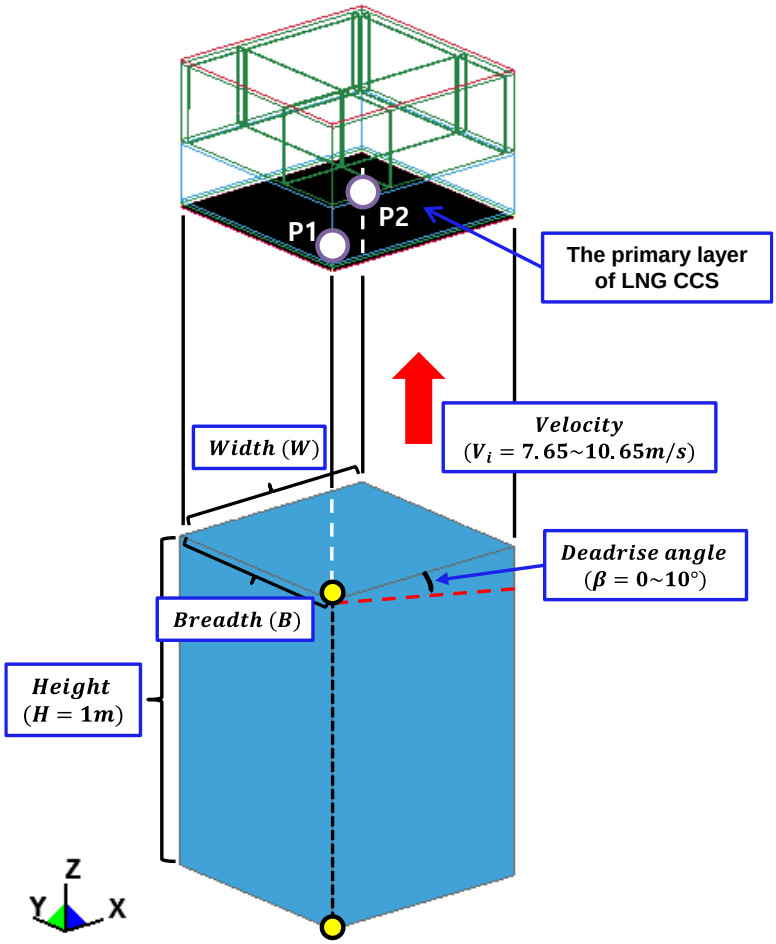

Fig. 20. Selected water column dimensions

A total of 16 water column cases were generated as summarized in Table 3. The water hitting simulations were performed using these water columns with two different structure models: flat-rigid plate and flat-flexible CCS. The hydroelasticity effect of the KC-1-type LNG CCS was derived from a comparison of these two models' results. Based on the flat-rigid plate model results, a specific water column generating the design sloshing pressure obtained from the sloshing model test could be selected. By applying this water column

to the flat-flexible CCS model, the hydroelasticity effect on the specific design sloshing pressure could be judged more precisely.

Table 3. Information on generated water columns

Velocity (V_i) (m/s)	Deadrise angle (β) (degree)			
	0	4	7	10
7.65	WC1-1 (case1)	WC2-1 (case5)	WC3-1 (case9)	WC4-1 (case13)
8.65	WC1-2 (case2)	WC2-2 (case6)	WC3-2 (case10)	WC4-2 (case14)
9.65	WC1-3 (case3)	WC2-3 (case7)	WC3-3 (case11)	WC4-3 (case15)
10.65	WC1-4 (case4)	WC2-4 (case8)	WC3-4 (case12)	WC4-4 (case16)

2.3.3. Hydroelasticity effect on sloshing pressure

A number of sloshing model tests were performed to identify the design sloshing loads during the lifetime of an LNG carrier. Measured and calculated sloshing pressures are normally obtained from a flat-rigid plate. The LNG CCS, which consists of thin metal membranes and insulation materials, is more flexible than a steel hull structure. This means that consideration of the hydroelasticity effect on sloshing pressures is needed in order to perform structural safety assessment of the LNG CCS. To investigate the hydroelasticity effect on sloshing pressure, water hitting simulations were conducted for the two different models (i.e. the flat-rigid plate model and the flat-flexible CCS model) with 16 different types of water columns.

2.3.3.1. Selection of pressure calculation regions

The sloshing pressures were measured for several regions in the sloshing model test. The larger the region of sloshing pressure measurement, the smaller the peak value and the longer the duration time. To measure sloshing pressure, a total of three regions were selected in the KC-1-type LNG CCS sloshing model test on the basis of one panel size. The design sloshing pressures used to assess structural safety of LNG CCS were derived for each region. Pressure calculation was performed in the water hitting simulation for the areas of the same size as the pressure measurement areas selected in the sloshing model test. The size of the LNG CCS model was equal to one panel size, so that the regions for pressure calculation were selected as shown in Fig. 21. The selected regions were named 1 × 1 region, 2 × 2 region and 3 × 3 region, respectively, in order of size. The 1 x 1 region corresponds to the smallest pressure measurement area in the sloshing model test, and the 3 x 3 region, the entire area of the one panel, corresponds to the largest pressure measurement area.

The 1×1 region, as the center region of the LNG CCS model, had a higher hitting intensity than the other regions when the water column impact occurred. The highest peak pressure was obtained in this region, while relatively small peak pressures were calculated in the 2×2 and 3×3 regions. This tendency is identical to the sloshing model test results. If the water column has a positive deadrise angle, the occurrence of full contact between the selected region and the water column is delayed, as the selected region is larger. As a result, in the

flat-flexible CCS model, the impact-caused vibrational structural response of the primary layer had a significant effect on the pressure results calculated in the 2×2 and 3×3 regions. For all of the water hitting simulation cases, pressure was calculated for each of the three selected regions, and then the effect of the size of the selected region was analyzed.

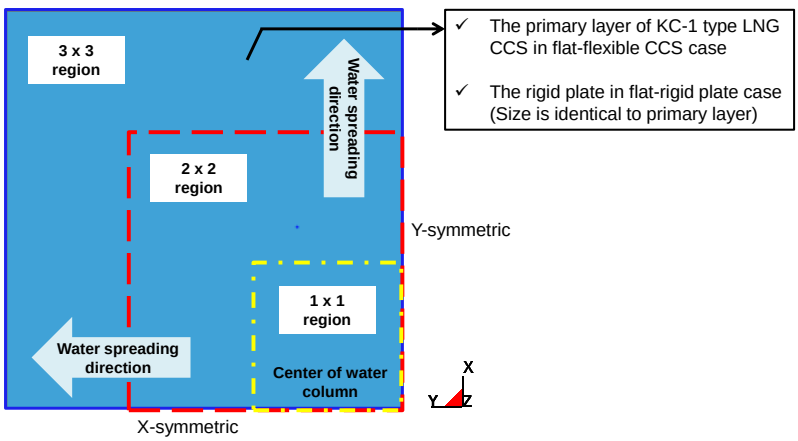

Fig. 21. Selected regions for pressure calculation

2.3.3.2. Results for flat-rigid plate model

The pressure profile calculated from the numerical simulation contained noise, which led to an unexpected error in the extraction of peak pressure and rising time. Especially, as shown in Fig. 22, the rising time determined from the peak value and half peak value (ABS [10]) is very sensitive to the shape of the peak region. Fig. 23 represents the comparison of raw data and 10-point averaged data for each of the two models. In the flat-rigid plate model, the difference between raw data and filtered data was not large, whereas

in the flat-flexible CCS model, noise in the peak region was relieved by filtering. This leads to reducing the uncertainty inherent in rising time decision. Peak pressure value was not significantly affected by filtering in the both models. When the filter was applied, the data time step was 0.1ms, which is a value that can obtain a non-distorted pressure profile in FSI analysis. Thus, a 10-point average filter was used in the both models to reduce the effect of noise.

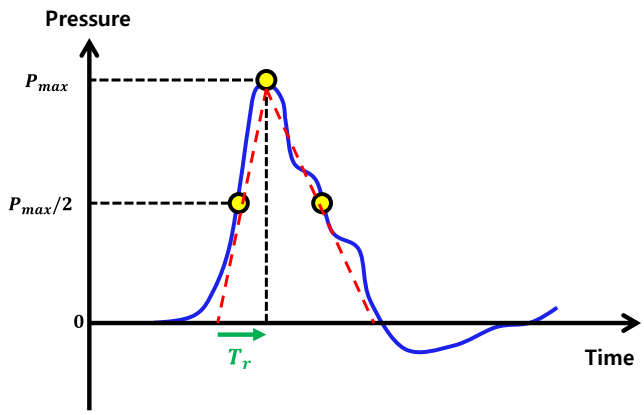

Fig. 22. Determination of rising time from pressure profile

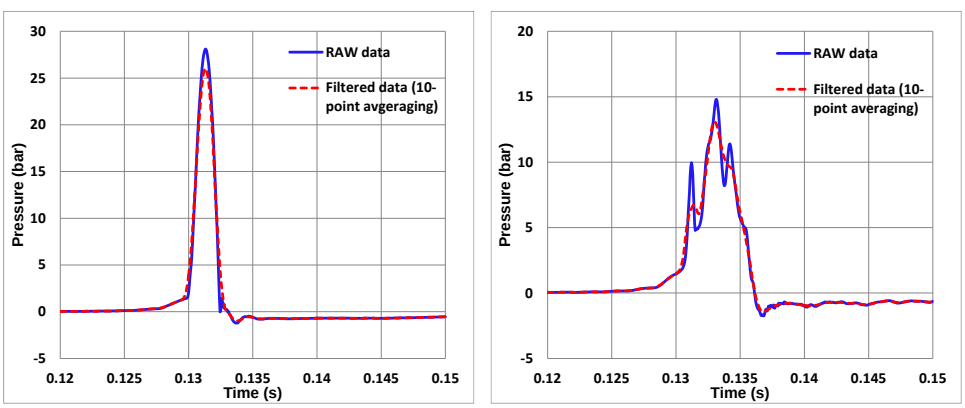

(a) Flat-rigid plate model (b) Flat-flexible CCS model

Fig. 23. Comparison of raw data and filtered data (case1)

Fig. 24 shows the calculated peak pressure results for the flat-rigid plate model with respect to the 16 water columns and 3 selected regions. The impact energy, which is equal to the initial kinetic energy of the water column, was determined from the square of the water column velocity. This impact energy is the most important factor in determining the peak pressure generated on a plate. It was found that, by means of a regression analysis, that the peak pressure is proportional to the square of the water column velocity.

The peak pressure tends to decrease as the deadrise angle of water column increases. In the case of the zero deadrise angle, a considerably large peak pressure was obtained relative to the other cases. For instance, the water column with zero deadrise angle and a velocity of 7.65m/s induced larger peak pressure than did the water column with a deadrise angle of 4 degrees and a velocity of 10.65m/s. The incident angle of impact in the sloshing phenomenon is also a critical factor when it comes to determining the peak pressure.

Different peak pressures are calculated according to the selected region. Plate deformation did not occur in the flat-rigid plate model, and so the pressures were not influenced by plate vibration. The only factor determining peak pressure according to the selected regions was the hitting intensity between the plate and the water column. The 1 x 1 region was in contact with the center of the water column, which generated the highest hitting intensity. The hitting intensity became smaller in the outer region of the plate, due to the water spreading effect. At the edge of the 3 x 3 region, which was outside the boundary of one panel of the KC-1-type LNG CCS, the smallest

hitting intensity was observed. The location of center region of the water column and the water spreading direction are illustrated in Fig. 21. As a result, large peak pressures were calculated in the following order: 1 x 1 region, 2 x 2 region, 3 x 3 region.

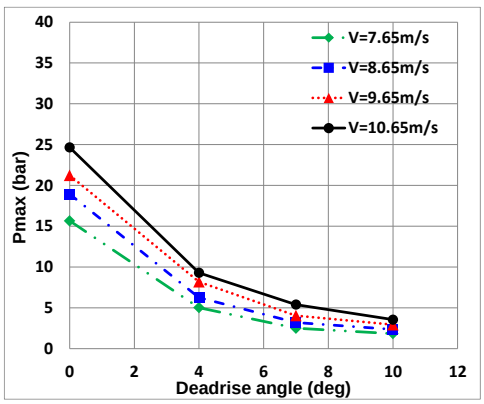

(a) FR, 3×3 region, Pmax

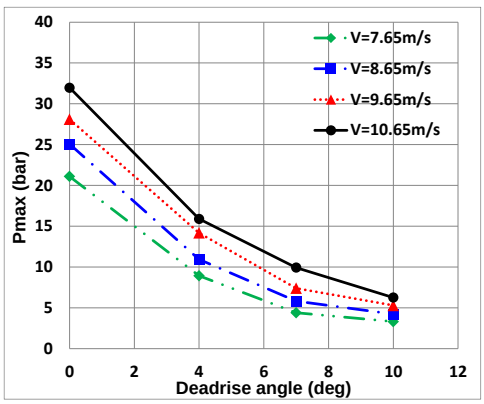

(b) FR, 2×2 region, Pmax

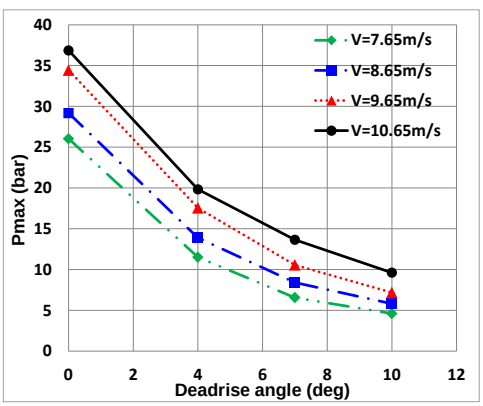

(c) FR, 1×1 region, Pmax

Fig. 24. Summarized peak pressure results for flat-rigid plate cases (FR: flat-rigid plate, Pmax: peak pressure)

The rising times calculated from the flat-rigid plate model are summarized in Fig. 25. The velocity and deadrise angle of water column affected the rising time of the impact pressure. However, the

effect of water column velocity on rising time was not significant. The deadrise angle of water column was a relatively more dominant factor. Especially, looking at the cases of 0 and 4 degrees of deadrise angle, an almost-constant rising time was obtained regardless of water column velocity in all three regions. When the deadrise angle was 10 degrees in 3 x 3 region, an almost quasi-static pressure profile, which had a 6 to 10ms rising time, was obtained.

The smaller the selected region, the shorter the rising time. this tendency was evident in the large deadrise angle cases. In the 1 x 1 region, a fairly constant rising time was observed regardless of the deadrise angle. Since the 1 x 1 region was located at the center of the water column, the contact between the flat-rigid plate and the water column was less affected by the deadrise angle than the cases of the 2 x 2 or 3 x 3 region.

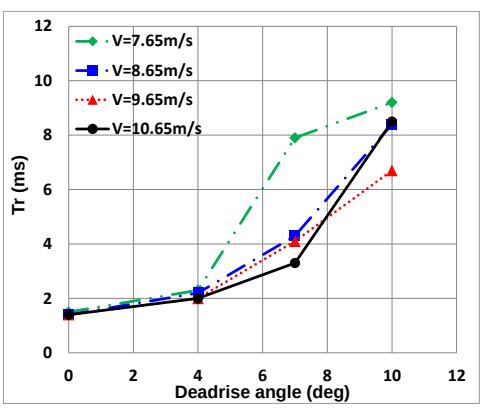

(a) FR, 3×3 region, Tr

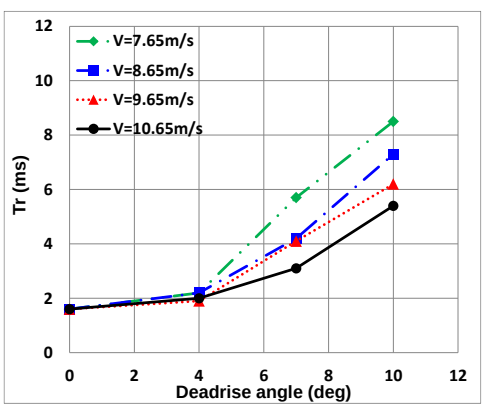

(b) FR, 2×2 region, Tr

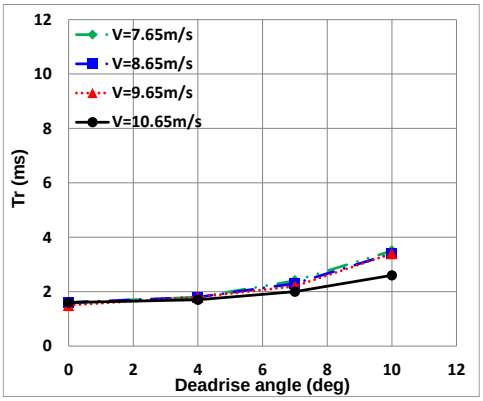

(c) FR, 1×1 region, Tr

Fig. 25. Summarized rising time results for flat-rigid plate cases (FR: flat-rigid plate, Tr: rising time)

Fig. 26 displays the pressure profiles according to the selected regions. The deadrise angle of water column was fixed at zero degrees. The velocity of the water column determines when the impact occurs. Thus, the peak pressure was generated first at a velocity of 10.65m/s. The noise was barely observed in not only the pressure profile of raw data but also that of filtered data as shown in Fig. 23(a), due to the non-occurrence of displacement on the flat-rigid plate. The negative pressure induced by the suction effect also did not appear. It can be seen that the pressure profile has a symmetrical shape with little skewness.

The pressure profiles according to the deadrise angles are shown in Fig. 27. The rising time and duration time of the pressure profile became longer as the deadrise angle increased. Skewness of pressure profile was observed in the positive deadrise angle cases. After the peak, the pressure oscillated and then converged to zero.

This pressure profile was similar to that obtained from the wet drop test of the wedge-shaped steel plate (Ahn and Kwon [32]).

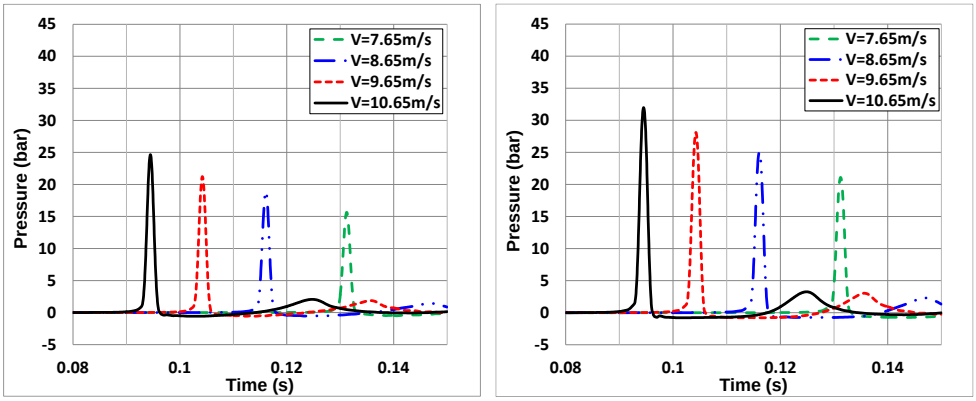

(a) 3×3 region (b) 2×2 region

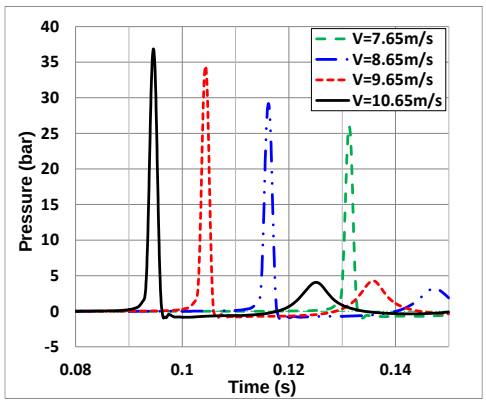

(c) 1×1 region

Fig. 26. Pressure profiles according to selected region (Flat-rigid plate model, Deadrise angle 0°)

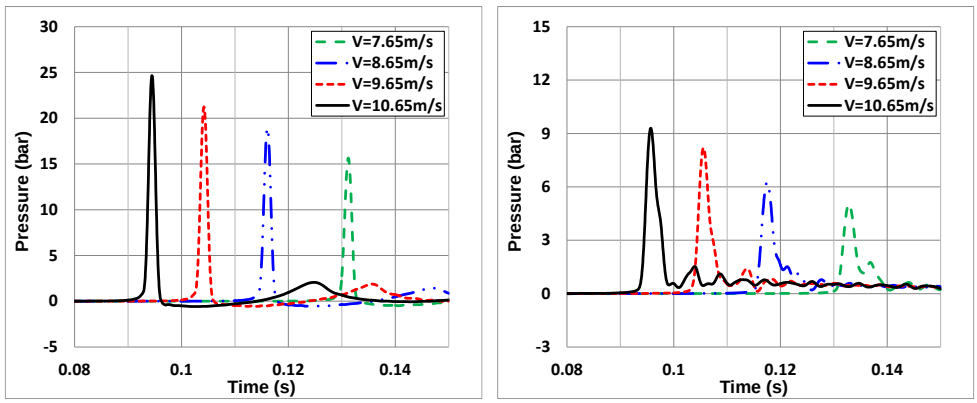

(a) Deadrise angle 0° (b) Deadrise angle 4°

(c) Deadrise angle 7° (d) Deadrise angle 10°

Fig. 27. Pressure profiles according to deadrise angle (Flat-rigid plate model, 3×3 region)

The following conclusions could be drawn from the flat-rigid plate model results.

- The peak pressure increases and the rising time tends to decrease as the velocity of the water column increases. However, the effect on rising time is not critical.
- The larger the deadrise angle of the water column, the lower the peak pressure and the longer the rising time. The deadrise angle of water column is the most dominant factor in determining the rising

time. It also has a significant effect on the peak pressure.

- The smaller the selected region, the higher the peak pressure and the shorter the rising time.
- There is nearly no noise in the calculated pressure profile.
- The negative pressure due to the suction effect is hardly observed in the calculated pressure profile.
- The shape of calculated pressure profile is symmetric under the zero deadrise angle condition. If the deadrise angle is greater than zero degrees, pressure profile skewness appears.

2.3.3.3. Results for flat-flexible CCS model

The actual KC-1-type LNG CCS model, except for corrugation, was applied as the structure part in the flat-flexible CCS analysis. Like the flat-rigid plate model, a 10-point average filter was applied to the pressure profile of the flat-flexible CCS model. Fig. 28 shows the calculated peak pressures of the flat-flexible CCS model for 16 water columns and three selected regions. As with the results for the flat-rigid plate model, increasing the velocity of the water column or decreasing its deadrise angle causes the increment of peak pressure. The degree of influence of water column velocity on the magnitude of peak pressure was similar in the flat-rigid plate model and the flat-flexible CCS model. The effect of deadrise angle of water column was relatively small in the flat-flexible CCS model. In the results for the flat-rigid plate model, the peak pressure difference between the deadrise angles of zero and 10 degrees was about 7.73 to 9.24 times for the 3 x 3 region. On the other hand, the flat-flexible

CCS model results showed a difference of only about 3.23 to 3.63 times. The peak pressure did not increase rapidly in the flat-flexible CCS model, even when the deadrise angle approached zero degrees.

At the deadrise angles of 0 and 4 degrees, a larger peak pressure was calculated in the flat-rigid plate model than in the flat-flexible CCS model. The smaller the deadrise angle, the smaller the effect of water spreading. When the deadrise angle was 0 degrees, only the vertical flexibility of the LNG CCS affected the pressure difference. If the impact by sloshing is generated on the entire primary layer simultaneously, the actual sloshing peak pressure will be smaller than the design sloshing pressure obtained from the sloshing model test.

In the case of a positive deadrise angle, the impact between the water column and the entire primary layer did not occur at the same time, but rather, continuous contact occurred. The larger the deadrise angle, the longer the duration of continuous contact. In addition to the vertical flexibility of the LNG CCS, the structural response of LNG CCS caused by continuous contact, e.g. vibration in the direction of water spreading, affected the determination of the pressure profile. The effect of water spreading was significant when the deadrise angle was 7 or 10 degrees and the selected region was the 2 x 2 or 3 x 3 region. In these cases, a larger peak pressure was obtained in the flat-flexible CCS model than in the flat-rigid plate model.

However, when the 1 x 1 region was selected and the deadrise angle was small, high peak pressure was generated on the primary layer of the LNG CCS. Such pressure induces severe damage to the LNG CCS compared to pressures which have a small peak pressure

and a relatively long rising time, thus, has an important influence on the LNG CCS structural safety assessemnt. Looking at Fig. 24 and Fig. 28, the larger the peak pressure, the greater the peak reduction due to the hydroelasticity effect. The excessive LNG CCS design caused by the design sloshing pressures having high peak can be relaxed by considering the hydroelasticity effect.

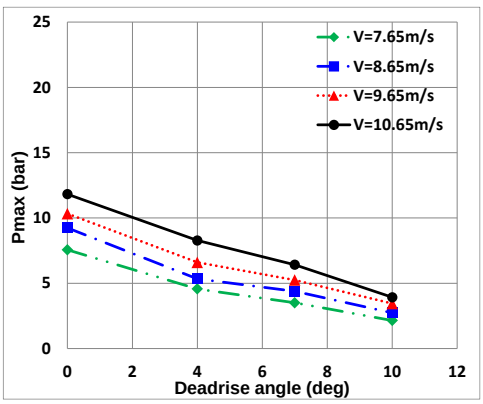

(a) FF, 3×3 region, Pmax

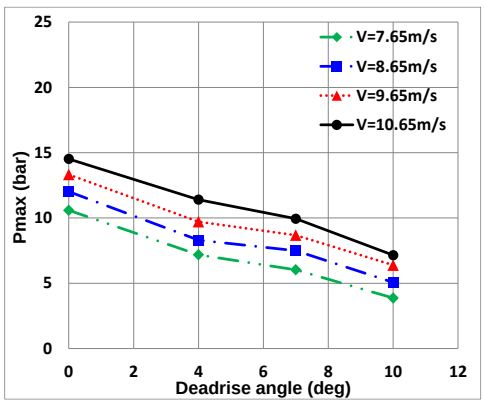

(b) FF, 2×2 region, Pmax

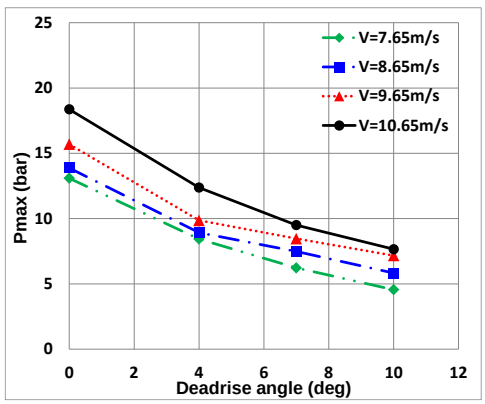

(c) FF, 1×1 region, Pmax

Fig. 28. Summarized peak pressure results for flat-flexible CCS cases (FF: flat-flexible CCS, Pmax: peak pressure)

The rising times calculated from the flat-flexible CCS model are summarized in Fig. 29. As the velocity of water column decreases and the deadrise angle of water column increases, the rising time tends to increase. However, the influence of the velocity of water column is small in a relative sense. The rising time does not change substantially depending on the hitting conditions in the results for the 1 x 1 region. The difference in rising time between the flat-rigid plate model and the flat-flexible CCS model is apparent under the zero deadrise angle condition. This means that the hydroelasticity effect can increase the rising time of sloshing pressure provided that the incident angle of impact is small. Looking at the results for the 2 x 2 region with zero deadrise angle and the 3 x 3 region with a 4 degree deadrise angle, a value deviating from the overall tendency was observed when the water column velocity was 10.65m/s. These results reflected the shape of the peak region. In the flat-flexible CCS model, the vertical vibration of the LNG CCS caused by the impact with the water column contributed to the noise generation of the pressure profile. Therefore, the pressure profile calculated from the flat-flexible CCS model contained some noise around the peak, unlike the corresponding case in the flat-rigid plate model. In the pressure profile, the rising time was determined by the half of peak pressure and peak pressure as shown in Fig. 22, which are very sensitive to the shape of the peak region. Even though the point averaging filter was utilized to reduce the influence of noise on the determination of rising time, the rising time result was, as inevitably, uncertain.

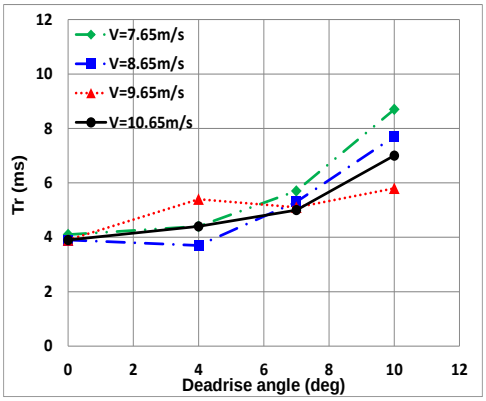

(a) FF, 3×3 region, Tr

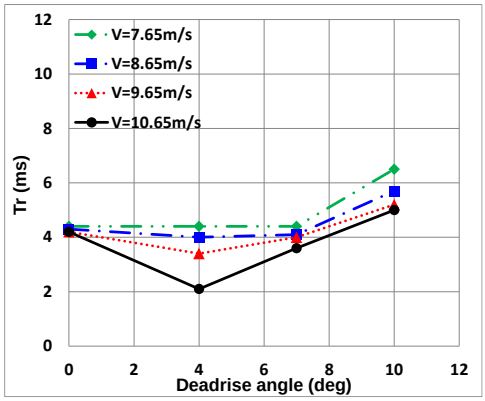

(b) FF, 2×2 region, Tr

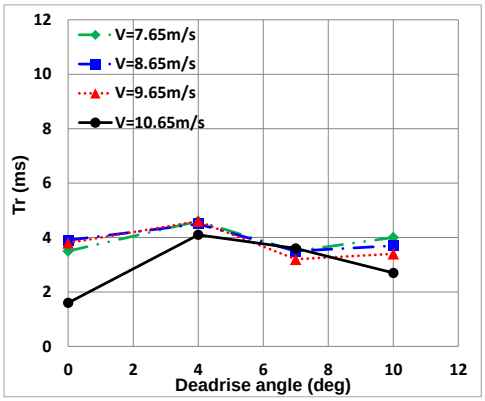

(c) FF, 1×1 region, Tr

Fig. 29. Summarized rising time results for flat-flexible CCS cases (FF: flat-flexible CCS, Tr: rising time)

The pressure profiles according to the selected region are shown in Fig. 30. The deadrise angle of water column was zero degrees. The smaller selected region generated the higher peak pressure. This tendency is the same as that seen in the flat-rigid plate model results. The interaction between the displacement of flat-flexible CCS and the impact pressure occurred at each time step. Thus, it was observed that some noise had occurred in the peak region, in contrast with the results for the flat-rigid plate model. In particular, noise was

more severe in the 1 x 1 region where vertical displacement was relatively large due to the high hitting intensity. After the peak pressure occurred, the pressure dropped and a slight negative pressure appeared. The shape of pressure profile was almost symmetrical.

The pressure profiles according to the deadrise angle are displayed in Fig. 31. The pressure measurement area selected was the 3 x 3 region. The rising time and duration time became longer as the deadrise angle increased, in common with the results for the flat-rigid plate model. The change of deadrise angle did not significantly affect the skewness of the pressure profile. In the case of deadrise angles of 7 and 10 degrees, noise in the pressure profile barely appeared. The larger the deadrise angle, the longer the impact duration, which mitigates the LNG CCS model's rapid displacement and vibration with short duration.

No damping effect was considered in the water hitting simulation. When the deadrise angle is 7° and 10°, some oscillation having a specific magnitude was observed after the first peak. If an appropriate damping factor is applied to the penalty coupling (Aquelet et al. [21]) or suitable proportional damping is applied to the LNG CCS, the magnitude of oscillation is expected to be reduced.

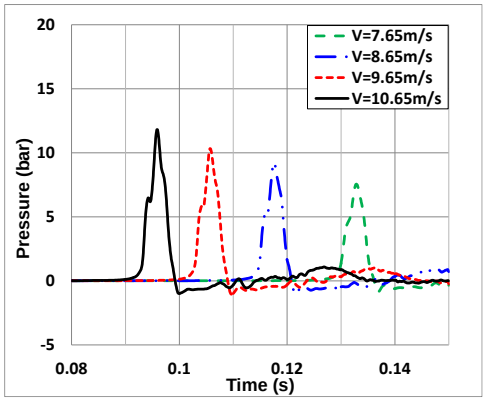

(a) 3×3 region

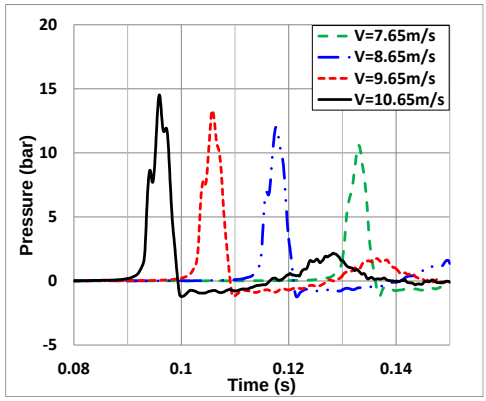

(b) 2×2 region

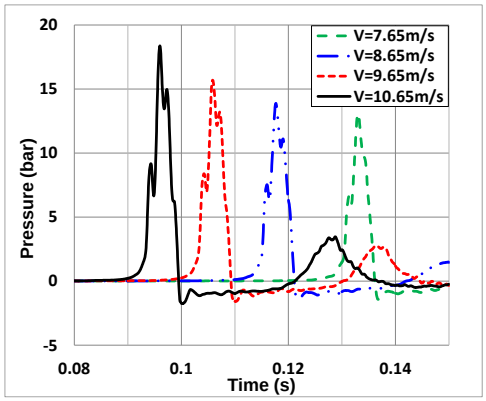

(c) 1×1 region

Fig. 30. Pressure profiles according to selected region (Flat-flexible CCS model, Deadrise angle 0°)

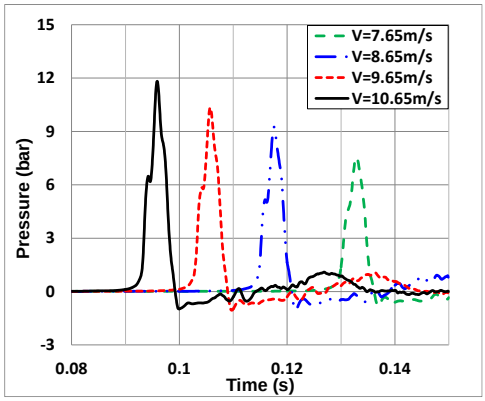

(a) Deadrise angle 0°

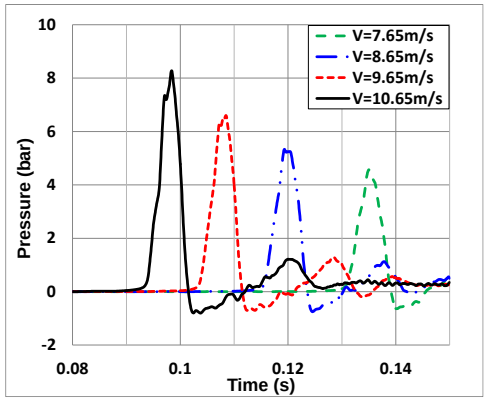

(b) Deadrise angle 4°

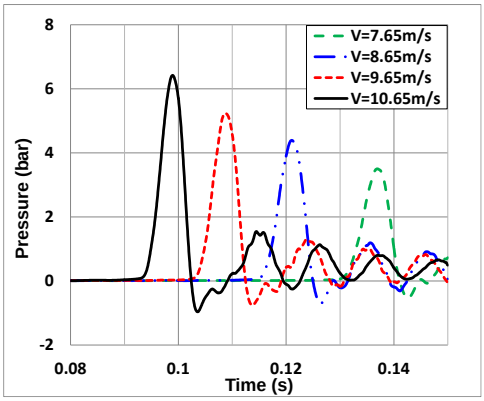

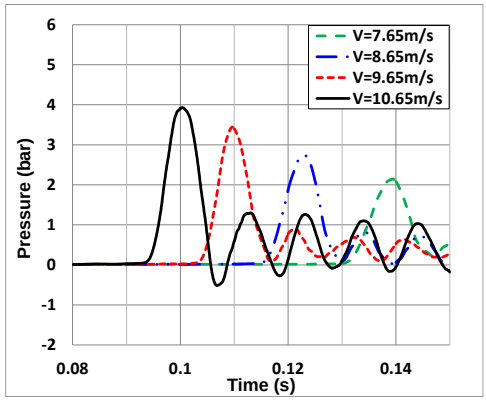

(c) Deadrise angle 7° (d) Deadrise angle 10°

Fig. 31. Pressure profiles according to deadrise angle (Flat-flexible CCS model, 3 x 3 region)

The following conclusions could be drawn from the flat-flexible CCS model results.

- The peak pressure decreases and rising time increases as the deadrise angle of water column becomes larger. The deadrise angle of water column is important for determining rising time but also for determining peak pressure. However, the effect of deadrise angle on rising time is small relative to the flat-rigid plate model. The variation of the pressure profile according to the hitting condition is reduced by the hydroelasticity effect.

- Compared to the flat-rigid plate model, some noise is observed in the pressure profile of the flat-flexible CCS model. The calculation of rising time is sensitive to the shape of the peak pressure region due to noise occurrence. The intensity of noise decreases as the deadrise angle increases.

- In the 1 x 1 region where the highest pressure is obtained, the

flat-flexible CCS model has relatively less peak pressure than the flat-rigid plate model. That is, in the case of the design sloshing pressure with a large peak value, the peak pressure reduction due to the hydroelasticity effect appears significantly.

- When the deadrise angle is zero degrees, a longer rising time is obtained in the flat-flexible CCS model than in the flat-rigid plate model. This difference becomes smaller as the deadrise angle increases. In the sloshing pressure where the rising time is short and peak value is large, the importance of hydroelasticity effect becomes greater.

- The negative pressure on the pressure profile is observed. It can be judged that the LNG CCS behavior after the impact causes negative pressure.

- Unlike the flat-rigid plate model, the pressure profile has almost symmetrical shape regardless of the deadrise angle, velocity, and selected region. It is believed that the hydroelasticity effect suppresses the occurrence of skewness on the pressure profile.

2.4. Structural safety assessment procedure for LNG CCS considering hydroelasticity effect

From the results of the water hitting simulations, it was determined that the hydroelasticity effect has a significant influence on the sloshing load. A quantitative evaluation of the hydroelasticity effect is required in order to apply it to LNG CCS design. Therefore, the concept of a correction factor was introduced for the peak value and

rising time of sloshing pressure, respectively. The correction factor is a variable that indicates the degree of sloshing pressure change due to the pure hydroelasticity effect. After calculating the correction factors for each of the 16 analysis cases, empirical formulas were derived to predict correction factors for arbitrary sloshing pressure. When using the empirical formulas, there is an advantage in that the hydroelasticity effect of the LNG CCS can be easily considered without any time-consuming fluid-structure interaction analysis. Based on these results, a structural safety assessment procedure for the LNG CCS considering the hydroelasticity effect was derived (and is proposed herein).

The suggested corrections factors are determined solely by the sloshing pressure characteristics. The effects of fluid compressibility, air pocket and aeration observed on the impact surface cannot be considered. Therefore, the use of correction factors is limited to pure impact conditions (Malencia et al. [36]) causing relatively large peak pressure.

2.4.1. Suggested correction factors and empirical formulas for estimation of hydroelasticity effect

The design sloshing pressure determined from the sloshing model test is the result of the flat-rigid plate model and needs to be modified by considering the hydroelasticity effect. When performing structural safety assessment of the LNG CCS, the design sloshing pressure is idealized into a triangular pressure profile (Nho et al.

[40], ABS [10]). This profile can be described in terms of three variables: peak pressure, rising time, and duration time. The peak pressure and rising time are relatively important factors for determining the structural response of the LNG CCS. Accordingly, the hydroelasticity effect was investigated in terms of the difference in peak pressure and rising time between the flat-rigid plate model and the flat-flexible CCS model. To quantify the hydroelasticity effect, two correction factor concepts were introduced. Eq. (3) and Eq. (4) show the definitions of correction factors for peak pressure and rising time, respectively. The corrected design sloshing pressure considering the hydroelasticity effect could be obtained by applying the following correction factors.

$$P_{FF} = C_{R-P} P_{FR} \cdots (3)$$

where,

P_{FR}: peak pressure calculated from flat rigid plate model

P_{FF}: peak pressure calculated from flat flexible CCS model

C_{R-P}: correction factor of peak pressure

$$Tr_{FF} = C_{R-T} Tr_{FR} = \cdots (4)$$

where,

Tr_{FR}: rising time calculated from flat rigid plate model

Tr_{FF}: rising time calculated from flat flexible CCS model

C_{R-T}: correction factor of rising time

A design sloshing pressure having a higher peak pressure and a

smaller rising time was obtained in the 1 x 1 region compared with the other pressure measurement regions. For quantitative evaluation of the hydroelasticity effect on the sloshing pressure, correction factors of peak pressure and rising time in the 1 x 1 region were calculated as shown in Tables 4 and 5. Fig. 32 shows the tendency of correction factors for deadrise angle and velocity. The correction factors of peak pressure(C_{R-P}) had a value of about 0.5 when the deadrise angle was zero. Conversely, the correction factors of rising time(C_{R-T}) had a value greater than 2 except when the velocity of water column was 10.65m/s. The zero deadrise angle cases generated larger peak pressure and shorter rising time than the other positive deadrise angle cases. This means that the impulse-type sloshing load, which is a critical factor for LNG CCS structural safety assessment, has a peak pressure decrease and a rising time increase due to the hydroelasticity effect. By considering the hydroelasticity effect, the impulse-type sloshing load is shifted to the quasi-static type, which leads to partial relief of the LNG CCS design burden.

The increment of the deadrise angle of water column results in the increase of the correction factor of peak pressure. When the deadrise angle of water column is larger than 10 degrees, the correction factor converges to 1. Increasing the deadrise angle leads to a decrease in peak pressure and an increase in rising tine. This means that the hydroelasticity effect is not large for sloshing pressure, which has a small peak pressure and a long rising time.

Table 4. Correction factors of peak pressure (C_{R-P}) for KC-1 type LNG CCS (1 x 1 region)

V (m/s)	dead rise angle (deg)			
	0	4	7	10
7.65	0.50	0.73	0.95	0.99
8.65	0.48	0.64	0.89	1.00
9.65	0.46	0.56	0.80	1.00
10.65	0.50	0.68	0.70	0.80

Table 5. Correction factors of rising time (C_{R-T}) for KC-1 type LNG CCS (1 x 1 region)

V (m/s)	dead rise angle (deg)			
	0	4	7	10
7.65	2.19	2.56	1.46	1.14
8.65	2.44	2.50	1.52	1.09
9.65	2.53	2.56	1.45	1.00
10.65	1.00	2.41	1.80	1.04

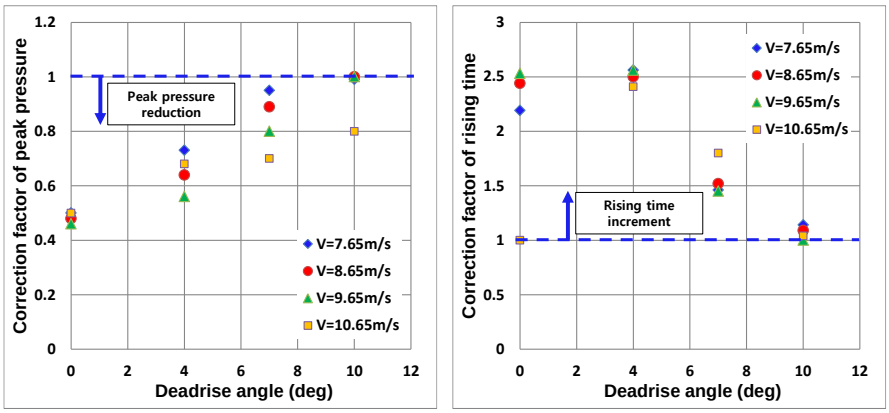

(a) C_{R-P} (b) C_{R-T}

Fig. 32. Calculated correction factors in 1 x 1 region

The correction factor varies depending on the sloshing pressure. In order to derive a correction factor corresponding to a specific sloshing pressure, it is necessary to select appropriate water column properties from a flat-rigid plate simulation. The repetitive fluid-structure interaction analysis is required in this step. Then, the flat-flexible CCS simulation should be performed by using the selected water column properties. The correction factor can be determined through comparison of the two sets of simulation results. In actual design, it is inefficient to perform a series of fluid-structure interaction analyses to calculate correction factors. If the explicit equations for calculation of correction factors are given, the hydroelasticity effect of the LNG CCS can be effectively considered in the actual design.

Empirical formulas in the forms of Eqs. (5) and (6) were devised to take into account the hydroelasticity effect of the LNG CCS without time-consuming FSI analysis. The KC-1-type LNG CCS was adopted in this research to derive the empirical formulas. Actually, each LNG CCS type has its own insulation system that determines the vertical flexibility, and the correction factors change according to the LNG CCS type. However, in various membrane-type LNG CCS, the properties of PUF and plywood constituting the insulation system are quite similar. Since the dominant factor determining the vertical flexibility of the LNG CCS is the composition of the insulation system, empirical formulas based on the KC-1-type LNG CCS can be utilized as a reference to consider the hydroelasticity effect of other types of LNG CCS. If the correlation between the vertical flexibility of the

LNG CCS and the correction factors is studied further, the utility of empirical formulas can be enhanced.

$$C_{R-P} = f(P_{FR}, Tr_{FR}) \cdots (5)$$

$$C_{R-T} = g(P_{FR}, Tr_{FR}) \cdots (6)$$

A regression analysis was conducted based on a total of 16 analysis results defined in Table 3. Empirical formulas were proposed for the three different selected regions where the pressure measurement sensors were attached in the KC-1-type LNG CCS sloshing model test. The sizes of the 1 x 1 and 2 x 2 regions depicted in Fig. 21 are 0.45m by 0.45m and 0.9m by 0.9m, respectively. The 3 x 3 region was selected as the entire area of the primary layer of the KC-1-type LNG CCS unit panel. The 2nd order polynomial type was applied to the correction factor of peak pressure (C_{R-P}), and the power law form was applied to the correction factor of rising time (C_{R-T}). Peak pressure was non-dimensionalized using the elastic modulus of PUF, which is the most important factor for determining the vertical flexibility of the LNG CCS. The natural period of the LNG CCS was applied to non-dimensionalized rising time. The results of the regression analysis are expressed in Eqs. (7) and (8).

$$C_{R-P_{11}} = -3.25 \cdot 10^0 \cdot \left(\frac{P_{FR}}{E_Z}\right) + 4.47 \cdot 10^1 \cdot \left(\frac{P_{FR}}{E_Z}\right)^2 - 2.16 \cdot 10^1 \cdot \left(\frac{P_{FR}}{E_Z}\right) \cdot \left(\frac{Tr_{FR}}{T_n}\right) + 4.77 \cdot 10^0 \cdot \left(\frac{Tr_{FR}}{T_n}\right) - 4.66 \cdot 10^0 \cdot \left(\frac{Tr_{FR}}{T_n}\right)^2$$

$$C_{R-P_{22}} = 7.46 \cdot 10^0 \cdot \left(\frac{P_{FR}}{E_Z}\right) - 5.81 \cdot 10^0 \cdot \left(\frac{P_{FR}}{E_Z}\right)^2 - 4.46 \cdot 10^1 \cdot \left(\frac{P_{FR}}{E_Z}\right) \cdot \left(\frac{Tr_{FR}}{T_n}\right) + 3.70 \cdot 10^0 \cdot \left(\frac{Tr_{FR}}{T_n}\right) - 1.91 \cdot 10^0 \cdot \left(\frac{Tr_{FR}}{T_n}\right)^2$$

$$C_{R-P_{33}} = 7.64 \cdot 10^0 \cdot \left(\frac{P_{FR}}{E_Z}\right) - 6.21 \cdot 10^1 \cdot \left(\frac{P_{FR}}{E_Z}\right)^2 - 2.89 \cdot 10^1 \cdot \left(\frac{P_{FR}}{E_Z}\right) \cdot \left(\frac{Tr_{FR}}{T_n}\right) + 3.33 \cdot 10^0 \cdot \left(\frac{Tr_{FR}}{T_n}\right) - 1.73 \cdot 10^0 \cdot \left(\frac{Tr_{FR}}{T_n}\right)^2 \cdots (7)$$

where,

C_{R-P_ii}: correction factor of peak pressure for i x i region

E_Z: elastic modulus of polyurethane foam (350bar in KC-1-type LNG CCS)

T_n: natural period of LNG CCS (6.57ms in KC-1-type LNG CCS)

$$C_{R-T_11} = 0.0643 \cdot \left(\frac{10 \cdot P_{FR}}{E_Z}\right)^{-0.5374} \cdot \left(\frac{Tr_{FR}}{T_n}\right)^{-2.4038}$$

$$C_{R-T_22} = 1.0259 \cdot \left(\frac{10 \cdot P_{FR}}{E_Z}\right)^{0.1868} \cdot \left(\frac{Tr_{FR}}{T_n}\right)^{-0.6734}$$

$$C_{R-T_33} = 1.0020 \cdot \left(\frac{10 \cdot P_{FR}}{E_Z}\right)^{0.0187} \cdot \left(\frac{Tr_{FR}}{T_n}\right)^{-0.6767} \cdots (8)$$

where,

C_{R-T_ii}: correction factor of rising time for i x i region

E_Z: elastic modulus of polyurethane foam (350bar in KC-1-type LNG CCS)

T_n: natural period of LNG CCS (6.57ms in KC-1-type LNG CCS)

There are two ways to calculate the natural period of the LNG CCS. The first method performs an eigenvalue analysis; however, it requires the FE model of the LNG CCS. As an alternative to the numerical approach, the natural period of the LNG CCS can be predicted by using the elastic modulus of PUF. The simple equation

for calculating the natural period of the LNG CCS is expressed in Eq. (9). In the present study, Eq. (9) was used to calculate the natural period of the KC−1−type LNG CCS.

$$T_n = 2\pi\sqrt{\frac{\overline{m}}{k}} = 2\pi\sqrt{\frac{mH}{E_Z A}} \cdots (9)$$

where,

E_Z: elastic modulus of polyurethane foam

A: area of primary layer

H: height (vertical length) of LNG CCS

The correction factors corresponding to the peak pressure and rising time of design sloshing pressure can be calculated from Eqs. (7) and (8). If the design sloshing pressure is corrected with these calculated correction factors, the hydroelasticity effect of the LNG CCS can be considered without any FSI analysis.

The various physical phenomenon, e.g. fluid compression, air cushion, aeration, thermal exchange can be observed in the actual sloshing (Malencia et al. [36]). The hydroelasticity effect may appear differently even at the same sloshing pressure due to the difference of impact condition entailing these phenomena. The correction factors calculated from Eqs. (7) and (8) is determined only by sloshing pressure characteristics. In the actual design stage, the design sloshing pressures critical to the safety assessment of LNG CCS are pressures having large peak value and short rising time. These critical design sloshing pressures are mainly generated by

pure impact where the effect of air pocket and aeration are quite small (Lee et al. [41]). Thus, the proposed correction factors can be practically used when performing transient analysis for critical design sloshing pressures. As the next step, if the relationship between these phenomena and the hydroelasticity effect can be derived, a more sophisticated pressure correction will be made for arbitrary sloshing pressures.

2.4.2. Suggested LNG CCS structural safety assessment procedure considering hydroelasticity effect

Fig. 33 displays the overall procedure for LNG CCS structural safety assessment with consideration of the hydroelasticity effect. A total of two additional procedures are proposed based on the fluid-structure interaction analysis model, correction factors and empirical formulas. The procedure named the Level IV method takes into account the hydroelasticity effect of the LNG CCS by performing a fluid-structure interaction analysis directly. If specific design sloshing pressure is given, the water column properties that return it are determined through the flat-rigid plate model. The flat-flexible CCS analysis is conducted by applying the determined water column properties, and structural safety assessment is carried out from the structural response that appears in the flat-flexible CCS analysis. This Level IV method is the most accurate method with which to consider the hydroelasticity effect of the LNG CCS. However, in order to determine the properties of the water column, it is necessary

to repeat the fluid-structure interaction analysis after changing the velocity and deadrise angle of the water column. In actual design, there are many types of design sloshing pressure, the result being that considering the hydroelasticity effect of the LNG CCS using the Level IV method is actually inefficient.

A procedure called the Level III method, which can be effectively used in actual design, was additionally suggested. In the Level III method, empirical formulas are used instead of fluid-structure interaction analysis to consider the hydroelasticity effect of the LNG CCS. Correction factors are calculated from the empirical formulas given in Eqs. (7) and (8). After that, they are applied to the design sloshing pressure to obtain the corrected design sloshing pressure. Using the corrected design sloshing pressure, structural safety assessment of the LNG CCS can be done by performing only transient analysis. Even if the accuracy of the Level III method is relatively lower than that of the Level IV method, time efficiency is greatly enhanced.

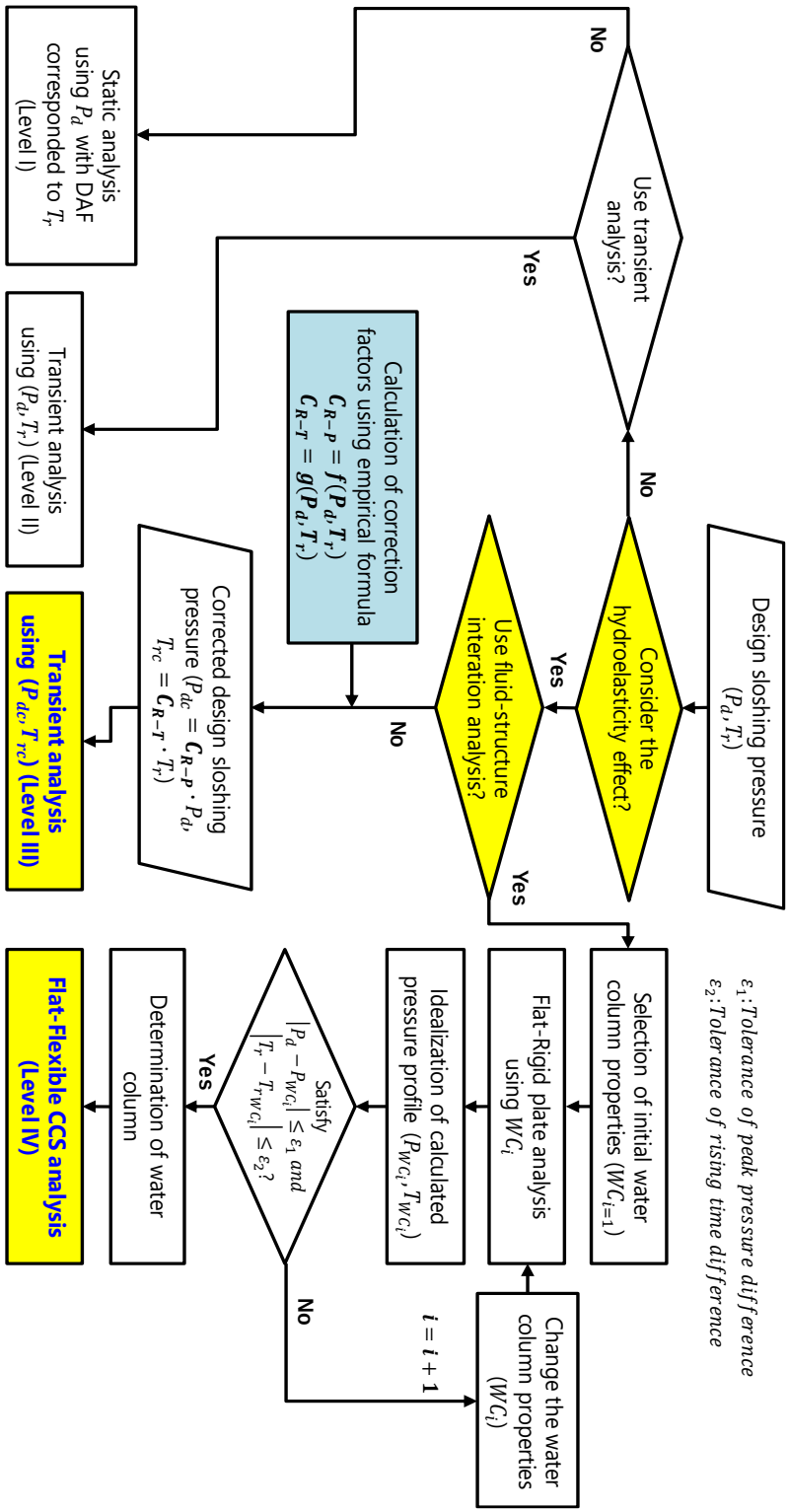

Fig. 33. Flowchart of LNG CCS strength assessment considering hydroelasticity effect

To verify the validity of the Level III method, a comparison with the Level IV method was performed for a total of three design sloshing pressures as shown in Table 6. Design sloshing pressure was selected for each pressure measurement region. In the Level IV method, the water column causes pressure distribution on the entire primary layer of the LNG CCS. On the other hand, in the Level III method, pressure is applied only on the selected region.

For direct comparison between the two method, a validation model called detached model was newly suggested as shown in Fig. 34. The water impact on outer region (outer of 1x1 or 2x2) has no effect on the deflection of detached area (1x1 or 2x2). In order to consider the continuity of insulation panel, symmetric boundary conditions were applied to the side of detached region (see Fig. 34).

The water hitting simulations were performed for the detached model and the original model, respectively, and the calculated pressures were compared (see Fig. 35). Almost identical peak pressures and rising times are obtained in both models. It is acceptable to apply empirical formulas (see Eqs. (7) and (8)) to the detached model.

Table 6. Generated cases for verification of Level III method

Case	Design sloshing pressure (DSP)			Corrected transient pressure (used in Level III method)			Water column properties (used in Level IV method)
Case 1 (1x1)	3x3	2x2	1x1	3x3	2x2	1x1	Deadrise angle = 0deg Velocity = 7.65m/s
	-	-	26.0bar / 1.6ms	-	-	13.0bar / 3.6ms	
Case 2 (2x2)	3x3	2x2		3x3	2x2		Deadrise angle = 7deg Velocity = 10.2m/s
	-	9.13bar / 3.2ms		-	8.85bar / 4.2ms		
Case 3 (3x3)	3x3			3x3			Deadrise angle = 10deg Velocity = 15m
	7.17bar / 3.6ms			7.96bar / 5.3ms			

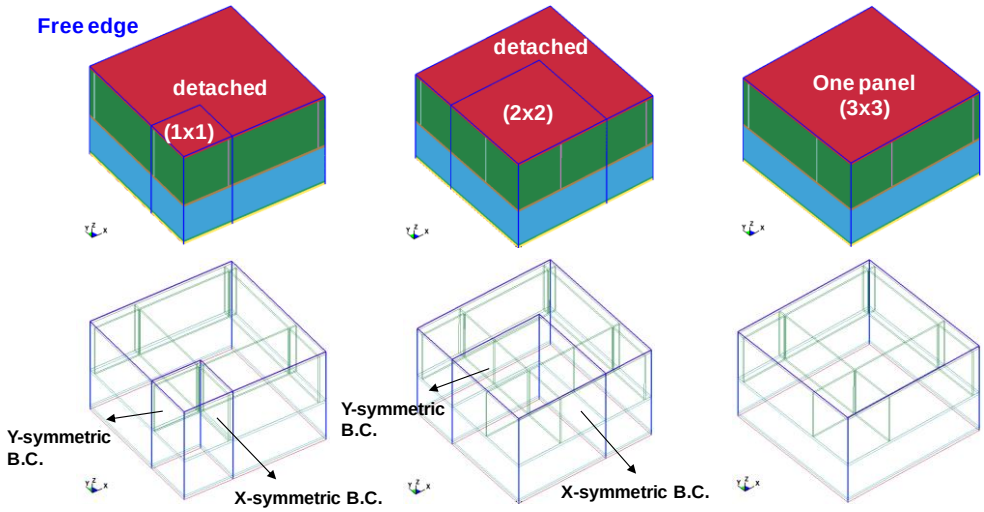

(a) 1x1 (b) 2x2 (c) 3x3

Fig. 34. Validation model (detached model)

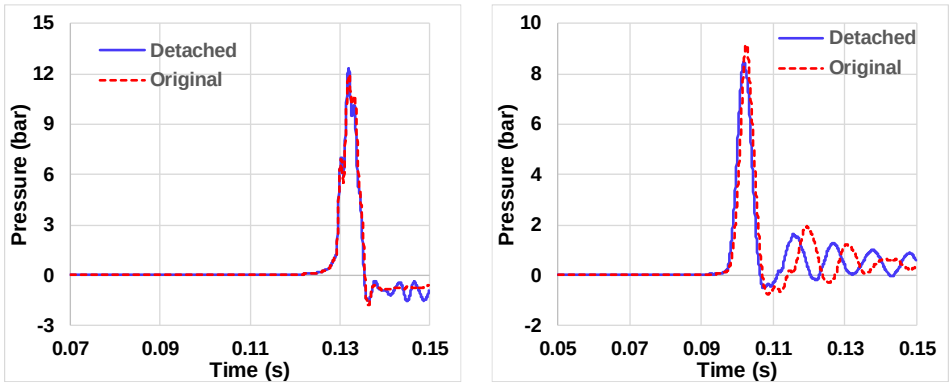

(a) Case1 (0deg,7.65m/s) (b) Case2 (7deg,10.2m/s)

Fig. 35. Comparison of pressure results (water hitting simulation)

In the transient analysis, the Belytscho-Tsay type was applied to 2D shell elements, and the constant-stress type was applied to 3D solid elements, as in the fluid-structure interaction analysis. It was confirmed that the difference between the case of using the quadratic 8-node hexahedron with the nodal rotations type derived from the 20-node hexahedron (which is solid element formulation No.3 provided by LS-dyna) and the case of using the constant-stress type was not significant.

The displacement results were compared at four locations on the primary layer, as shown in Fig. 36. The results are illustrated in Figs. 37 to 39. In the water hitting simulation, the pressure distribution on membrane is not uniform and has a high peak pressure in the center region. The design sloshing pressure is average value obtained over a specific area, not the value obtained at a point. Thus, averaging of displacement was conducted for the pressure measurement region corresponding to each case. In Case 1, using the design sloshing

pressure measured in the 1 x 1 region, displacement averaging was performed in locations A and B. In Case 3, all four locations A, B, C and D were adopted for calculation of average displacement. The averaged displacement results showed good agreement. According to these results, it was judged that use of the Level III method would be appropriate.

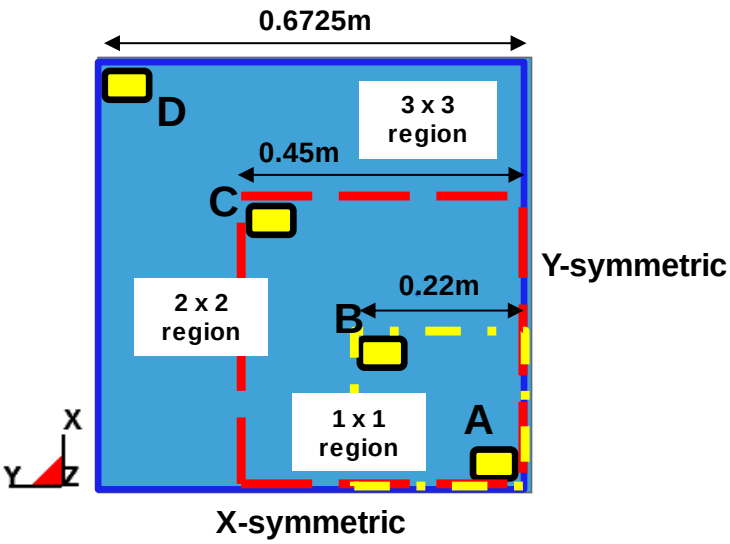

Fig. 36. Locations for displacement calculation

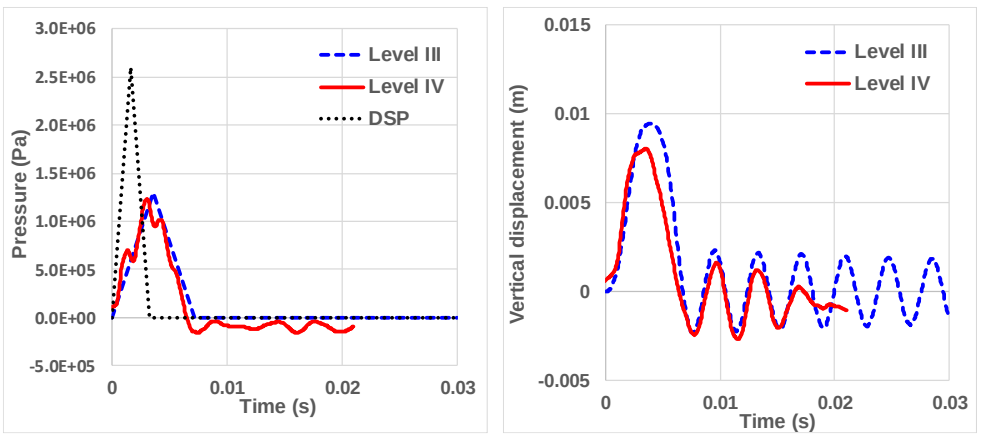

(a) Pressure (b) Averaged displacement

Fig. 37. Results comparison (Case 1)

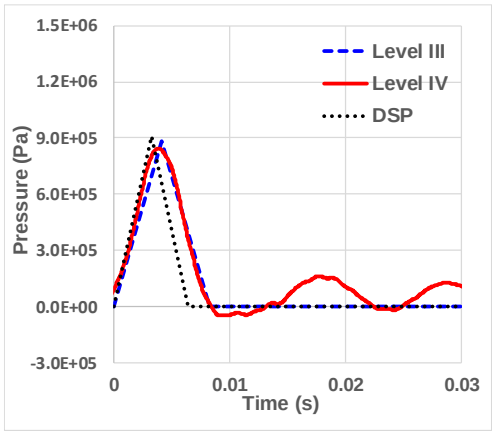

(a) Pressure

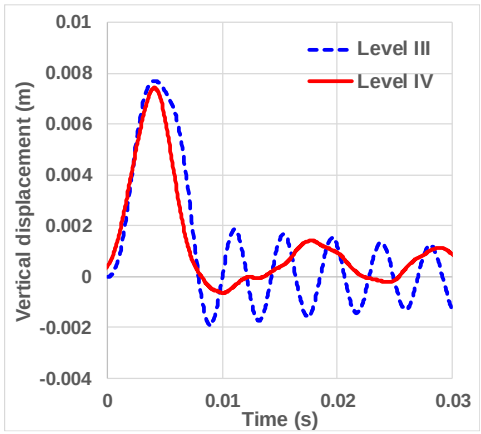

(b) Averaged displacement

Fig. 38. Results comparison (Case 2)

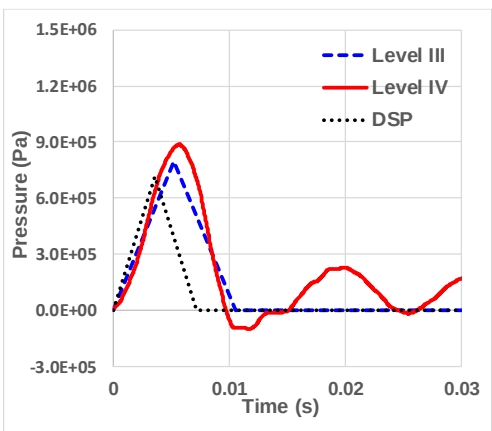

(a) Pressure

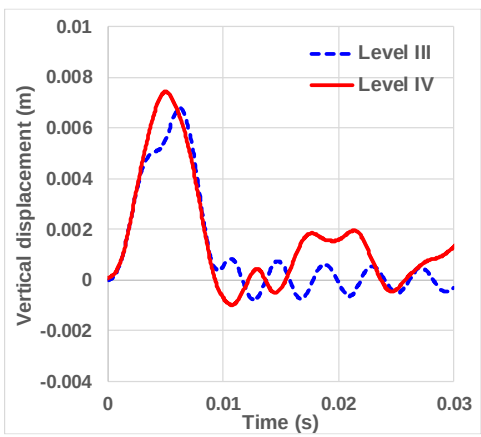

(b) Averaged displacement

Fig. 39. Results comparison (Case 3)

2.5. Conclusions

The hydroelasticity effect due to LNG CCS flexibility, which factor is not considered in sloshing tests, was investigated via fluid-structure interaction analysis. The fluid-structure interaction analysis was validated by wet drop test results. Then, a water hitting simulation was devised in order to realize the sloshing phenomenon

more precisely. A total of two structure models, namely a flat-rigid plate model and a flat-flexible CCS model, were generated to examine the hydroelasticity effect. The corrugation on the primary layer of the LNG CCS was neglected in the water hitting simulations. A comparison of the results for the two simulation models was performed for a total of 16 cases. It was confirmed that the hydroelasticity effect significantly influences sloshing load. In order to quantitatively reflect the hydroelasticity effect in actual design, a correction factor concept was introduced, and empirical formulas were proposed to predict the correction factor corresponding to an arbitrary sloshing load. When the correction factor was derived, effects such as air cushion, aeration and thermal exchange observed in real sloshing were not considered. Finally, an LNG CCS structural safety assessment procedure considering the hydroelasticity effect was established. The conclusions drawn from the present research are as follows.

- The fluid-structure interaction analysis was performed by using commercial software LS-dyna and verified by the wet drop test. Even though there is a limit to considering the precise characteristics of fluid, the peak value and duration time of the pressure profile showed good agreement with wet drop test results.
- Water hitting simulation is newly proposed to realize the sloshing phenomenon. In the present water hitting simulation, the structure model was fixed to the air domain, and fluid of specific velocity, dimensions and shape hit the structure.
- The existence of corrugation on the primary layer of the LNG

CCS induces complex fluid motion, so that was neglected in the water hitting simulation for simplicity.

- Two structure models, namely the flat-rigid plate model and the flat-flexible CCS model, were applied to the water hitting simulation for investigation of the hydroelasticity effect. These two models represent the sloshing model test condition and the real sloshing condition, respectively.

- A total of 16 types of water columns were generated to cover various hitting conditions. The velocity and deadrise angle were selected as variables for generation of the water columns.

- The change of pressure profile according to water column type was examined. The peak pressure decreased and rising time tended to increase as the deadrise angle of water column increased. On the other hand, the opposite tendency was observed in the case of the velocity of water column.

- The change of hydroelasticity effect according to water column type was investigated. The hydroelasticity effect was reduced as the deadrise angle of water column increased. The deadrise angle is a more dominant factor than velocity of water column for determination of the hydroelasticity effect.

- A total of three regions were adopted to calculate the pressure in the water hitting simulation. A relatively larger peak pressure was calculated for the 1 x 1 region, which is the smallest area and is located at the center of the impact region.

- For quantitative evaluation of hydroelasticity, the concept of the correction factor was suggested. The design sloshing pressure

measured in a sloshing model test can be modified by using the correction factor for consideration of the hydroelasticity effect. This leads to more sophisticated LNG CCS structural safety assessment.

- There are limitations in calculating correction factors by performing an FSI analysis on all design sloshing pressures. Therefore, an empirical formula was proposed to consider the hydroelasticity of the LNG CCS without any time-consuming FSI analysis, and accuracy verification was performed. A more general empirical formula can be obtained if the investigation of the effects of vertical flexibility on hydroelasticity is conducted in the future.

- Ultimately, on the basis of the water hitting simulation and correction factors, an LNG CCS structural safety assessment procedure considering the hydroelasticity effect was derived (and is proposed herein).

Chapter 3. Screening of Design Sloshing Pressure using Impulse Superposition Method

3.1. Introduction

The design sloshing pressure obtained from the sloshing model test is given for various rising times and loaded areas (see Table 7). In order to perform strength assessment of an LNG CCS, finite element analysis is required for all given design sloshing pressures. Such analysis consumes a lot of computation time. In particular, iterative FSI analysis is needed to conduct strength assessment of an LNG CCS in consideration of the hydroelasticity effect, as discussed in Chapter 2. It is not efficient to derive all water column properties corresponding to design sloshing pressures.

Table 7. Design sloshing pressures

	Loaded Area1	Loaded Area2	Loaded Area3
T_{r1}	$(T_{r1}, P1_{max1})$	$(T_{r1}, P2_{max1})$	$(T_{r1}, P3_{max1})$
⋮	⋮	⋮	⋮
T_{ri}	$(T_{ri}, P1_{maxi})$	$(T_{ri}, P2_{maxi})$	$(T_{ri}, P3_{maxi})$

As an alternative to finite element analysis, a simplified approach based on the impulse superposition method (see Fig. 40) has been suggested (ABS [10], Nho et al [40], Nho et al [42]). From the superposition of the structural response generated by a triangular impulse (unit load), the structural response to an arbitrary load can

be deduced without finite element analysis.

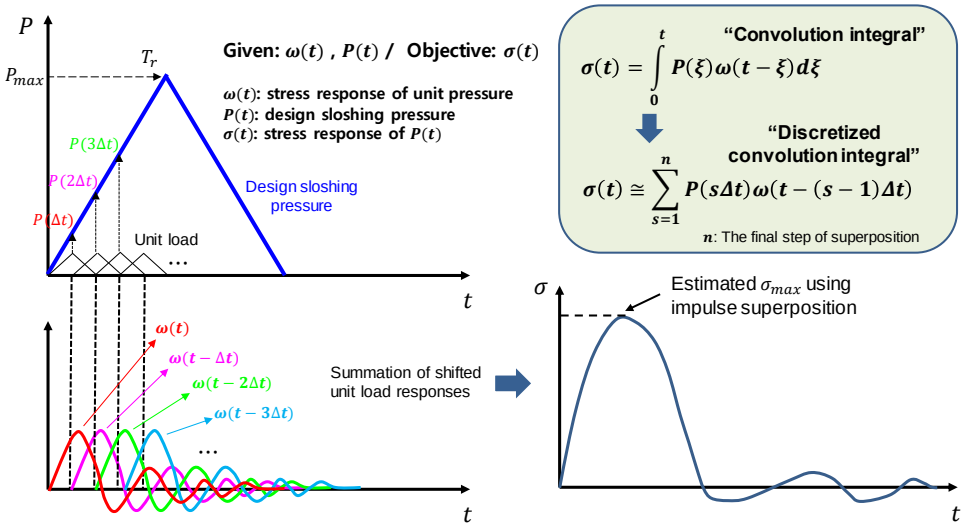

Fig. 40. Impulse superposition method

In the present study, a screening process for design sloshing pressures was conducted using the impulse/space superposition method (Thomson and Dahleh [43]). The most critical design sloshing pressure for failure modes that occur mainly in the LNG CCS can be chosen. Strength assessment of an LNG CCS can be efficiently achieved by performing FSI analysis only for the critical design sloshing pressures. The screening process for design sloshing pressures is as follows.

1. Calculate the stress response at the hot spot for the triangular impulse, which is used to represent the unit load.
2. Calculate the hot spot stress response of design sloshing pressures using the impulse superposition method.
3. Select the critical design sloshing pressures that generate the

largest stress response among the design sloshing pressures.

Critical design sloshing pressure is determined for each loaded area and failure mode. In this study, four design sloshing pressures were artificially generated based on the results of a sloshing model test. The screening process was then applied to the generated sloshing pressures.

3.2. Description of Finite Element Model

The finite element method was used to calculated the structural response of the LNG CCS. The LNG CCS structure model generated to perform the finite element analysis is shown in Fig. 41. The region where the girder and web section intersect in the upper corner of the LNG tank was selected as the modeling range. The model breadth was adopted as two spacing of stiffener. The inner hull deck, girder, web section, stiffener web and stiffener flange constituting the supporting structure were all modeled with shell elements. Solid elements were used for Mastic, Plywood and PUF constituting the insulation panel, and the element size was selected based on the value recommended by the classifications (DNVGL [12], Lloyd's [13]). The membrane to which the sloshing pressure is applied was modeled as shell elements. The effect of corrugation was indirectly taken into account by correcting the thickness so as to have an equivalent section modulus. Mastic and the inner hull deck were connected so that the shell element size of the supporting structure was equal to the mesh size of the insulation panel. The effect of the

slit on the insulation panel of the LNG CCS was neglected.

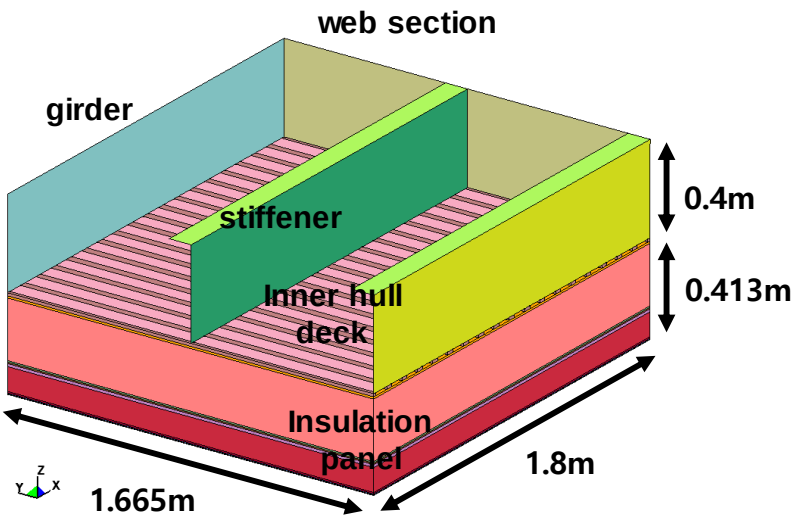

Fig. 41. LNG CCS FE model

The boundary conditions applied to the LNG CCS FE model are shown in Fig. 42. The translational fixed condition was exerted to the upper part of the girder and web section. Symmetric boundary conditions were adopted for each direction of the insulation panel and supporting structure.

A linear system was assumed when assessing the strength of an LNG CCS under design sloshing pressures. By wet drop test (introduced in Chapter2), it was confirmed that no significant plastic deformation of the membrane or supporting structure occurred. Therefore, a linear elastic material property was applied to the girder, web section, stiffener, inner hull deck and membrane. The 3D orthotropic elastic model was applied for PUF and Plywood. The mastic was represented as a 3D isotropic elastic model.

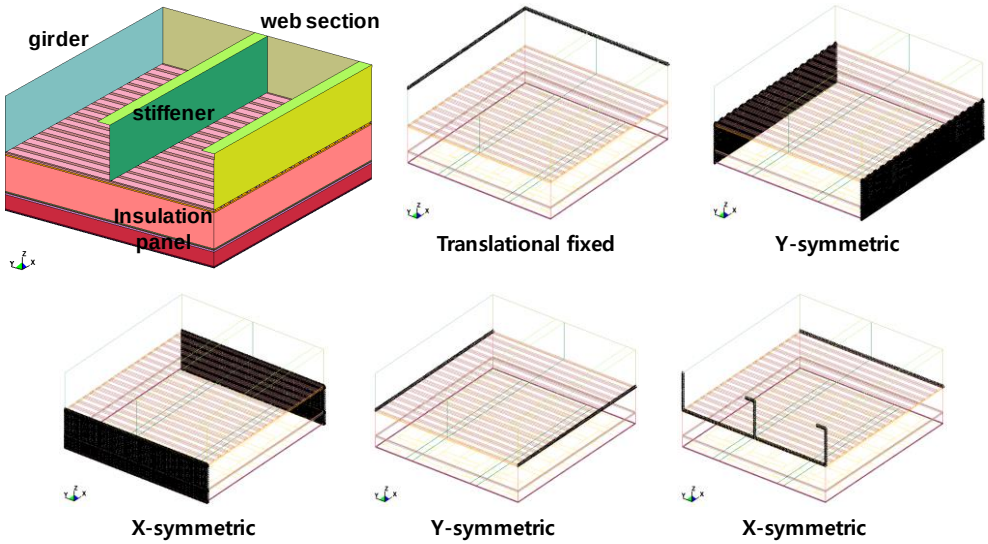

Fig. 42. Boundary conditions of LNG CCS FE model

3.3. Application of Screening Procedure

3.3.1. Generation of design sloshing pressures

The design sloshing pressures generally are obtained for three areas (0.33m x 0.33m, 0.67m x0.67m, 1.00m x1.00m). The rising time has a value between 1ms and 10ms. Based on the actual design sloshing pressures, the following four artificial design sloshing pressures were generated (see Fig. 43). To observe the hydroelasticity effect, correction factors were applied to the generated design sloshing pressures. The corrected design sloshing pressures considering the hydroelasticity effect were calculated (see Fig. 43). The correction factor was determined from an FSI analysis for the given LNG CCS model. The screening process also was performed for the corrected design sloshing pressures.

Loaded Area [m x m]	0.33 x 0.33
Rise time (ms)	Pressure (bar)
1	15
2	14.6
3	8
4	7.5

Design sloshing pressure(DSP)

Consideration of the hydrolasticity effect using correction factors
$C_{R-P} = f(P_d, T_r)$
$C_{R-T} = g(P_d, T_r)$

Loaded Area [m x m]	0.33 x 0.33
Rise time (ms)	Pressure (bar)
3.63	6.3
4.33	13.6
4.58	7.7
4.90	4.6

Corrected design sloshing pressure(CDSP)

Fig. 43. Generated design sloshing pressures

3.3.2. Calculation of unit load response

In general, the design sloshing pressure has a rising time of 1ms or more and a peak pressure of 1 bar or more. The rising time of unit load (unit pressure) should be shorter than 1ms in order to predict the response of design sloshing pressure using the impulse superposition method. As shown in Fig. 44, the peak value of unit load was 1bar, and the rising time was 0.5ms.

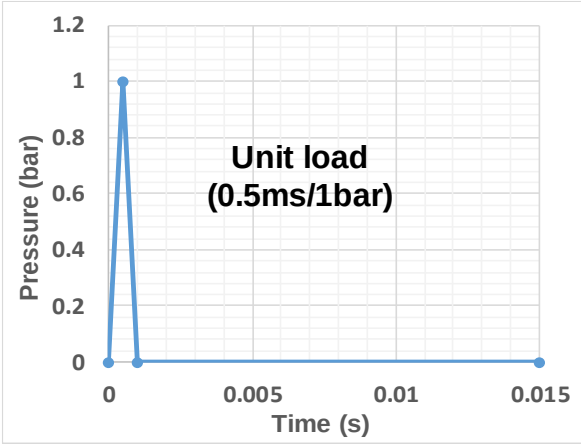

Fig 44. Selected unit load(pressure)

Each loaded area and corresponding hot spot location are shown in Fig. 45. Relatively high compression occurs where the girder and inner hull meet, and large stress is generated in Mastic, Plywood and PUF. Thus, as shown in Fig. 46, the design sloshing pressure is screened by targeting the stress observed from Mastic, Plywood and PUF located under the girder.

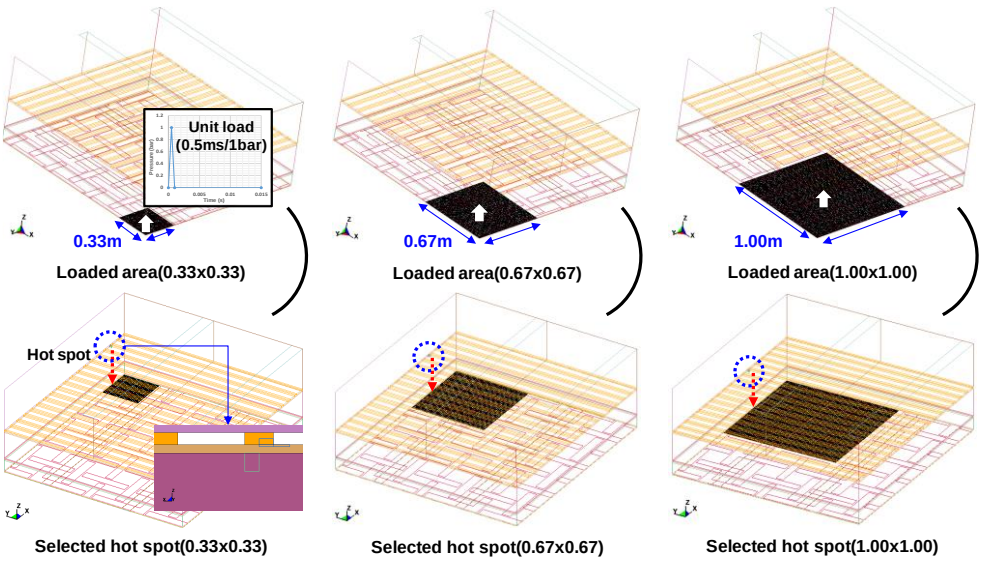

Fig. 45. Loaded area and location of hot spot

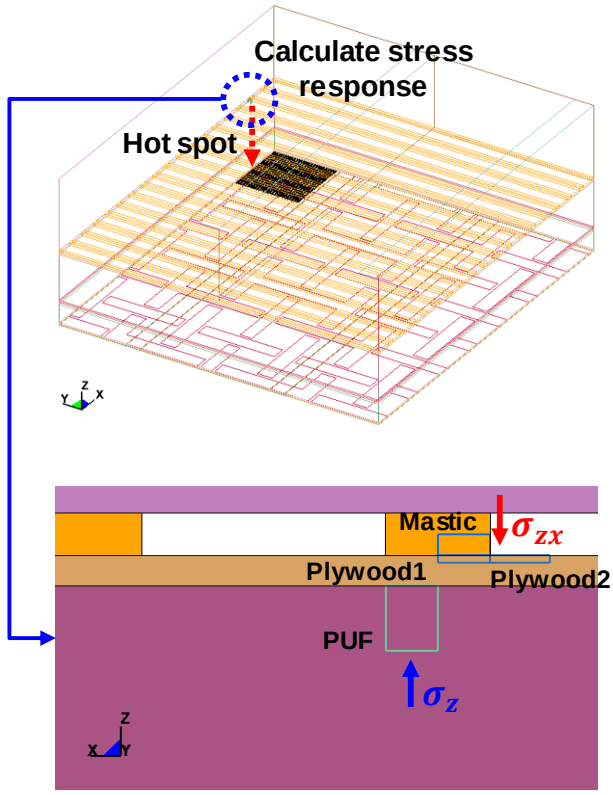

Fig. 46. Calculated stress response at hot spot

Among the LNG CCS failure modes caused by sloshing pressure (DNVGL [12], Park et al [44]), two modes were selected: vertical crushing($\boldsymbol{\sigma_z}$) and shear failure($\boldsymbol{\sigma_{zx}}$) induced by compression. Since shear failure rarely appears in PUF, a total of 7 stress responses were calculated as follows.

- PUF: vertical crushing($\boldsymbol{\sigma_z}$)
- Mastic: vertical crushing($\boldsymbol{\sigma_z}$), shear failure($\boldsymbol{\sigma_{zx}}$)
- Plywood1: vertical crushing($\boldsymbol{\sigma_z}$), shear failure($\boldsymbol{\sigma_{zx}}$)
- Plywood2: vertical crushing($\boldsymbol{\sigma_z}$), shear failure($\boldsymbol{\sigma_{zx}}$)

The generated design sloshing pressures had a loaded area of 0.33m x 0.33m. Seven hot spot stress responses were obtained by

applying the unit load to the loaded area of 0.33m x 0.33m as shown in Fig. 45. The results corresponding to the unit load response in the impulse superposition method are shown in Figs. 47 and 48. A relatively high vertical stress was observed in mastic, because the vertical elastic modulus of mastic is the largest. Looking at the shear stress results, a higher stress response was found in plywood2 than in plywood1 connected to mastic.

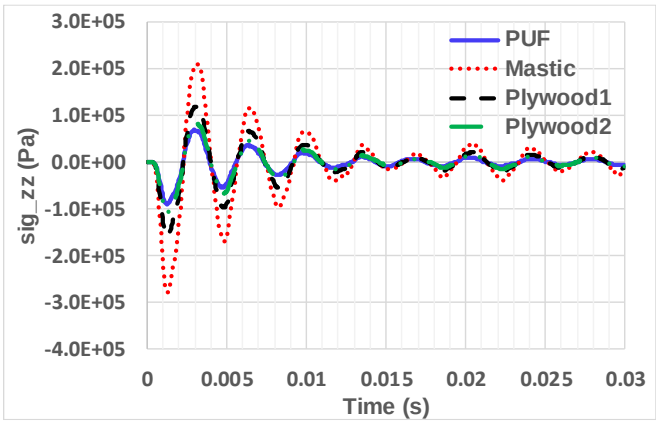

Fig. 47. Unit load responses (vertical crushing)

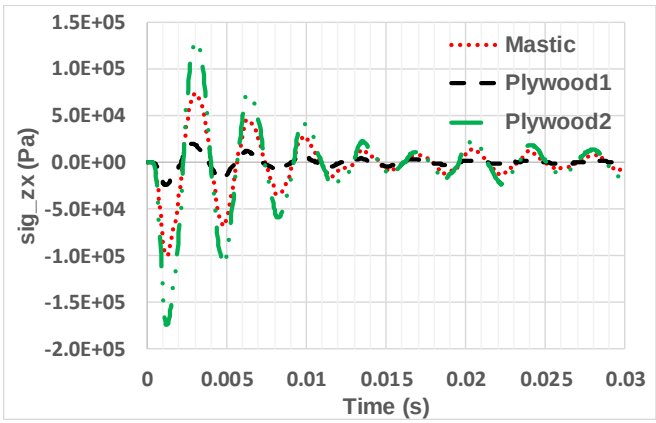

Fig. 48. Unit load responses (shear failure)

3.3.3. Selection of critical design sloshing pressure

Based on the calculated unit load responses, the impulse superposition method can be applied to estimate the hot spot stress response for any design sloshing pressure. In order to confirm the validity of the impulse superposition method, its predicted results were compared with those of transient analysis. In the transient analysis, seven hot spot stress responses were extracted by directly applying the selected design sloshing pressures to the loaded area. Fig. 49 shows a comparison of results for vertical crushing (σ_z) generated in PUF. For all of the design sloshing pressures, it can be seen that not only the first peak but also the response by vibration were predicted accurately.

Fig. 50 compares the results obtained through the transient analysis and the impulse superposition method. Seven hot spot stress responses were calculated from each of the four design sloshing pressures. From this, it could be judged that the prediction of hot spot stress response using the impulse superposition method was reasonable.

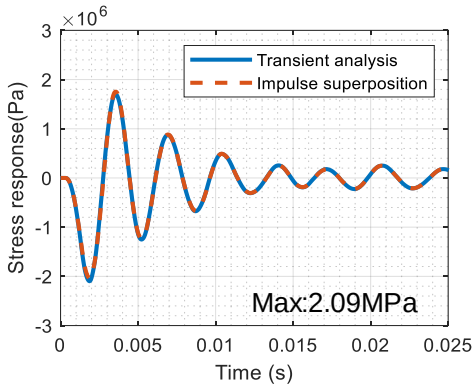

(1ms, 15bar)

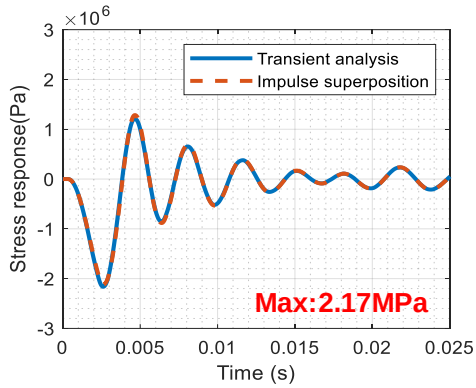

(2ms, 14.6bar)

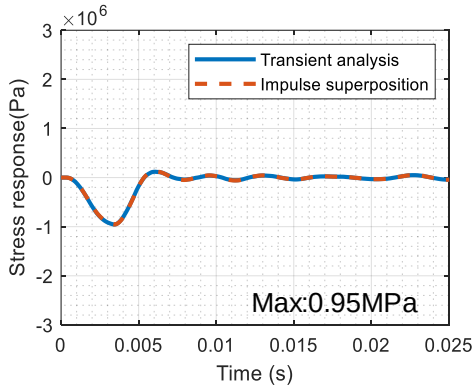

(3ms, 8bar)

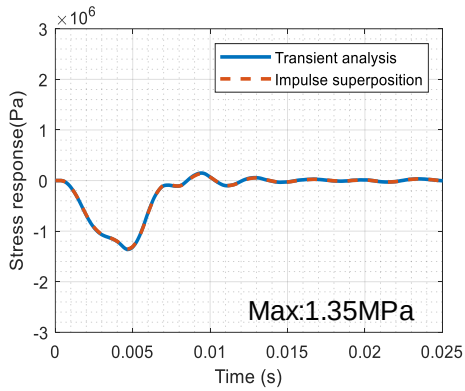

(4ms, 7.5bar)

Fig. 49. Calculated time history of stress response

The impulse superposition method results and transient analysis results agreed well enough for the corrected design sloshing pressures. However, looking at the generated stress level, a small stress response relative to the design sloshing pressure results was observed. As was confirmed in Chapter 2, this means that the severity of the structural response of the LNG CCS is reduced when the hydroelasticity effect in the design sloshing pressure is considered.

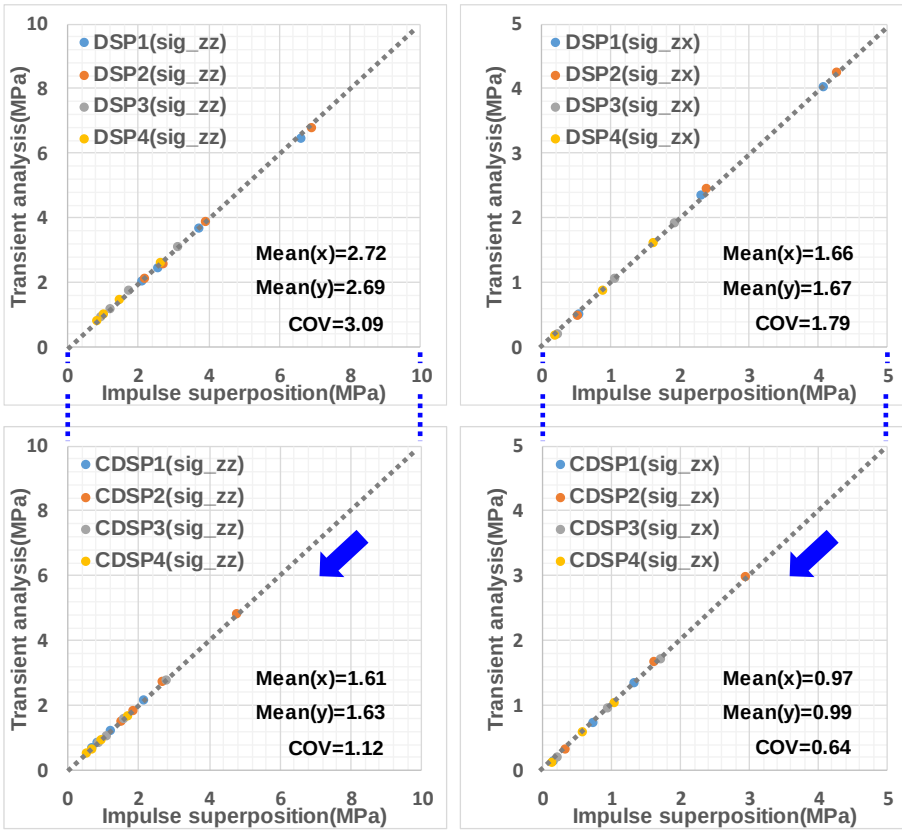

Fig. 50. Comparison of peak stress

Using the unit load responses (see Figs. 47 and 48), hot spot stress response prediction was performed for the selected design sloshing pressures without additional finite element analysis. The predicted vertical crushing responses for PUF, mastic and plywood are illustrated in Fig. 51. From the calculated results, it can be determined that when conducting strength assessment for vertical crushing of insulation panel, design sloshing pressure no. 2 is the most critical. In the case of shear failure, the highest stress response was obtained also at design sloshing pressure no.2 (see Fig. 52). Therefore, design sloshing pressure no.2 was determined to be the most critical pressure for all failure modes.

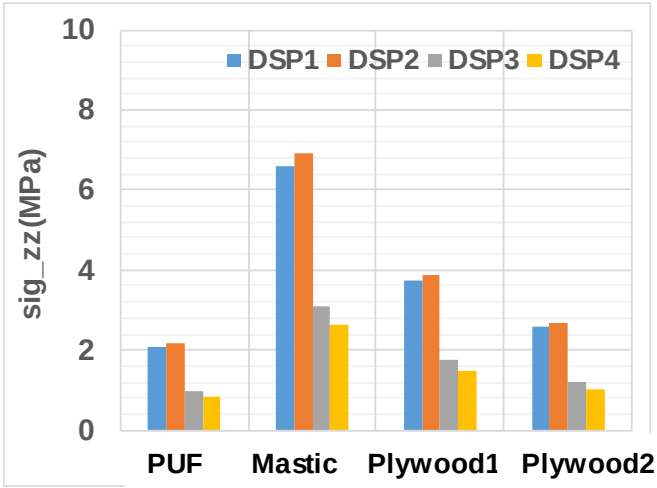

Fig. 51. Predicted hot spot stress responses for design sloshing pressures (vertical crushing)

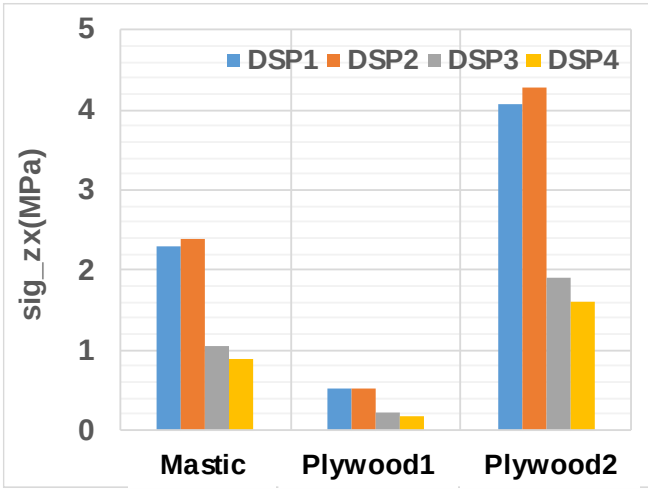

Fig. 52. Predicted hot spot stress responses for design sloshing pressures (shear failure)

Similarly, the hot spot stress responses were predicted using the impulse superposition method for the corrected design sloshing pressures (see Figs. 53 and 54). The stress response level was relatively small due to the hydroelasticity effect. And, as was the

case for the design sloshing pressure, pressure no.2 was determined to be the most critical, even for the corrected design sloshing pressure. Table 8 shows the selected critical design sloshing pressure results. By performing detailed LNG CCS strength assessment only for the selected critical design sloshing pressure, the design efficiency was increased. In particular, the burden of analysis was greatly reduced when FSI analysis was adopted to take into account the hydroelasticity effect.

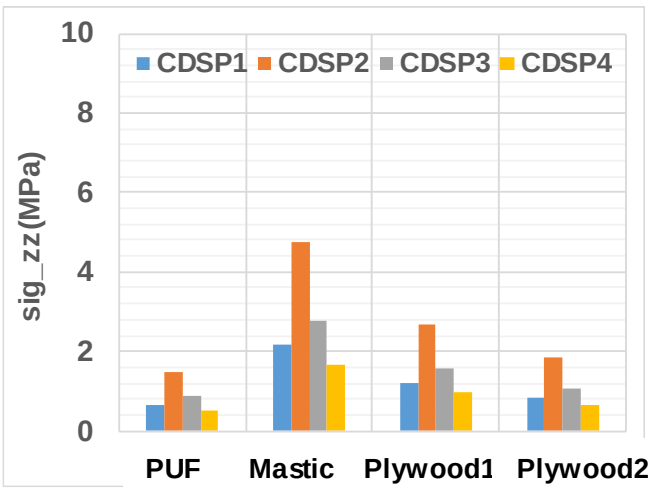

Fig. 53. Predicted hot spot stress responses for corrected design sloshing pressures (vertical crushing)

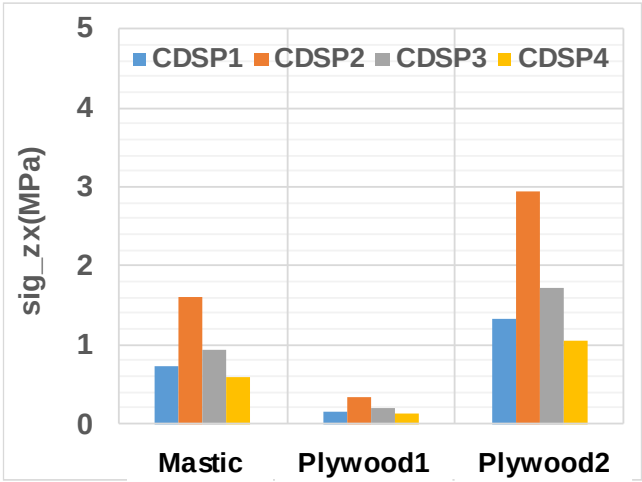

Fig. 54. Predicted hot spot stress responses for corrected design sloshing pressures (shear failure)

Table 8. Selected critical design sloshing pressures

Loaded Area (0.33x0.33)	(T_r, P_{max})	Loaded Area (0.33x0.33)	(T_r, P_{max})
DSP1	(1ms, 15bar)	CDSP1	(3.63ms, 6.3bar)
DSP2	(2ms, 14.6bar)	CDSP2	(4.33ms, 13.6bar)
DSP3	(3ms, 8bar)	CDSP3	(4.58ms, 7.7bar)
DSP4	(4ms, 7.5bar)	CDSP4	(4.90ms, 4.6bar)

The peak value of pressure no.1 was larger than pressure no.2 (selected as the critical design sloshing pressure). The stress response generated in the LNG CCS was affected not only by the peak value of pressure but also by the rising time. Modal analysis was performed to calculate the natural frequency of the LNG CCS

model, and the results are presented in Table 9. Looking at the natural frequency of the LNG CCS model, the contribution of mode3 was dominant, as shown in Fig. 55. The rising time of pressure corresponding to the frequency of mode3 was about 2 to 3ms. Due to the effect of rising time, although the peak pressure of design sloshing pressure no.1 was slightly higher than that of design sloshing pressure no.2, design sloshing pressure no.2 was classified as a more critical pressure in terms of stress response. Design sloshing pressure no.3 had a much lower peak pressure than design sloshing pressures no.1 and no.2. Thus, design sloshing pressure no.3 was relatively insignificant even when taking the rising time effect into account.

Table 9. Natural frequency of LNG CCS model

	Participation (%)	Frequency (Hz)	Period (ms)	Rising time (ms)
1st mode	9.8	61	16.39	4.10
2nd mode	4.8	64	15.63	3.91
3rd mode(*)	**44.9**	**99**	**10.10**	**2.53**
4th mode	9.0	114	8.77	2.19
5th mode	0.4	140	7.14	1.79

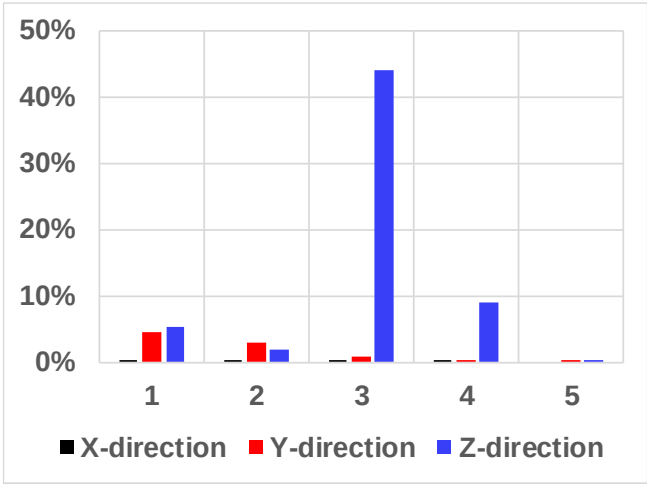

Fig. 55. Modal effective mass fraction of LNG CCS model

3.4. Conclusions

The screening process for design sloshing pressures was conducted using the impulse superposition method. If FSI analysis was performed only for the selected critical design sloshing pressure, the design efficiency increased. The conclusions drawn from the present research are as follows.

- The impulse superposition method can be used to predict the structural response of an LNG CCS for given design sloshing pressures. Structural response is influenced not only by peak pressure but also by rising time.
- From the predicted structural response, the critical design sloshing pressure can be selected for each failure mode. By applying the critical design sloshing pressure to FSI analysis, strength assessment of an LNG CCS in consideration of the hydroelasticity effect can be effectively performed.

Chapter 4. Prediction of Sloshing Pressure and LNG CCS Structural Response

4.1. Introduction

Several studies have been conducted to obtain sloshing pressures generated on the inner wall of LNG tanks. The most widely used method is the sloshing model test (Kim et al [45], Kim et al [46], Kwon et al [47], Kim et al [48], Ahn et al [49], Bureau Veritas [50], Loysel et al [51]). In the sloshing model test, the pressure generated by 6-DOF ship motion is measured by attaching pressure sensors to an LNG tank model. By applying an appropriate scaling law (ITTC [52], Karimi et al [53], Karimi et al [54], Bogaert et al [55]) to the measured pressure time history, the real sloshing pressure time history can be estimated. After that, the design sloshing pressures are finally calculated through a statistical process. Recently, in order to more accurately observe the sloshing phenomenon and predict sloshing pressures, sloshing model tests have been performed on large and/or real scales (Bogaert et al [55], Bunnik and Huijsmans [56], Bogaert et al [57]).

With the gradual development of computational technology, sloshing pressure calculation using computational fluid dynamics (CFD) has also been actively studied (Parthasarathty et al [58], Xie et al [59], Zhuang and Wan [60], Ge et al [61], Hwang and Lee [62], Brizzolara et al [63]). Various verifications are being made by comparing the sloshing pressure calculated from CFD and that obtained through a sloshing model test. In the approach using CFD,

the size of the LNG tank can be reflected as it is, which affords a cost-effective advantage compared to sloshing model testing. However, there remain limitations in calculating a sloshing pressure time history of several hours using CFD.

Research on the structural response of the LNG CCS to sloshing pressure has proceeded based on the finite element method (ABS [10], DNVGL [12], KR [64], Lloyd [65]). The most widely used methods apply the dynamic amplification factor (DAF) to static analysis and perform transient analysis by reflecting both the peak and rising time of design sloshing pressure (Chun et al [66], Pillon et al [67], Arswendy et al [68], Hwang et al [69]). In addition, to consider the effect of fluid, a method of introducing a dashpot system or directly modeling the LNG domain and then performing FSI analysis has been proposed (Jin et al [14], Wang and Shin [70], Lee et al [71]). Simplified methods to calculate the structural response of an LNG CCS using a triangular response function instead of finite element analysis (ABS [10], Nho et al [40], Nho et al [42]) also have been suggested. These simplified methods are based on the impulse superposition method.

Even though research on sloshing has been carried out by various approaches, there is still insufficient information on the time history of sloshing pressure or the time history of the stress response generated in the insulation panel. It is difficult to predict the sloshing pressure in real time from the sloshing model test. There is also a limit to estimating the structural response of an LNG CCS for given design sloshing pressures in real time from strength assessment

results.

There are many practical limitations to measuring sloshing pressure and structural response by directly placing sensors inside the membrane or insulation panel. Alternatively, it is possible to measure the response of the supporting structure of an LNG CCS. In the present study, then, a method for predicting the sloshing pressure and structural response of an insulation panel from measured stress data on the LNG CCS supporting structure is proposed. When real-time sloshing pressure is predicted from the measured stress data, the peak level and rising time range for sloshing pressure generated in the actual LNG tank can be identified. In this way, the validity of the design sloshing pressures currently applied to LNG CCS strength assessment can be judged.

Structural integrity monitoring of the LNG CCS from the predicted real-time stress response has become possible. In addition to monitoring of the occurrence of instant failure beyond the allowable stress, prediction of fatigue damage accumulated over time also can be carried out.

The impulse/space superposition method is used to predict sloshing pressure from measured stress data on the supporting structure. From the predicted sloshing pressure and hot spot stress response of unit pressure, the hot spot stress response to sloshing pressure is calculated. Additionally, a method for estimating the hot spot stress response to sloshing pressures through the mode superposition method is suggested. Figure 56 shows the overall procedure for prediction of the sloshing pressure and hot spot stress

response of an LNG CCS. The stress response of unit pressure is calculated through transient analysis. The modal amplitude can be obtained from the measured stress response data on the supporting structure and the modal analysis result for an LNG CCS model.

Given the measured stress response of the supporting structure, the sloshing pressure can be predicted by applying the impulse/space superposition method (see Fig. 56). And as for the hot spot stress response of an LNG CCS, it can be estimated using either the impulse/space superposition method or the mode superposition method (see Fig. 56).

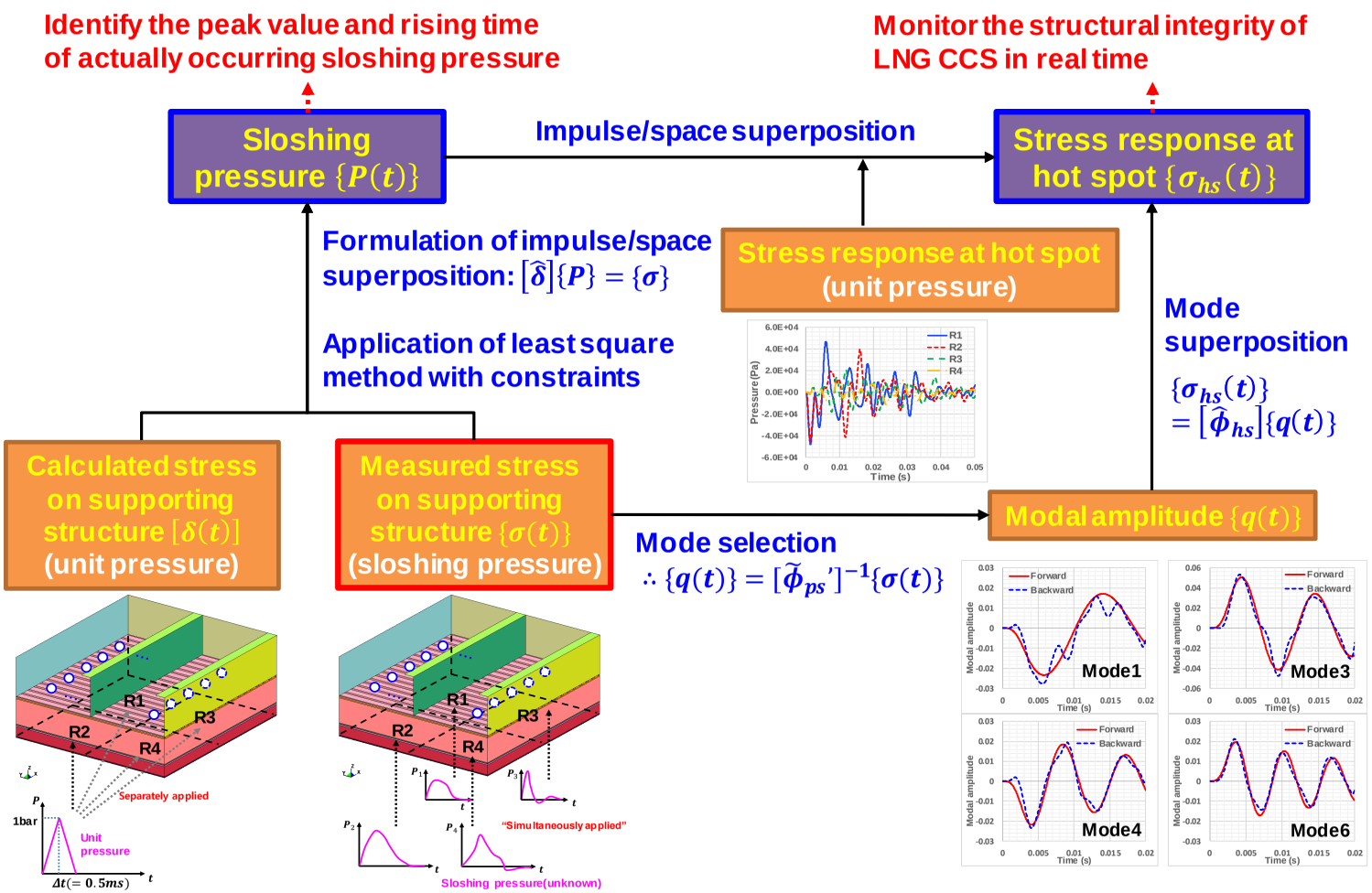

Fig. 56. Overall procedure for sloshing pressure and hot spot stress response prediction

4.2. Prediction of Sloshing Pressure and LNG CCS Structure Response using Impulse/Space Superposition Method

The sloshing pressure, which is generated on membrane of LNG CCS, is applied to multiple areas simultaneously. The concept of space superposition is added to the existing impulse superposition method in order to consider the effect of several sloshing pressure application areas. The relationship between the measured stress response and the unit pressure stress response is established through the impulse/space superposition method. This relationship is expressed by the sloshing pressure applied to each area. Thus, given the measured stress response and unit pressure stress response, the corresponding sloshing pressure can be calculated. By applying the impulse/space superposition method to the calculated sloshing pressure, hot spot stress responses for sloshing pressure are obtained. The measured stress response of the supporting structure is converted to time histories of sloshing pressure and hot spot stress responses.

4.2.1. Impulse/space superposition method

The response to an arbitrary load can be expressed as the superposition of the unit load response, which approach is known as the impulse superposition method. Fig. 57 illustrates the concept of this method. At a specific time $t = \xi$, the impulse of applied load $P(\xi)$is $P(\xi)\Delta\xi$. The response generated by impulse $P(\xi)\Delta\xi$ can be

expressed as $P(\xi)\Delta\xi\delta(t-\xi)$, where $\delta(t)$ is the unit load response. In general, a delta function or an idealized triangular impulse is utilized as the unit load. If only the result of the unit load response is given, the response to an arbitrary load is calculated by means of the convolution integral of the unit load response (see Eq. 10).

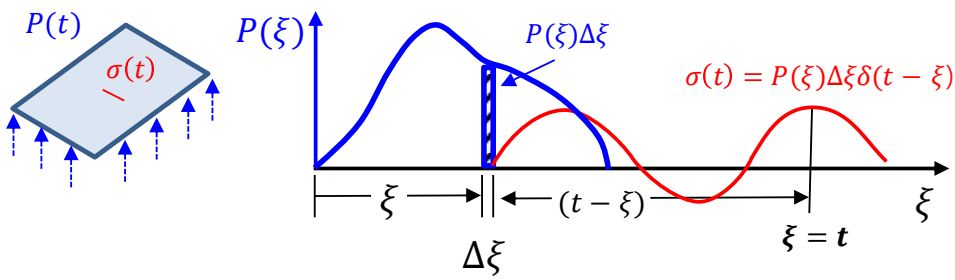

Fig. 57. Impulse superposition method

$$\sigma(t) = \int_0^t P(\xi)\delta(t-\xi)\,d\xi \cdots (10)$$

where,

$\sigma(t)$: *actual response*

$\delta(t)$: *unit load response*

$P(t)$: *applied load*

The sloshing phenomenon generates different pressures on each selected area. In the sloshing model test, sloshing pressures are measured in several areas. A different sloshing pressure is obtained for each measurement area. In order to consider the effect of area, the concept of space superposition is additionally introduced to the impulse superposition method. Thus, this combined approach is

named the impulse/space superposition method. Figure 58 illustrates an example of the application of the impulse/space superposition method to a case where there are four regions to which sloshing pressure is applied. The response at a specific location is affected by $P_1(t) \sim P_4(t)$, respectively. The contribution of $P_1(t)$ can be written as in Eq. 11. The contribution of $P_2(t) \sim P_4(t)$ can be treated in the same way.

$$\int_0^t P_1(\xi)\, \delta^1\,(t - \xi)\, d\xi \cdots (11)$$

By linearly integrating all of the effects of the four loads, response $\sigma(t)$ at a specific location is expressed as in Eq. 12.

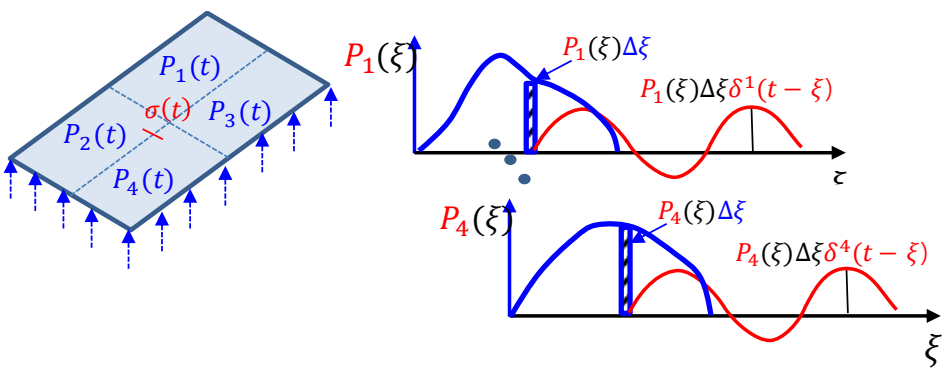

Fig. 58. Impulse/space superposition method

$$\sigma(t) = \sum_{k=1}^{4} \int_0^t P_k(\xi)\, \delta^k\,(t - \xi)\, d\xi \cdots (12)$$

where,

$\sigma(t)$: *actual response*

$P_k(t)$: *applied load on the* k^{th} *region*

$\delta^k(t)$: *response when unit load is applied to* k^{th} *region*

The response of multiple points can be calculated using the impulse/space superposition method. Figure 59 shows an example of impulse/space superposition method application wherein there are three points at which to predict the response. Given a unit load response at each measurement point, the impulse/space superposition method can be applied independently. Response $\sigma_1(t)$ at the first position is calculated from unit load response $\delta_1^k(t)$. Superscript k represents the number of regions in which the load is applied. Similarly, $\sigma_2(t)$ and $\sigma_3(t)$ are calculated using $\delta_2^k(t)$ and $\delta_3^k(t)$, respectively. When the load is applied to several regions simultaneously, a response at an arbitrary location can be obtained using Eq. 13.

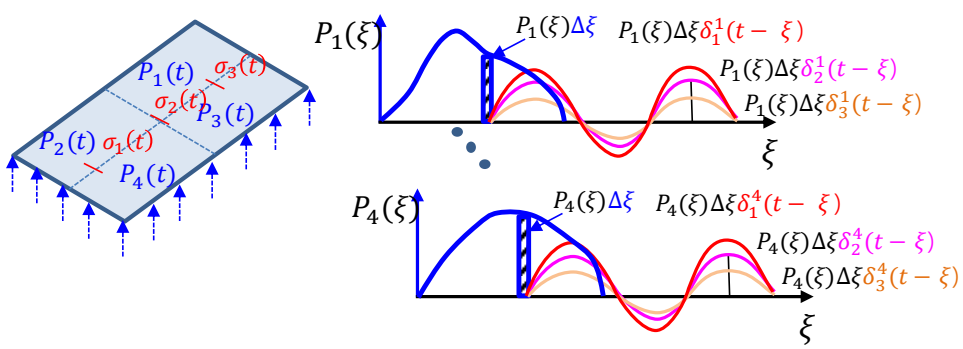

Fig. 59. Impulse/space superposition for multiple responses

$$\sigma_i(t) = \sum_{k=1}^{4} \int_0^t P_k(\xi)\delta_i^k(t - \xi)\, d\xi \cdots (13)$$

where,

$\sigma_i(t)$: $actual\ response\ at\ the\ i^{th}\ location$

$P_k(t)$: $applied\ load\ on\ the\ k^{th}\ region$

$\delta_i^k(t)$: $response\ at\ the\ i^{th}\ location\ where\ unit\ load\ is\ applied\ to\ k^{th}\ region$

4.2.2. Prediction of sloshing pressure

The LNG CCS model used to predict the sloshing pressure and stress response is shown in Fig. 60. It is identical to the model introduced in Chapter 3: the boundary conditions and material properties are all the same. Based on the area where the sloshing pressure is measured in the sloshing model test, the membrane is divided into four regions, and sloshing pressure prediction is performed for the selected regions. The in-plane stress generated on the inner hull deck was chosen as the measurement data. Among the in-plane stresses in the x- and y-directions, the y-direction in-plane stress corresponding to the longitudinal direction of mastic was used to predict sloshing pressure. The longitudinal direction of mastic is the transverse direction of the vessel; as such, the influence of the hull girder moment rarely appears. Stress was measured at a total of 25 locations, and the sensor placement distance was determined to be three times the mastic spacing. It was confirmed that the uncertainty of measured stress increases when sensors are placed at the position where the stiffener passes. Placing additional

sensors on the stiffener web has no significant effect. Figure 61 shows the sloshing pressure prediction regions and stress measurement points.

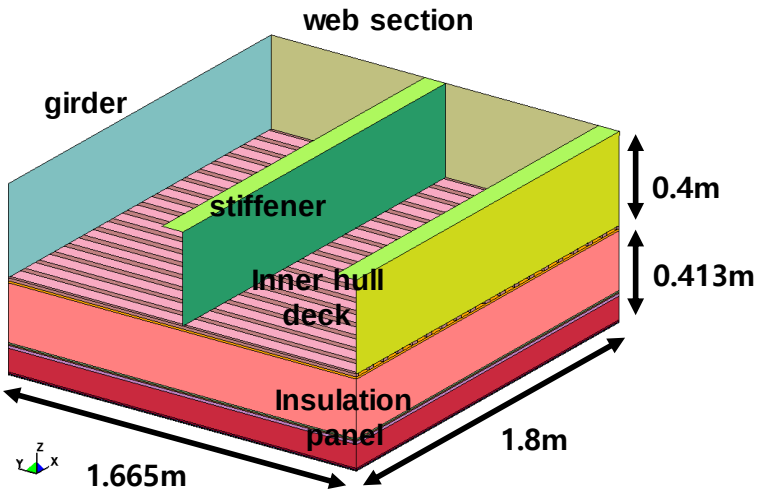

Fig. 60. LNG CCS model

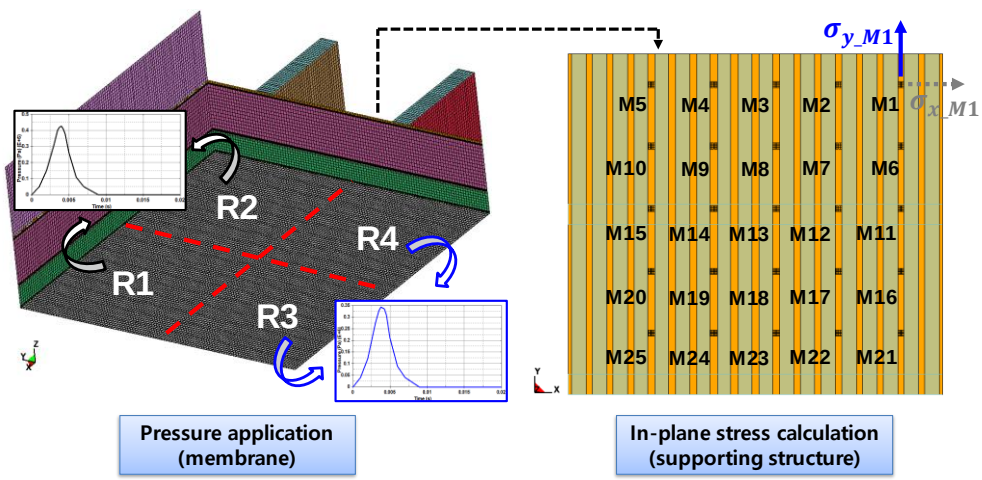

Fig. 61. Sloshing pressure prediction regions and stress measurement locations

4.2.2.1. Stress response of unit pressure

The response at each measurement point by unit pressure was calculated for the LNG CCS model. The unit pressure was assumed to be a triangular impulse having no skewness. The peak value of unit pressure was 1 bar, and the rising time was 0.5ms.

The calculated unit pressure stress responses at the measurement points are illustrated in Fig. 62. The four regions for sloshing pressure prediction are named R1, R2, R3 and R4, respectively. When unit pressure was applied to R1, the stress responses obtained at the 25 measurement points were represented as $\delta_1^1(t)$~$\delta_{25}^1(t)$. Similarly, when unit pressure was applied to R2~R4, the stress responses obtained at the 25 measurement points can be written as $\delta_1^2(t)$~$\delta_{25}^2(t)$, $\delta_1^3(t)$~$\delta_{25}^3(t)$ and $\delta_1^4(t)$~$\delta_{25}^4(t)$, respectively.

Finally, the measurement points' stress response to the unit pressure was expressed as in Eq. (14). At a specific time t, the unit pressure stress response had a matrix of 25 by 4. This unit pressure stress response was obtained directly by performing transient analysis on the LNG CCS model. The unit pressure stress response $[\delta(t)]$ is given value when predicting the sloshing pressure using the impulse/space superposition method.

$$[\delta(t)] = \begin{bmatrix} \delta_1^1(t) & \cdots & \delta_1^4(t) \\ \vdots & \ddots & \vdots \\ \delta_{25}^1(t) & \cdots & \delta_{25}^4(t) \end{bmatrix} \cdots (14)$$

where,

$\delta_i^k(t)$: *response at the* i^{th} *location where unit pressure is applied to* k^{th} *region*

4.2.2.2. Stress response of sloshing pressure

Sloshing pressure with an arbitrary pressure profile acts on the four regions simultaneously. Figure 63 represents the measured stress response generated by the sloshing pressure. Unlike the unit pressure stress response, there is no k index corresponding to the region to which the pressure is applied. The stress response of sloshing pressure is written as Eq. (15).

$$\{\sigma(t)\} = \begin{Bmatrix} \sigma_1(t) \\ \sigma_2(t) \\ \vdots \\ \sigma_{25}(t) \end{Bmatrix} \cdots (15)$$

where,

$\sigma_i(t)$: $response\ of\ sloshing\ pressure\ at\ the\ i^{th}\ location$

The supporting structure's stress response generated by sloshing pressure can be measured from the sensors. $\{\sigma(t)\}$ is a known value like $[\delta(t)]$. From these two values, the sloshing pressure applied to R1~R4 can be predicted by impulse/space superposition.

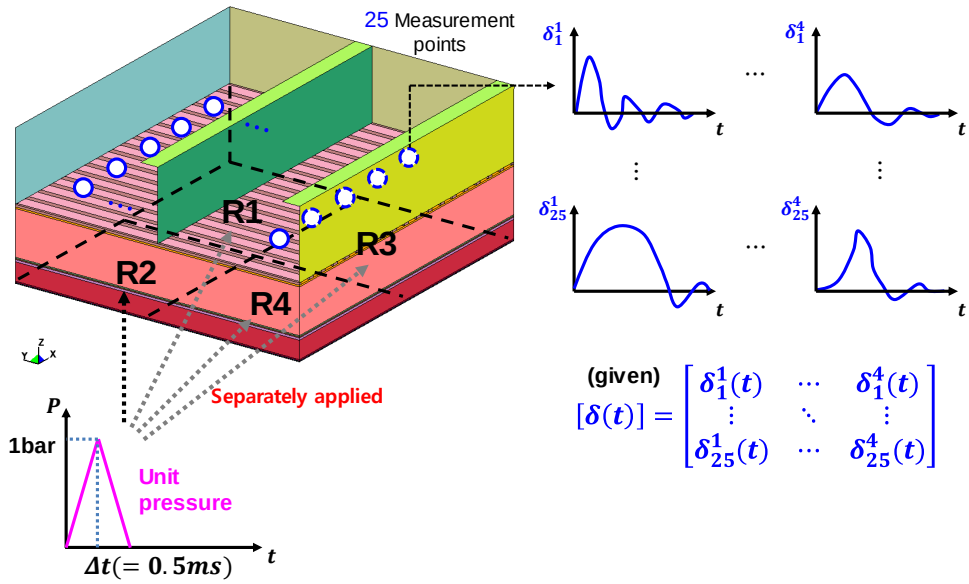

Fig. 62. Stress responses of unit pressure

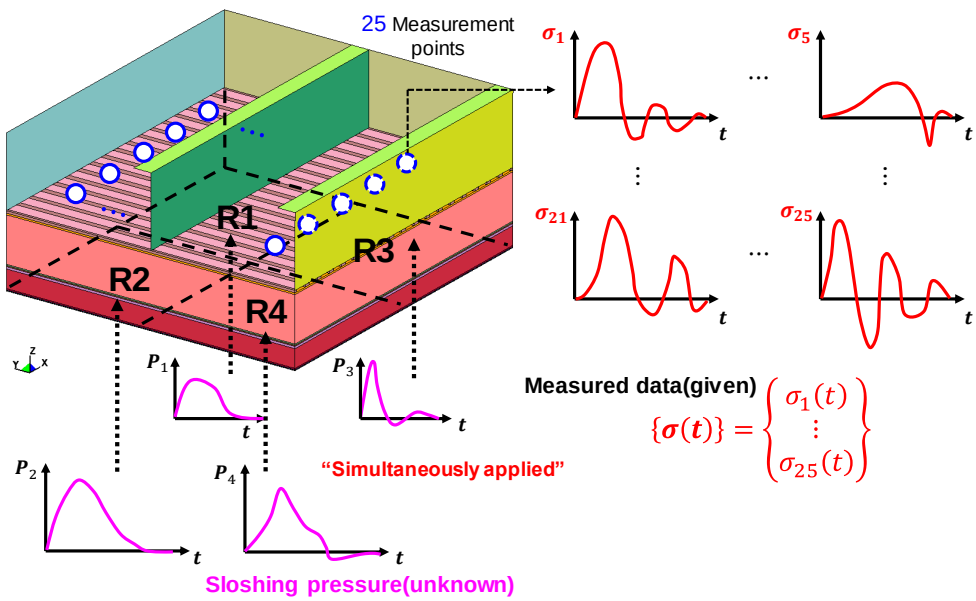

Fig. 63. Stress responses of sloshing pressure

4.2.2.3. Correlation between $[\delta(t)]$ and $\{\sigma(t)\}$

The relationship between the given stress responses and sloshing pressure can be expressed by Eq. (16). The time step by which the unit pressure stress response is superimposed is equal to the rising time of unit pressure, $\Delta t = 0.5ms$. When the sloshing pressure prediction range is $q\Delta t$, the superposition of unit pressure stress response is as shown in Fig. 64. The sloshing pressure P(t) is discretized at intervals of Δt. At each time step, the sloshing pressure amplitude is multiplied by the shifted unit pressure stress response. For instance, at $t = \Delta t$, $P(\Delta t)$ is multiplied by $\delta(t)$, and at $t = 2\Delta t$, $P(2\Delta t)$ is multiplied by a function in which $\delta(t)$ is shifted by Δt. A linear superposition of sloshing pressure amplitude and stress response of unit pressure is conducted up to the defined sloshing pressure prediction range $q\Delta t$. Then, the stress response due to the sloshing pressure is calculated.

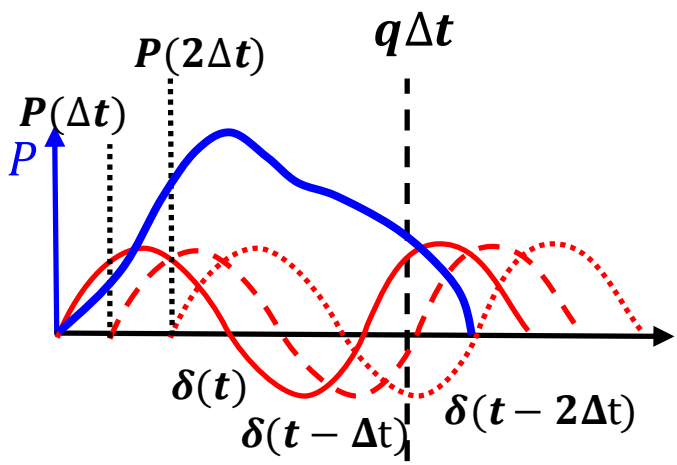

Fig. 64. Schematic of superposition of unit pressure response

The stress response of sloshing pressure discretized by intervals of Δt can be written as Eq. (16). Since the sloshing pressure is applied to a total of 4 regions, sloshing pressure $\{P(t)\}$ can be expressed as a 4 by 1 vector constituted of $P_1(t)\sim P_4(t)$.

$$\{\sigma(t)\}|_{t=\Delta t} = \sum_{s=1}^{1}[\delta(t-(s-1)\Delta t)]_{|_{t=\Delta t}} \cdot \{P(s\Delta t)\}$$

$$\{\sigma(t)\}|_{t=2\Delta t} = \sum_{s=1}^{2}[\delta(t-(s-1)\Delta t)]_{|_{t=2\Delta t}} \cdot \{P(s\Delta t)\}$$

$$\vdots$$

$$\{\sigma(t)\}|_{t=q\Delta t} = \sum_{s=1}^{q}[\delta(t-(s-1)\Delta t)]_{|_{t=q\Delta t}} \cdot \{P(s\Delta t)\} \cdots (16)$$

where,

$$\{\sigma(t)\} = \begin{Bmatrix} \sigma_1(t) \\ \sigma_2(t) \\ \vdots \\ \sigma_{25}(t) \end{Bmatrix} : \text{stress response of sloshing pressure}$$

$$[\delta(t)] = \begin{bmatrix} \delta_1^1(t) & \cdots & \delta_1^4(t) \\ \vdots & \ddots & \vdots \\ \delta_{25}^1(t) & \cdots & \delta_{25}^4(t) \end{bmatrix} : \text{stress response of unit pressure}$$

$$\{P(t)\} = \begin{Bmatrix} P_1(t) \\ \vdots \\ P_4(t) \end{Bmatrix} : \text{sloshing pressure}$$

When all of Eq. (16) is added, the left side becomes the stress response of sloshing pressure for each time step, and the right side, also for each time step, is expressed as the product of unit pressure stress response and sloshing pressure amplitude. This can be reduced to the one formula in Eq. (17). The variable $(s-1)\Delta t$

represents the shifted time of the unit pressure stress response. If s=2, the stress response of unit pressure is shifted by Δt.

$$\begin{Bmatrix} \sigma_1(t) \\ \vdots \\ \sigma_{25}(t) \end{Bmatrix}_{|_{t=\Delta t:\Delta t:q\Delta t}} = \begin{bmatrix} \delta_1^1(t-(s-1)\Delta t) & \cdots & \delta_{25}^k(t-(s-1)\Delta t) \\ \vdots & \ddots & \vdots \\ \delta_{25}^1(t-(s-1)\Delta t) & \cdots & \delta_{25}^4(t-(s-1)\Delta t) \end{bmatrix}_{\substack{|_{t=\Delta t:\Delta t:q\Delta t} \\ s=1:q}}$$

$$\cdot \begin{Bmatrix} P_1(t) \\ \vdots \\ P_4(t) \end{Bmatrix}_{|_{t=\Delta t:\Delta t:q\Delta t}} \cdots (17)$$

The peak value of the dynamic response by impulse appears at a time different from the rising time of impulse. This means that the time at which the peak of unit pressure stress response($\delta(t)$)occurs is different from the rising time of unit pressure, $\Delta t = 0.5ms$. Thus, if the stress response is discretized at Δt intervals, the peak value may be omitted. In this study, $\Delta t' = 0.05ms$ was adopted as the time step for calculating the LNG CCS stress response generated by unit pressure and sloshing pressure. The time step $\Delta t' = 0.05ms$ is sufficient not to miss the peak value of stress response.

Between $\Delta t = 0.5ms$, which is the discretization step of sloshing pressure, there are a total of 10 values of stress response. Figure 65 shows the relationship between the sloshing pressure discretization step $\Delta t = 0.5ms$ and the stress response discretization step $\Delta t' = 0.05ms$.

When the discretization step of $\Delta t' = 0.05ms$ is applied to the stress response, Eq. (17) is converted into Eq. (18). $\{P(t)\}$ does not change, and the values of $\{\sigma(t)\}$ and $[\delta(t)]$ are defined by time step $\Delta t'$. The

time step at which the pressure amplitude is predicted is maintained at Δt.

$$\begin{Bmatrix} \sigma_1(t) \\ \vdots \\ \sigma_{25}(t) \end{Bmatrix}_{|t=\Delta t:\Delta t':q\Delta t} = \begin{bmatrix} \delta_1^1(t-(s-1)\Delta t) & \cdots & \delta_{25}^k(t-(s-1)\Delta t) \\ \vdots & \ddots & \vdots \\ \delta_{25}^1(t-(s-1)\Delta t) & \cdots & \delta_{25}^4(t-(s-1)\Delta t) \end{bmatrix}_{\substack{|t=\Delta t:\Delta t':q\Delta t \\ s=1:q}} \cdot \begin{Bmatrix} P_1(t) \\ \vdots \\ P_4(t) \end{Bmatrix}_{|t=\Delta t:\Delta t:q\Delta t} \quad \cdots (18)$$

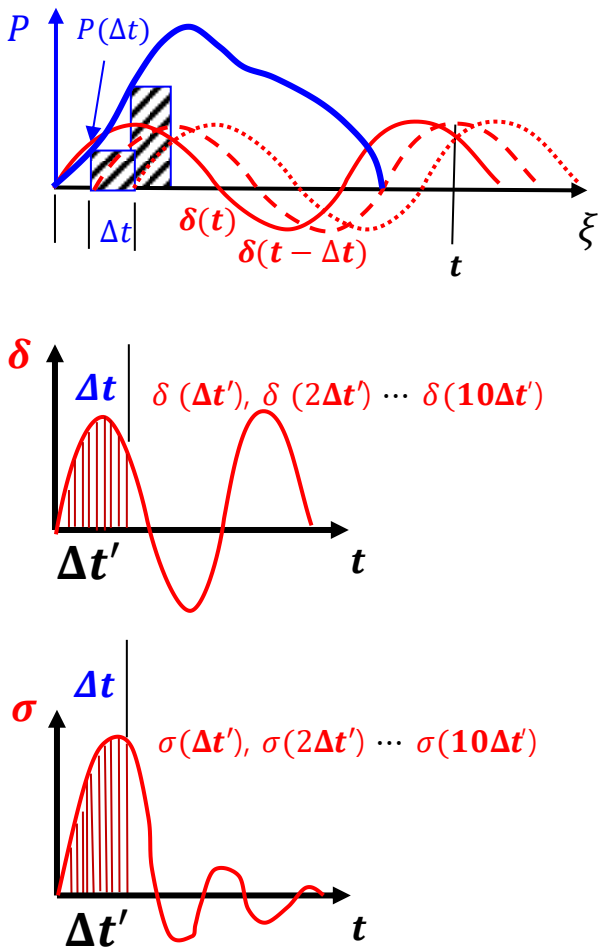

Fig. 65. Application of high resolution to stress response

In Eq. (18), sloshing pressure and the stress response to it are expressed as vectors at a specific time. The stress response of unit pressure is expressed in matrix form. To reduce the time dimension, sloshing pressure $\{P(t)\}$ and stress response of sloshing pressure $\{\sigma(t)\}$ are transformed into Eq. (19) and Eq. (20), respectively. $P_1(\Delta t) \sim P_1(q\Delta t)$ represents the sloshing pressure applied to R1, and $P_4(\Delta t) \sim P_4(q\Delta t)$ means the sloshing pressure applied to R4. $\sigma_1(0), \sigma_1(\Delta t'), \cdots, \sigma_1(q\Delta t)$ corresponds to the stress response measured at the first measurement point. $\sigma_{25}(0), \sigma_{25}(\Delta t'), \cdots, \sigma_{25}(q\Delta t)$ represents the measured stress response at the 25th measurement point.

$$\{P(t)\}_{|_{t=\Delta t:\Delta t:q\Delta t}} = \begin{Bmatrix} P_1(t) \\ \vdots \\ P_4(t) \end{Bmatrix}_{|_{t=\Delta t:\Delta t:q\Delta t}} = \begin{Bmatrix} P_1(\Delta t) \\ P_2(\Delta t) \\ P_3(\Delta t) \\ P_4(\Delta t) \\ P_1(2\Delta t) \\ P_2(2\Delta t) \\ P_3(2\Delta t) \\ P_4(2\Delta t) \\ \vdots \\ P_1(q\Delta t) \\ P_2(q\Delta t) \\ P_3(q\Delta t) \\ P_4(q\Delta t) \end{Bmatrix} \cdots (19)$$

$$\{\sigma(t)\}_{|t=0:\Delta t\prime:q\Delta t} = \begin{Bmatrix} \sigma_1(t) \\ \sigma_2(t) \\ \vdots \\ \sigma_{25}(t) \end{Bmatrix}_{|t=\Delta t:\Delta t\prime:q\Delta t} = \begin{Bmatrix} \sigma_1(\Delta t) \\ \sigma_2(\Delta t) \\ \vdots \\ \sigma_{25}(\Delta t) \\ \sigma_1(\Delta t+\Delta t') \\ \sigma_2(\Delta t+\Delta t') \\ \vdots \\ \sigma_{25}(\Delta t+\Delta t') \\ \vdots \\ \sigma_1(2\Delta t) \\ \sigma_2(2\Delta t) \\ \vdots \\ \sigma_{25}(2\Delta t) \\ \sigma_1(2\Delta t+\Delta t') \\ \sigma_2(2\Delta t+\Delta t') \\ \vdots \\ \sigma_{25}(2\Delta t+\Delta t') \\ \vdots \\ \sigma_1(q\Delta t) \\ \sigma_2(q\Delta t) \\ \vdots \\ \sigma_{25}(q\Delta t) \end{Bmatrix} \cdots (20)$$

In Eq. (18), if sloshing pressure is replaced with Eq. (19) and the stress response of sloshing pressure is replaced with Eq. (20), the corresponding stress response of unit pressure can be shown as in Eq. (21) below. The first column of Eq. (21) indicates the calculated stress response when the unit pressure is applied to R1. The second column is composed of the calculated stress response when the unit pressure is applied to R2. The cells filled with 0 represent the result of time shifting of unit pressure stress responses.

$$
\begin{bmatrix}
\delta_1^1(\Delta t) & \delta_1^2(\Delta t) & \delta_1^4(\Delta t) & 0 & 0 \\
\delta_2^1(\Delta t) & \delta_2^2(\Delta t) & \delta_2^4(\Delta t) & 0 & 0 \\
\vdots & \vdots & \vdots & \vdots & \vdots \\
\delta_{25}^1(\Delta t) & \delta_{25}^2(\Delta t) & \delta_{25}^4(\Delta t) & 0 & 0 \\
\delta_1^1(\Delta t+\Delta t') & \delta_1^2(\Delta t+\Delta t') & \delta_1^4(\Delta t+\Delta t') & 0 & 0 \\
\delta_2^1(\Delta t+\Delta t') & \delta_2^2(\Delta t+\Delta t') & \delta_2^4(\Delta t+\Delta t') & 0 & 0 \\
\vdots & \vdots & \vdots & \vdots & \vdots \\
\delta_{25}^1(\Delta t+\Delta t') & \delta_{25}^2(\Delta t+\Delta t') & \delta_{25}^4(\Delta t+\Delta t') & 0 & 0 \\
\vdots & \vdots & \vdots & \vdots & \vdots \\
\delta_1^1(2\Delta t) & \delta_1^2(2\Delta t) & \delta_1^4(2\Delta t) & \delta_1^1(\Delta t) & \delta_1^2(\Delta t) \\
\delta_2^1(2\Delta t) & \delta_2^2(2\Delta t) & \delta_2^4(2\Delta t) & \delta_2^1(\Delta t) & \delta_2^2(\Delta t) \\
\vdots & \vdots & \cdots \quad \vdots & \vdots & \vdots \\
\delta_{25}^1(2\Delta t) & \delta_{25}^2(2\Delta t) & \delta_{25}^4(2\Delta t) & \delta_{25}^1(\Delta t) & \delta_{25}^2(\Delta t) \\
\delta_1^1(2\Delta t+\Delta t') & \delta_1^2(2\Delta t+\Delta t') & \delta_1^4(2\Delta t+\Delta t') & \delta_1^1(\Delta t+\Delta t') & \delta_1^2(\Delta t+\Delta t') \\
\delta_2^1(2\Delta t+\Delta t') & \delta_2^2(2\Delta t+\Delta t') & \delta_2^4(2\Delta t+\Delta t') & \delta_2^1(\Delta t+\Delta t') & \delta_2^2(\Delta t+\Delta t') \\
\vdots & \vdots & \vdots & \vdots & \vdots \\
\delta_{25}^1(2\Delta t+\Delta t') & \delta_{25}^2(2\Delta t+\Delta t') & \delta_{25}^4(2\Delta t+\Delta t') & \delta_{25}^1(\Delta t+\Delta t') & \delta_{25}^2(\Delta t+\Delta t') \\
\vdots & \vdots & \vdots & \vdots & \vdots \\
\delta_1^1(q\Delta t) & \delta_1^2(q\Delta t) & \delta_1^4(q\Delta t) & \delta_1^1\big((q-1)\Delta t\big) & \delta_1^2\big((q-1)\Delta t\big) \\
\delta_2^1(q\Delta t) & \delta_2^2(q\Delta t) & \delta_2^4(q\Delta t) & \delta_2^1\big((q-1)\Delta t\big) & \delta_2^2\big((q-1)\Delta t\big) \\
\delta_3^1(q\Delta t) & \delta_3^2(q\Delta t) & \delta_3^4(q\Delta t) & \delta_3^1\big((q-1)\Delta t\big) & \delta_3^2\big((q-1)\Delta t\big) \\
\vdots & \vdots & \vdots & \vdots & \vdots \\
\delta_{25}^1(q\Delta t) & \delta_{25}^2(q\Delta t) & \delta_{25}^4(q\Delta t) & \delta_{25}^1\big((q-1)\Delta t\big) & \delta_{25}^2\big((q-1)\Delta t\big)
\end{bmatrix}
$$

$$
\begin{bmatrix}
0 & 0 & 0 \\
0 & 0 & 0 \\
\vdots & \vdots & \vdots \\
0 & 0 & 0 \\
0 & 0 & 0 \\
0 & 0 & 0 \\
\vdots & \vdots & \vdots \\
0 & 0 & 0 \\
\vdots & \vdots & \vdots \\
\delta_1^4(\Delta t) & 0 & 0 \\
\delta_2^4(\Delta t) & 0 & 0 \\
\vdots & \vdots & \vdots \\
\cdots \quad \delta_{25}^4(\Delta t) & \cdots \quad 0 & \cdots \quad 0 \\
\delta_1^4(\Delta t+\Delta t') & 0 & 0 \\
\delta_2^4(\Delta t+\Delta t') & 0 & 0 \\
\vdots & \vdots & \vdots \\
\delta_{25}^4(\Delta t+\Delta t') & 0 & 0 \\
\vdots & \vdots & \vdots \\
\delta_1^4\big((q-1)\Delta t\big) & \delta_1^1(\Delta t) & \delta_1^2(\Delta t) \\
\delta_2^4\big((q-1)\Delta t\big) & \delta_2^1(\Delta t) & \delta_2^2(\Delta t) \\
\delta_3^4\big((q-1)\Delta t\big) & \delta_3^1(\Delta t) & \delta_3^2(\Delta t) \\
\vdots & \vdots & \vdots \\
\delta_{25}^4\big((q-1)\Delta t\big) & \delta_{25}^1(\Delta t) & \delta_{25}^2(\Delta t)
\end{bmatrix}
\begin{bmatrix}
0 \\ 0 \\ \vdots \\ 0 \\ 0 \\ 0 \\ \vdots \\ 0 \\ \vdots \\ \delta_1^4(\Delta t) \\ \delta_2^4(\Delta t) \\ \vdots \\ \cdots \quad \delta_{25}^4(\Delta t) \\ \delta_1^4(\Delta t+\Delta t') \\ \delta_2^4(\Delta t+\Delta t') \\ \vdots \\ \delta_{25}^4(\Delta t+\Delta t') \\ \vdots \\ \delta_1^4\big((q-1)\Delta t\big) \\ \delta_2^4\big((q-1)\Delta t\big) \\ \delta_3^4\big((q-1)\Delta t\big) \\ \vdots \\ \delta_{25}^4\big((q-1)\Delta t\big)
\end{bmatrix}
\begin{bmatrix}
0 \\ 0 \\ \vdots \\ 0 \\ 0 \\ 0 \\ \vdots \\ 0 \\ \vdots \\ 0 \\ 0 \\ \vdots \\ \cdots \quad 0 \\ 0 \\ 0 \\ \vdots \\ 0 \\ \vdots \\ \delta_1^4(\Delta t) \\ \delta_2^4(\Delta t) \\ \delta_3^4(\Delta t) \\ \vdots \\ \delta_{25}^4(\Delta t)
\end{bmatrix}
$$

$$\cdots (21)$$

From Eqs. (19) to (21), Eq. (18) is transformed into a system of linear equations as in Eq. (22). If K is the number of regions wherein the sloshing pressure is applied, and I is the number of points where the stress response is measured, Eqs. (19) to (21) can be generalized to Eqs. (23) to (25). The generalized mathematical formulation can be expressed as Eq. (26). In Eq. (26), the matrix composed of the values of unit pressure stress response ($[\hat{\delta}]$) has a size of $(\frac{\Delta t}{\Delta t'} \cdot q + 1)I\ by\ Kq$. The sloshing pressure vector ($\{P\}$) has a size of $Kq\ by\ 1$. The vector corresponding to the stress response of sloshing pressure ($\{\sigma\}$) has a size of $(\frac{\Delta t}{\Delta t'} \cdot q + 1)I\ by\ 1$.

$$[\hat{\delta}]\{P\} = \{\sigma\} \cdots (22)$$

where,

$[\hat{\delta}]$: see Eq. (21)

$\{P\}$: see Eq. (19)

$\{\sigma\}$: see Eq. (20)

$$\{P(t)\}_{|_{t=\Delta t:\Delta t:q\Delta t}} = \begin{Bmatrix} P_1(t) \\ \vdots \\ P_K(t) \end{Bmatrix}_{|_{t=\Delta t:\Delta t:q\Delta t}} = \begin{Bmatrix} P_1(\Delta t) \\ P_2(\Delta t) \\ P_3(\Delta t) \\ P_K(\Delta t) \\ P_1(2\Delta t) \\ P_2(2\Delta t) \\ P_3(2\Delta t) \\ P_K(2\Delta t) \\ \vdots \\ P_1(q\Delta t) \\ P_2(q\Delta t) \\ P_3(q\Delta t) \\ P_K(q\Delta t) \end{Bmatrix} \cdots (23)$$

where

K: The number of sloshing pressure application regions

$$\{\sigma(t)\}_{|_{t=0:\Delta t\prime:q\Delta t}} = \begin{Bmatrix} \sigma_1(t) \\ \sigma_2(t) \\ \vdots \\ \sigma_I(t) \end{Bmatrix}_{|_{t=\Delta t:\Delta t\prime:q\Delta t}} = \begin{Bmatrix} \sigma_1(\Delta t) \\ \sigma_2(\Delta t) \\ \vdots \\ \sigma_I(\Delta t) \\ \sigma_1(\Delta t + \Delta t') \\ \sigma_2(\Delta t + \Delta t') \\ \vdots \\ \sigma_I(\Delta t + \Delta t') \\ \vdots \\ \sigma_1(2\Delta t) \\ \sigma_2(2\Delta t) \\ \vdots \\ \sigma_I(2\Delta t) \\ \sigma_1(2\Delta t + \Delta t') \\ \sigma_2(2\Delta t + \Delta t') \\ \vdots \\ \sigma_I(2\Delta t + \Delta t') \\ \vdots \\ \sigma_1(q\Delta t) \\ \sigma_2(q\Delta t) \\ \vdots \\ \sigma_I(q\Delta t) \end{Bmatrix} \cdots (24)$$

where

I: The number of stress response measurement points

$$
\begin{bmatrix}
\delta_1^1(\Delta t) & \delta_1^2(\Delta t) & \delta_1^K(\Delta t) & 0 & 0 \\
\delta_2^1(\Delta t) & \delta_2^2(\Delta t) & \delta_2^K(\Delta t) & 0 & 0 \\
\vdots & \vdots & \vdots & \vdots & \vdots \\
\delta_I^1(\Delta t) & \delta_I^2(\Delta t) & \delta_I^K(\Delta t) & 0 & 0 \\
\delta_1^1(\Delta t+\Delta t') & \delta_1^2(\Delta t+\Delta t') & \delta_1^K(\Delta t+\Delta t') & 0 & 0 \\
\delta_2^1(\Delta t+\Delta t') & \delta_2^2(\Delta t+\Delta t') & \delta_2^K(\Delta t+\Delta t') & \vdots & \vdots \\
\vdots & \vdots & \vdots & 0 & 0 \\
\delta_I^1(\Delta t+\Delta t') & \delta_I^2(\Delta t+\Delta t') & \delta_I^K(\Delta t+\Delta t') & \vdots & \vdots \\
\vdots & \vdots & \vdots & \delta_1^1(\Delta t) & \delta_1^2(\Delta t) \\
\delta_1^1(2\Delta t) & \delta_1^2(2\Delta t) & \delta_1^K(2\Delta t) & \delta_2^1(\Delta t) & \delta_2^2(\Delta t) \\
\delta_2^1(2\Delta t) & \delta_2^2(2\Delta t) & \delta_2^K(2\Delta t) & \vdots & \vdots \\
\vdots & \vdots & \vdots & \delta_I^1(\Delta t) & \delta_I^2(\Delta t) \\
\delta_I^1(2\Delta t) & \delta_I^2(2\Delta t) & \delta_I^K(2\Delta t) & \delta_1^1(\Delta t+\Delta t') & \delta_1^2(\Delta t+\Delta t') \\
\delta_1^1(2\Delta t+\Delta t') & \delta_1^2(2\Delta t+\Delta t') & \delta_1^K(2\Delta t+\Delta t') & \delta_2^1(\Delta t+\Delta t') & \delta_2^2(\Delta t+\Delta t') \\
\delta_2^1(2\Delta t+\Delta t') & \delta_2^2(2\Delta t+\Delta t') & \delta_2^K(2\Delta t+\Delta t') & \vdots & \vdots \\
\vdots & \vdots & \vdots & \delta_I^1(\Delta t+\Delta t') & \delta_I^2(\Delta t+\Delta t') \\
\delta_I^1(2\Delta t+\Delta t') & \delta_I^2(2\Delta t+\Delta t') & \delta_I^K(2\Delta t+\Delta t') & \vdots & \vdots \\
\vdots & \vdots & \vdots & \delta_1^1\big((q-1)\Delta t\big) & \delta_1^2\big((q-1)\Delta t\big) \\
\delta_1^1(q\Delta t) & \delta_1^2(q\Delta t) & \delta_1^K(q\Delta t) & \delta_2^1\big((q-1)\Delta t\big) & \delta_2^2\big((q-1)\Delta t\big) \\
\delta_2^1(q\Delta t) & \delta_2^2(q\Delta t) & \delta_2^K(q\Delta t) & \delta_3^1\big((q-1)\Delta t\big) & \delta_3^2\big((q-1)\Delta t\big) \\
\delta_3^1(q\Delta t) & \delta_3^2(q\Delta t) & \delta_3^K(q\Delta t) & \vdots & \vdots \\
\vdots & \vdots & \vdots & \delta_I^1\big((q-1)\Delta t\big) & \delta_I^2\big((q-1)\Delta t\big) \\
\delta_I^1(q\Delta t) & \delta_I^2(q\Delta t) & \delta_I^K(q\Delta t) &
\end{bmatrix}
$$

$$
\begin{bmatrix}
0 & 0 & 0 \\
0 & 0 & 0 \\
\vdots & \vdots & \vdots \\
0 & 0 & 0 \\
0 & 0 & 0 \\
0 & 0 & 0 \\
\vdots & \vdots & \vdots \\
0 & 0 & 0 \\
\vdots & \vdots & \vdots \\
\delta_1^K(\Delta t) & 0 & 0 \\
\delta_2^K(\Delta t) & 0 & 0 \\
\vdots & \vdots & \vdots \\
\cdots\ \delta_I^K(\Delta t) & \cdots\ 0 & \cdots\ 0 \\
\delta_1^K(\Delta t+\Delta t') & 0 & 0 \\
\delta_2^K(\Delta t+\Delta t') & 0 & 0 \\
\vdots & \vdots & \vdots \\
\delta_I^K(\Delta t+\Delta t') & 0 & 0 \\
\vdots & \vdots & \vdots \\
\delta_1^K\big((q-1)\Delta t\big) & \delta_1^1(\Delta t)\ \delta_1^2(\Delta t) & \delta_1^K(\Delta t) \\
\delta_2^K\big((q-1)\Delta t\big) & \delta_2^1(\Delta t)\ \delta_2^2(\Delta t) & \delta_2^K(\Delta t) \\
\delta_3^K\big((q-1)\Delta t\big) & \delta_3^1(\Delta t)\ \delta_3^2(\Delta t) & \delta_3^K(\Delta t) \\
\vdots & \vdots & \vdots \\
\delta_I^K\big((q-1)\Delta t\big) & \delta_I^1(\Delta t)\ \delta_I^2(\Delta t) & \delta_I^K(\Delta t)
\end{bmatrix}
$$

$$\cdots(25)$$

$$\left[\widehat{\delta_G}\right]\{P_G\} = \{\sigma_G\} \cdots (26)$$

where,

$\left[\widehat{\delta_G}\right]$: see Eq. (25)

$\{P_G\}$: see Eq. (23)

$\{\sigma_G\}$: see Eq. (24)

By substituting the calculated unit pressure stress response and the measured stress response of sloshing pressure into Eq. (26), the corresponding sloshing pressure can be calculated. Because the number of measured stress responses is larger than the predicted number of sloshing pressure amplitudes, the least-square method is used to solve Eq. (26).

In the sloshing pressure, no large negative pressure amplitude appears. A lower-bound constraint condition is applied to increase the stability of the sloshing pressure predicted from the least square method. When measuring the stress response of the supporting structure, noise may occur due to various factors. In order to reduce the effect of noise on the predicted sloshing pressure, a curvature constraint condition is additionally introduced. A term for a curvature constraint can be written as in Eq. (27). Figure 66 shows the concept of the curvature constraint condition. It has a directionality to minimize the difference between the predicted pressure amplitude at $t = (n + 1)\Delta t$ and the average value of the predicted pressure amplitude at $t = n\Delta t$ and $t = (n + 2)\Delta t$. The factor ρ that determines the intensity of the curvature constraint condition is defined. As ρ

increases, the smoothness of the predicted sloshing pressure increases.

However, if too large a ρ is selected, the effect of Eq. (27) becomes larger than that of Eq. (26), which may lead to incorrect sloshing pressure prediction. In this research, it was verified, through a series of case studies, that $\rho = 10^7$ is suitable.

$$[D]\{P\} = \begin{bmatrix} 0 & 0 & 0 & 0 & \cdots & \cdots & \cdots & \cdots & 0 \\ 1 & -2 & 1 & 0 & \cdots & \cdots & \cdots & \cdots & 0 \\ 0 & 1 & -2 & 1 & \cdots & \cdots & \cdots & \cdots & 0 \\ & & & & \vdots & & & & \\ & & & & \vdots & & & & \\ & & & & \vdots & & & & \\ 0 & 0 & 0 & 0 & \cdots & \cdots & 1 & -2 & 1 \\ 0 & 0 & 0 & 0 & \cdots & \cdots & 0 & 0 & 0 \end{bmatrix} \begin{Bmatrix} P_1(\Delta t) \\ P_1(2\Delta t) \\ \vdots \\ P_1(q\Delta t) \\ \vdots \\ P_K(\Delta t) \\ P_K(2\Delta t) \\ \vdots \\ P_K(q\Delta t) \end{Bmatrix} \cdots (27)$$

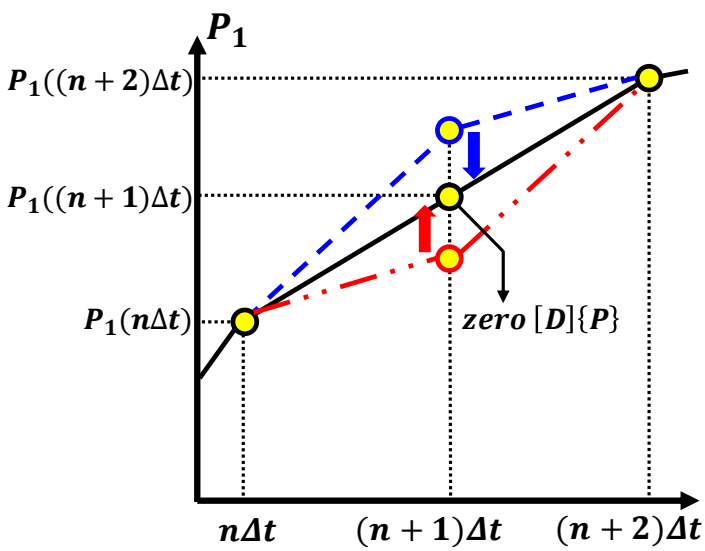

Fig. 66. Schematic of curvature constraint condition

The formula to which the curvature constraint condition is applied

is represented by Eq. (28). The sloshing pressure can be predicted by solving for Eq. (28) using the least square method.

$$\begin{bmatrix} \hat{\delta} \\ \rho D \end{bmatrix} \{P\} = \begin{Bmatrix} \sigma \\ 0 \end{Bmatrix} \cdots (28)$$

where

$\{\sigma\}$: stress response of sloshing pressure

$[\delta]$: stress response of unit pressure

$\{P\}$: sloshing pressure

$[\rho D]$: curvature constraint term

4.2.3. Prediction of hot spot stress response

Compression is generated on the insulation panel by sloshing pressure. The typical failure modes that can occur in an LNG CCS are vertical crushing of PUF, plywood and mastic as well as shear failure at the connection between the bottom plywood and mastic. The stress generated in the insulation panel is relatively large in the area where the stiffener or girder passes. As shown in Fig. 67, a total of 4 positions were selected near the girder for comparison of vertical stress occurring in PUF. Figure 68 shows the calculated vertical stress in PUF at each location. The highest stress concentration is observed in location L1 due to the influence of the presence of the girder.

As shown in Fig. 69, the locations where the girder passes were adopted as the hot spot points for prediction of stress response. Since shear failure does not appear in PUF, only the stress response of

vertical crushing was considered. For mastic and plywood, both vertical crushing and shear failure predictions were carried out. The total of 7 stress responses for which prediction was performed are as follows.

- PUF: vertical crushing (σ_z)
- Mastic: vertical crushing (σ_z), shear failure (σ_{zx})
- Plywood1: vertical crushing (σ_z), shear failure (σ_{zx})
- Plywood2: vertical crushing (σ_z), shear failure (σ_{zx})

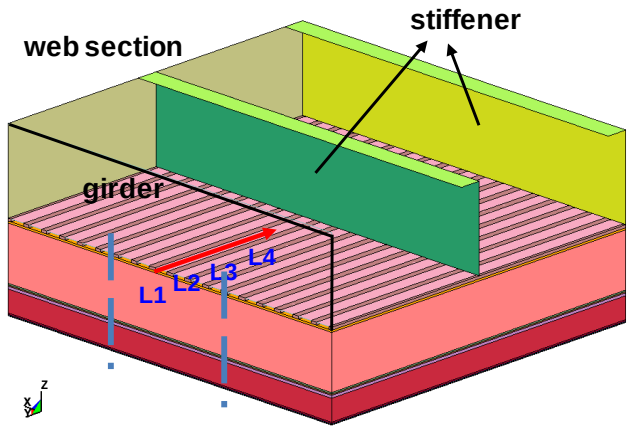

Fig. 67. Selected locations for stress response comparison

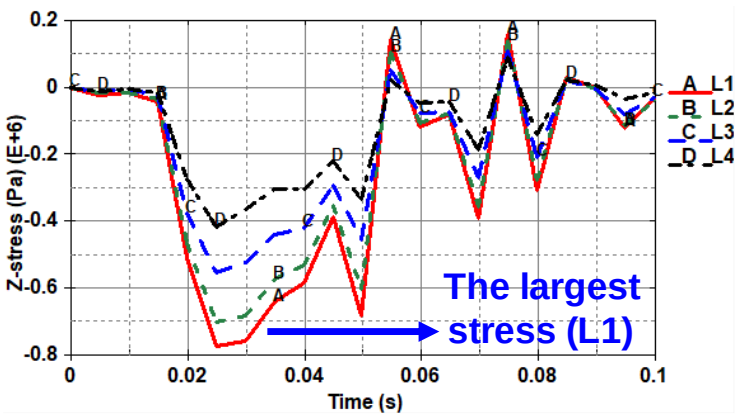

Fig. 68. Comparison of vertical stress in PUF

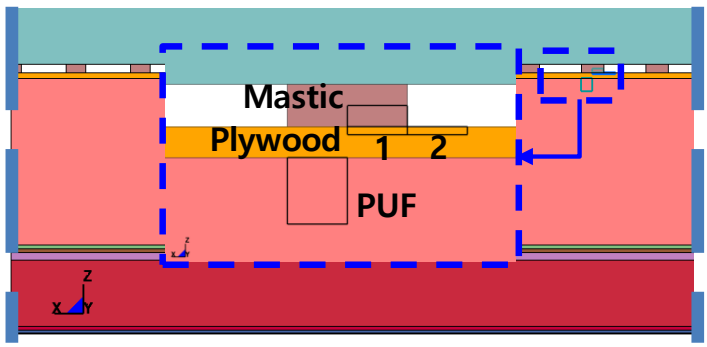

Fig. 69. Selected locations for stress response prediction

To predict the stress response at selected hot spots using the impulse/space superposition method, hot spot stress responses to unit pressure are required. As illustrated in Fig. 70, unit pressure was applied to each region, as in Section 2.2.1. Then, instead of calculating the stress response at 25 measurement points, the stress responses at the hot spots were obtained. Seven hot spot stress responses were calculated for each of the four loading conditions.

Fig. 71 shows the seven hot spot stress responses generated by the unit pressure. The selected hot spot location is adjacent to R1 and R2. As a result, looking at the calculated hot spot stress responses, the effect of the loading condition with unit pressure applied to R1 and R2 appears to be dominant. The shapes of the vertical stress profile in PUF, mastic and plywood were similar due to the linear system assumption. In the case of shear stress, the highest value was observed in plywood2, which exhibited geometrical discontinuity.

By changing the location of the hot spot for calculation of the stress

response of unit pressure, the sloshing pressure stress response can be predicted for any location.

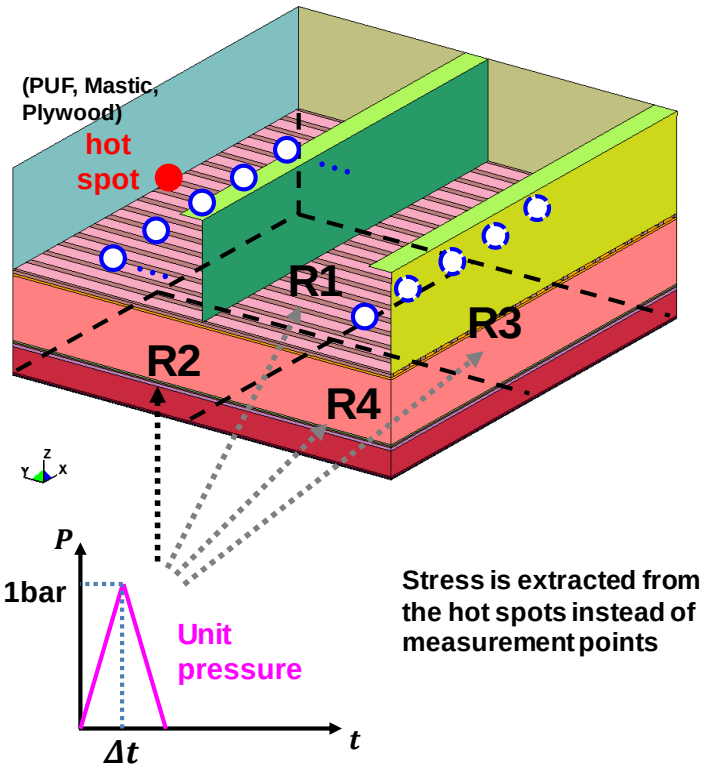

Fig. 70. Loading conditions for calculation of hot spot stress response of unit pressure

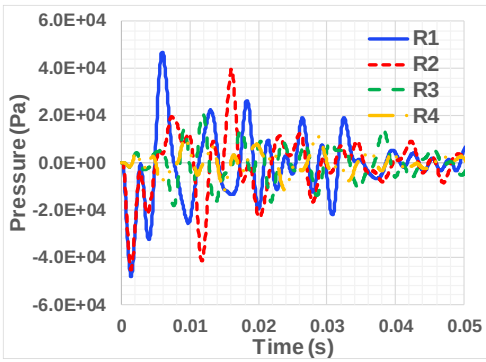

PUF (σ_z)

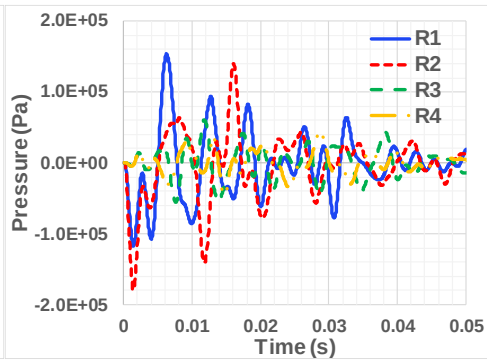

Mastic (σ_z)

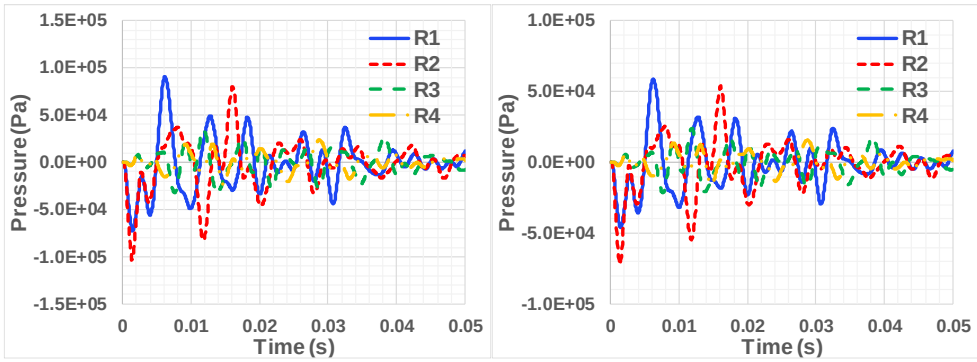

Plywood1 (σ_z)

Plywood2 (σ_z)

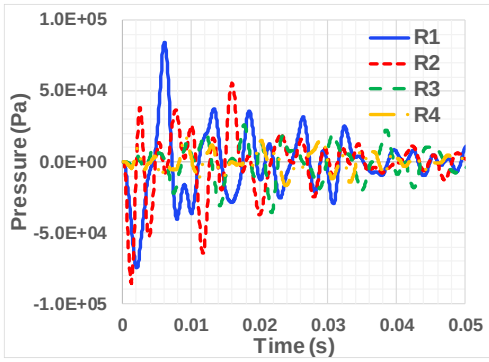

Mastic (σ_{zx})

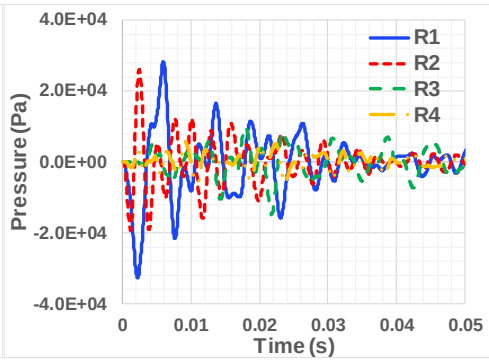

Plywood1 (σ_{zx})

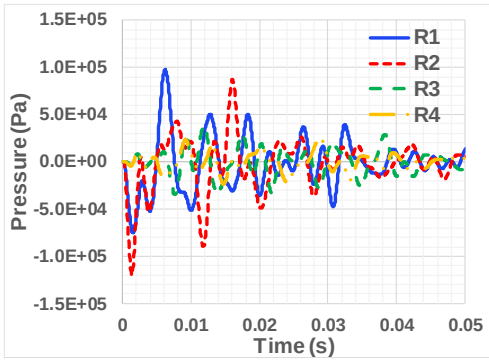

Plywood2 (σ_{zx})

Fig. 71. Calculated hot spot stress response of unit pressure

The hot spot stress response generated by the predicted sloshing pressure can be calculated using the impulse/space superposition method. The results shown in Fig. 71 were applied as unit load

responses. When predicting hot spot stress response, applied load and unit load response are the given values. Thus, there is no need to use the least square method or optimization to calculate the hot spot stress response. By substituting the predicted sloshing pressure and calculated hot spot stress response of unit pressure in Eq. (13), the hot spot stress response for sloshing pressure can be calculated directly. It can be written as Eq. (29).

$$\sigma_{hs_p}(t) = \sum_{k=1}^{4} \int_0^t P_k(\xi) \delta_{hs_p}^k (t - \xi) d\xi \cdots (29)$$

where,

p: The number of predicted hot spot stress response

$\sigma_{hs}(t)$: hot spot stress response of sloshing pressure

$P_k(t)$: sloshing pressure on k^{th} region

$\delta_{hs}^k(t)$: hot spot stress response when unit load is applied to k^{th} region

Stress response prediction using impulse/space superposition is based on the predicted sloshing pressure. Sloshing pressure is obtained in a specific area unit. Thus, in predicting hot spot stress response, the effect of pressure change within the selected region is not considered. Continuous impact appears in the actual sloshing phenomenon (Bogaert et al [55]). In that case, the error between the predicted hot spot stress response and the actual hot spot stress response is relatively large. The more detailed the area unit for predicting sloshing pressure is, the less the effect of error caused by continuous impact will be.

4.3. Prediction of Sloshing Pressure and LNG CCS Structural Response using Mode Superposition Method

Separately from the impulse/space superposition method, the relationship between the applied load and the structural response can be derived using the mode superposition method. When the sloshing pressure is given, the stress response generated in an LNG CCS is appropriately estimated through the mode superposition method. However, it has been confirmed that the reverse process of predicting sloshing pressure from the measured stress response includes considerable instability. In order to predict sloshing pressure using the mode superposition method, the numerical difference process for modal amplitude is required. If some noise or error occurs in modal amplitude, this effect is amplified in the predicted sloshing pressure. There is no numerical difference process for modal amplitude in predicting the hot spot stress response. The hot spot stress response of sloshing pressure is determined only by modal amplitude. The accuracy of modal amplitude estimation can be improved by selecting proper modes. In the case of the mode superposition method, the sloshing pressure obtained in a specific area unit is not used. Therefore, it can be applied to predict the hot spot stress response of sloshing pressure under any impact condition.

4.3.1. Mode superposition method

In the mode superposition method, the structural response is expressed as the product of the modal amplitude and the modal matrix obtained from the modal analysis. When all modes equal to the number of degrees of freedom (DOF) of the system are considered, the exact structural response can be calculated by the mode superposition method. In reality, there is a limitation on taking all modes into account, though in the case of high-order modes, the effect on the solution is small. As shown in Eq. (30), in general, the mode superposition method is applied only from the 1st mode to the mode of a specific order (Cho et al [72], Rixen [73]).

$$\{x(t)\} \approx \sum_{i=1}^{l} \phi_i \, q_i(t) = [\phi]\{q(t)\} \cdots (30)$$

where,

$\boldsymbol{l}$: the number of selected modes

$\{\boldsymbol{x}(\boldsymbol{t})\}$: structure response

$\{\boldsymbol{q}(\boldsymbol{t})\}$: modal amplitude

$[\boldsymbol{\phi}]$: modal matrix

Modal analysis was carried out on a given LNG CCS model in order to select an appropriate number of modes. Through the modal analysis, the modal participation factor could be obtained along with eigenvalues and eigenvectors according to each mode. The square value of the modal participation factor means the value of the modal effective mass fraction. This is a quantitative factor indicating the

contribution of each mode. Figure 72 shows the modal effective mass fraction results for each mode in the LNG CCS model. The influence of the z-direction was the most dominant, and mode no.3 had the highest contribution. Summing the values of the modal effective mass fraction up to the 20th mode reached about 90%. When using the mode superposition method, it is sufficient to consider the 1st mode to the 20th mode.

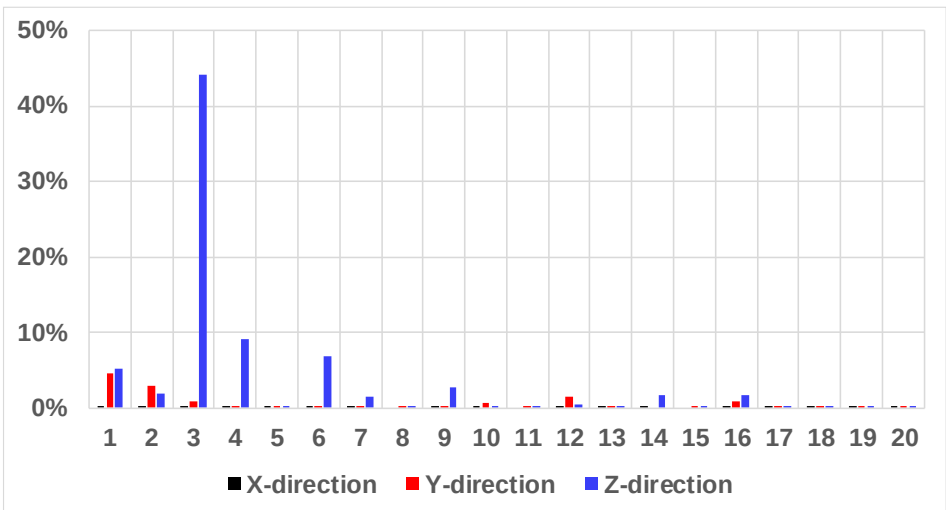

Fig. 72. Calculated modal effective mass fraction

For each degree of freedom of the system, the equation of motion can be written as Eq. (31). By substituting Eq. (30) into Eq. (31), the equation for structural response is converted to the equation for modal amplitude. If both sides of the transformed equation are multiplied by the transpose of the modal matrix, decoupling of the equation of motion can be achieved.

$$[M]\{\ddot{x}(t)\} + [C]\{\dot{x}(t)\} + [K]\{x(t)\} = \{F(t)\} \cdots (31)$$

where,

$[M]: mass\ \ matrix$

$[C]: damping\ \ matrix$

$[K]: stiffness\ \ matrix$

$\{F(t)\}: applied\ \ load\ \ vector$

Eq. (32) shows the process for deriving the decoupled equation. When mass normalization is applied in the modal analysis process, the term composed of the mass matrix and the modal matrix becomes an identity matrix, and the term composed of the stiffness matrix and the modal matrix becomes a diagonal matrix having eigenvalues as diagonal elements. For damping, Rayleigh damping, which is equal to proportional damping, is used. Between mass damping and stiffness damping, mass damping is adopted. Thus, the term composed of the damping matrix and the modal matrix is expressed as a mass damping coefficient value.

$$[M]\{\ddot{x}(t)\} + [C]\{\dot{x}(t)\} + [K]\{x(t)\} = \{F(t)\}$$

$$[M][\phi]\{\ddot{q}(t)\} + [C][\phi]\{\dot{q}(t)\} + [K][\phi]\{q(t)\} = \{F(t)\}$$

$$[\phi]^T[M][\phi]\{\ddot{q}(t)\} + [\phi]^T[C][\phi]\{\dot{q}(t)\} + [\phi]^T[K][\phi]\{q(t)\} = [\phi]^T\{F(t)\}$$

$$\{\ddot{q}(t)\} + \alpha\{\dot{q}(t)\} + [\lambda]\{q(t)\} = \left[\tilde{\phi}\right]^T\{F(t)\}\ \ (mass\ \ normalization) \cdots (32)$$

where,

α: mass damping coefficient

$[\lambda]$: eigenvalue matrix(diagonal term = eigenvalue)

From Eq. (30) and Eq. (31), the relationship between the structural response and the applied load is established. Given applied load $\{F(t)\}$, the corresponding modal amplitude is calculated from Eq. (32). By substituting the calculated modal amplitude into Eq. (30), structural response is obtained. Conversely, given structural response $\{x(t)\}$, the corresponding modal amplitude is calculated from Eq. (30). By substituting the calculated modal amplitude into Eq. (32), the applied load can be estimated.

4.3.2. Prediction of sloshing pressure

4.3.2.1. Calculation of response corresponding to applied load

The calculation of in-plane stress response was carried out at the measurement points by applying a specific pressure to R1~R4, as shown in Fig. 73. The Newmark-beta method was utilized to calculate the modal amplitude. 1/6 and 1/2 values were applied to the coefficients β and γ as required for the Newmark-beta method, respectively.

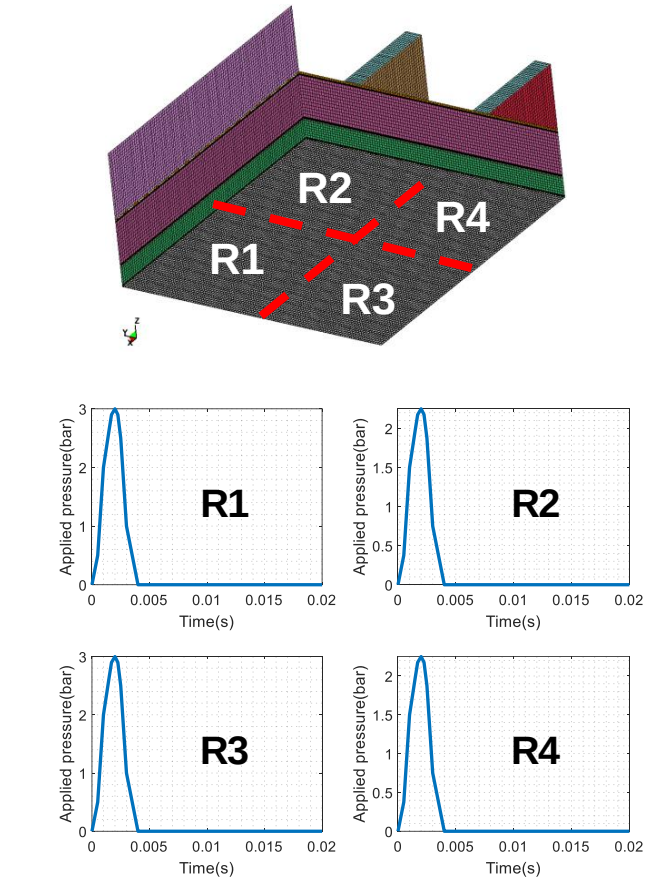

Fig. 73. Applied pressure

Figures 74, 75, and 76 show the results for modal amplitude ($\{q(t)\}$), modal amplitude velocity ($\{\dot{q}(t)\}$), and modal amplitude acceleration ($\{\ddot{q}(t)\}$), respectively, as calculated using the Newmark-beta method. The x-axis represents time. All three sets of results show a smooth profile without noise. By multiplying the calculated modal amplitude by the modal matrix, the structural response at the desired points can be estimated. Figure 77 compares the results predicted from the mode superposition method with those obtained from transient analysis for in-plane stress at 25 measurement points. The x-axis represents time and the y-axis represents stress

amplitude (unit: Pa). Except for positions no.1 and no.2, where the stress amplitude is relatively small, the two results agree well. A slight error occurring at positions no.1 and no.2 was reduced by increasing the number of modes to be considered.

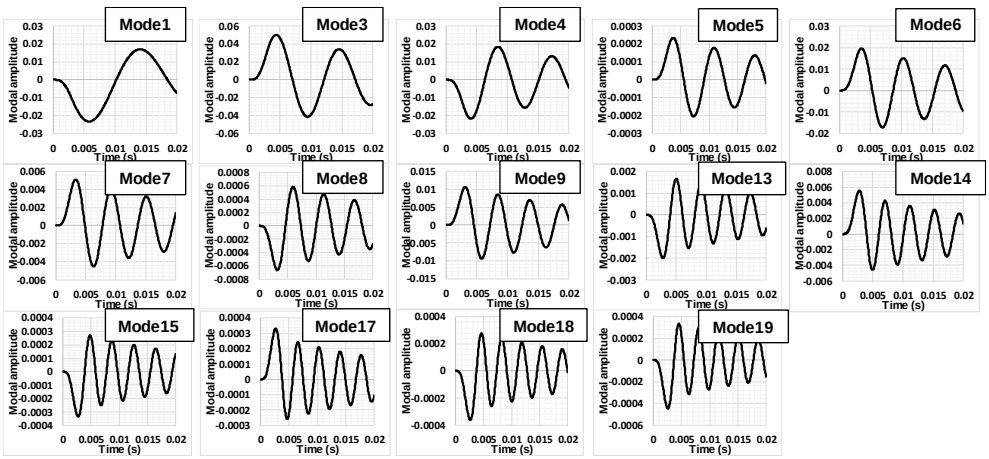

Fig. 74. Calculated modal amplitude ($\{q(t)\}$)

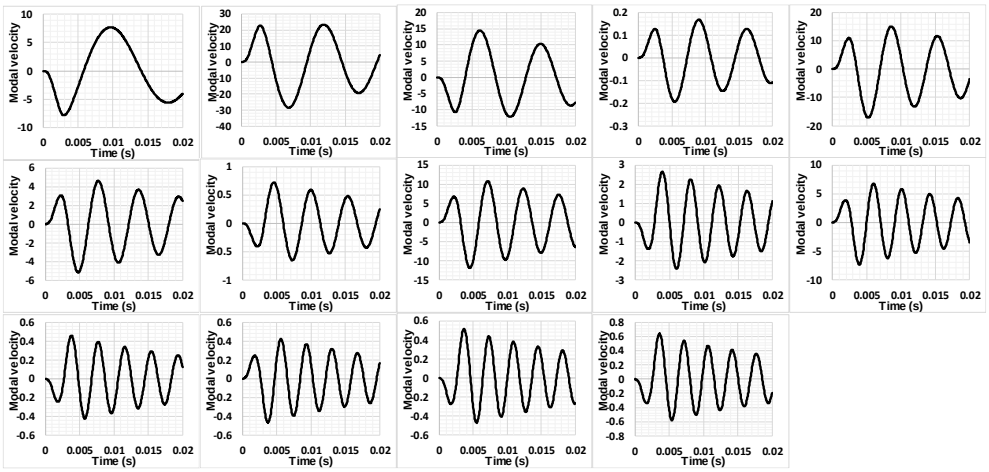

Fig. 75. Calculated velocity of modal amplitude ($\{\dot{q}(t)\}$)

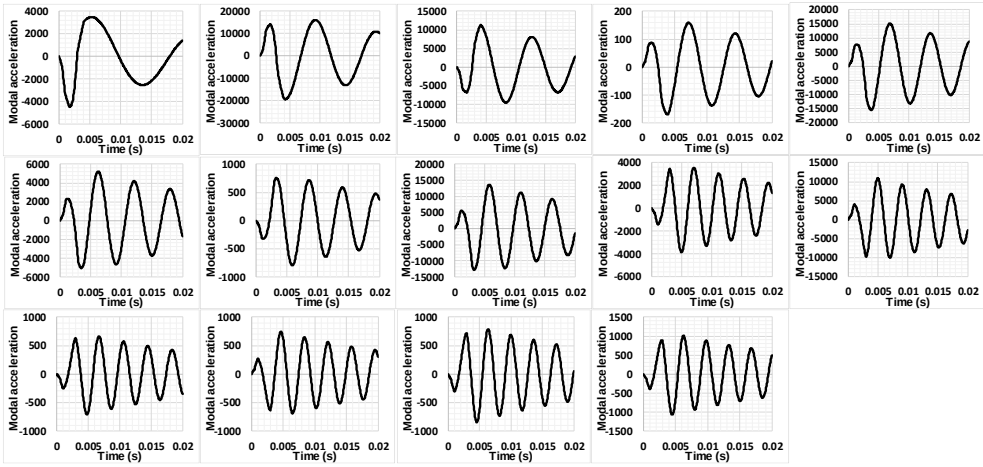

Fig. 76. Calculated acceleration of modal amplitude ($\{\ddot{q}(t)\}$)

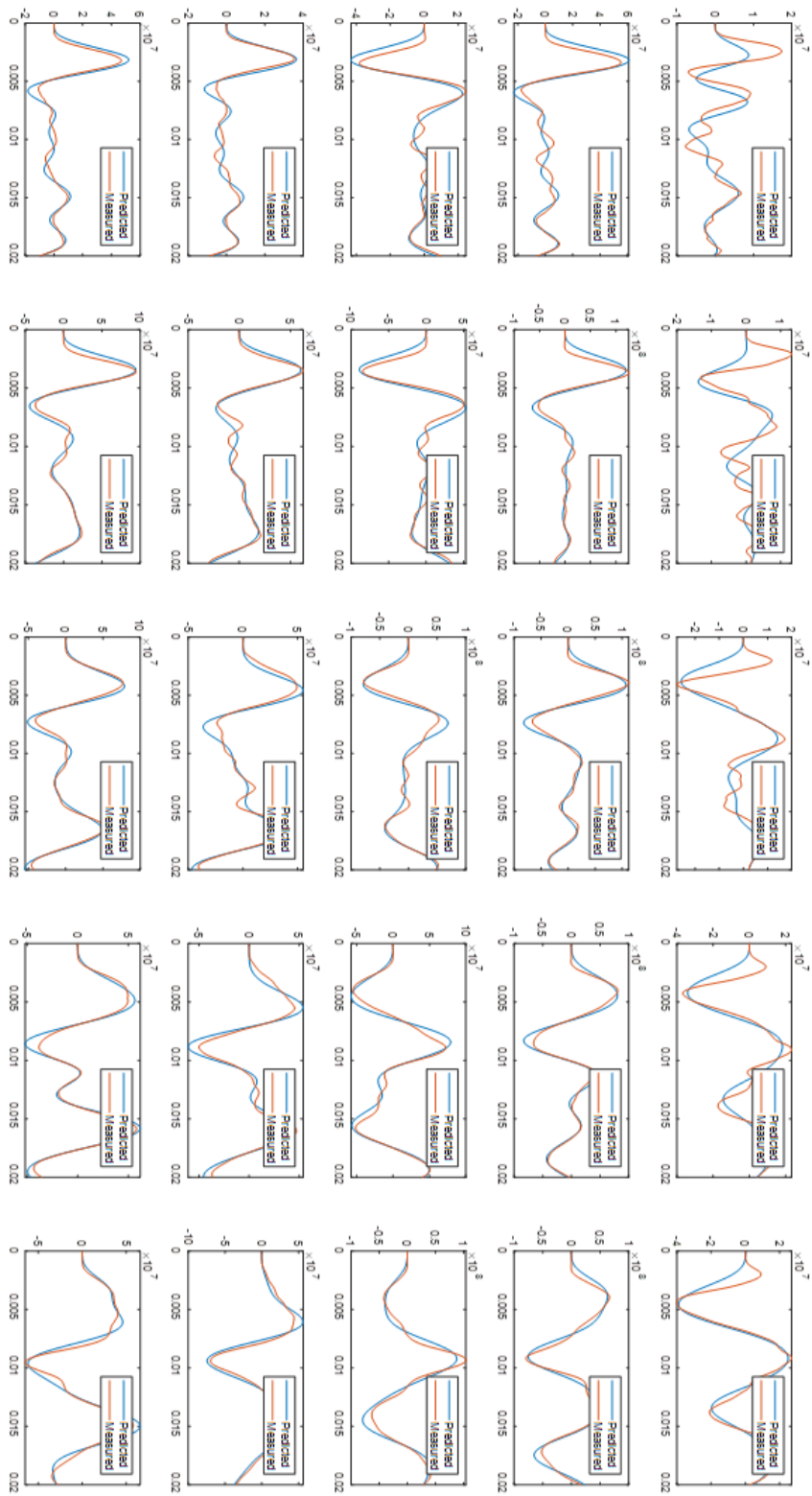

Fig. 77. Comparison of stress responses

4.3.2.2. Prediction of applied load corresponding to measured structural response

In order to predict sloshing pressure from the measured stress response of the supporting structure, the reverse process is required. The relationship between stress response and modal amplitude can be written as in Eq. (33). The modal matrix consists of the stress values of each mode obtained from the modal analysis. The modal amplitude is calculated by multiplying the inverse of the stress modal matrix by the measured stress response (see Eq. (33)).

$$\{\sigma(t)\} \approx \sum_{i=1}^{l} \phi_{s_i} q_i(t) = [\tilde{\phi}_s]\{q(t)\} \Leftrightarrow \{q(t)\} = [\tilde{\phi}_s]^{-1}\{\sigma(t)\} \cdots (33)$$

where,

$\{\sigma(t)\}$: stress response of sloshing pressure

$[\tilde{\phi}_s]$: generalized modal matrix(stress)

The modal amplitude velocity and modal amplitude acceleration can be calculated from the numerical difference of modal amplitude. A central difference foam is adopted for numerical difference, as shown in Eq. (34).

$$\{\dot{q}(t)\} = \frac{\{q(t+\Delta t)\} - \{q(t-\Delta t)\}}{2\Delta t}$$

$$\{\ddot{q}(t)\} = \frac{\{\dot{q}(t+\Delta t)\} - \{\dot{q}(t-\Delta t)\}}{2\Delta t} \cdots (34)$$

where,

$\{\dot{q}(t)\}$: velocity of modal amplitude

$\{\ddot{q}(t)\}$: acceleration of modal amplitude

By substituting the calculated modal amplitude, modal amplitude velocity and modal amplitude acceleration into Eq. (35), the sloshing pressure corresponding to the measured stress response can be predicted.

$$\{F(t)\} = \left(\left[\tilde{\phi}\right]^T\right)^{-1} (\{\ddot{q}(t)\} + \alpha\{\dot{q}(t)\} + [\lambda]\{q(t)\}) \cdots (35)$$

where,

$\left[\tilde{\phi}\right]$: generalized modal matrix(displacement)

When predicting sloshing pressure from measured stress response, the number of measured stress responses is quite small relative to the DOF number of the system. Originally, each column vector composing $\left[\tilde{\phi}_s\right]$ in Eq. (33) has the same number of elements as the total DOF number of the system. $\{\sigma(t)\}$ represents the stress response obtained in all DOF of the system. However, in an LNG CCS, the stress response of the supporting structure is measured only at 25 points. This means that the $\left[\tilde{\phi}_{ps}\right]$, which is a 25 by 20 matrix, is obtained from the values of the DOF for which the stress response is measured in $\left[\tilde{\phi}_s\right]$. $\left[\tilde{\phi}_{ps}\right]$ can be expressed as Eq. (36). Using $\left[\tilde{\phi}_{ps}\right]$, the modal amplitude corresponding to the measured stress response can be estimated (see Eq. (36)).

$$\left[\tilde{\phi}_{ps}\right] = \begin{bmatrix} \sigma_{1,1} & \cdots & \sigma_{1,20} \\ \vdots & \ddots & \vdots \\ \sigma_{25,1} & \cdots & \sigma_{25,20} \end{bmatrix}$$

$$\{q(t)\} = \left[\tilde{\phi}_{ps}\right]^{-1}\{\sigma(t)\} \cdots (36)$$

where,

$\left[\tilde{\phi}_{ps}\right]$: partial generalized modal matrix($stress$)

When a partial generalized modal matrix is used instead of a generalized modal matrix, the independence between column vectors constituting the modal matrix cannot be sufficiently secured. The higher the correlation between column vectors, the higher the instability in the process of performing pseudo inverse of the partial generalized modal matrix. This leads to an increase in the error of the calculated modal amplitude. If the modal amplitude is not calculated properly, the accuracy of the predicted sloshing pressure and hot spot stress response will be lowered.

In order to increase the accuracy of modal amplitude estimation, an additional mode selection process was introduced. By removing highly correlated column vectors in the partial generalized modal matrix, the stability of calculation of $[\tilde{\phi}_{ps}]^{-1}$ could be increased. Each mode has a different modal effective mass fraction. Additional mode selection process is carried out based on the mode with the highest model effective mass fraction (mode no.3) and the lowest mode (mode no.1). Among the remaining modes, the modes with low correlation (high priority) are sequentially determined. The modes with low priority are removed sequentially until a stable result is

obtained. From this, a total of 6 modes (mode nos.2,10,11,12,16 and 20) are removed. The calculation of modal amplitude using finally selected modes can be expressed as in Eq. (37).

$$\{q(t)\} = \left[\tilde{\phi}'_{ps}\right]^{-1}\{\sigma(t)\} \cdots (37)$$

$$\left[\tilde{\phi}_{ps}{}'\right] = \begin{bmatrix} \sigma_{1,1} & \cdots & \sigma_{1,\gamma} \\ \vdots & \ddots & \vdots \\ \sigma_{25,1} & \cdots & \sigma_{25,\gamma} \end{bmatrix}$$

where,

γ: the number of modes to consider

$\left[\tilde{\phi}_{ps}{}'\right]$: partial generalized modal matrix with additional mode selection (stress)

Under the same loading condition as shown in Fig. 73, prediction of sloshing pressure was performed from the measured stress response. The in-plane stresses measured at 25 locations are plotted in Fig. 77. The modal amplitude calculated using Eq. (37) is plotted in Fig. 78. There, 'forward' represents the modal amplitude result obtained using the Newmark-beta method when the sloshing pressure was given. The modal amplitude calculated in the forward process matched well with that estimated from the measured 25 stress responses.

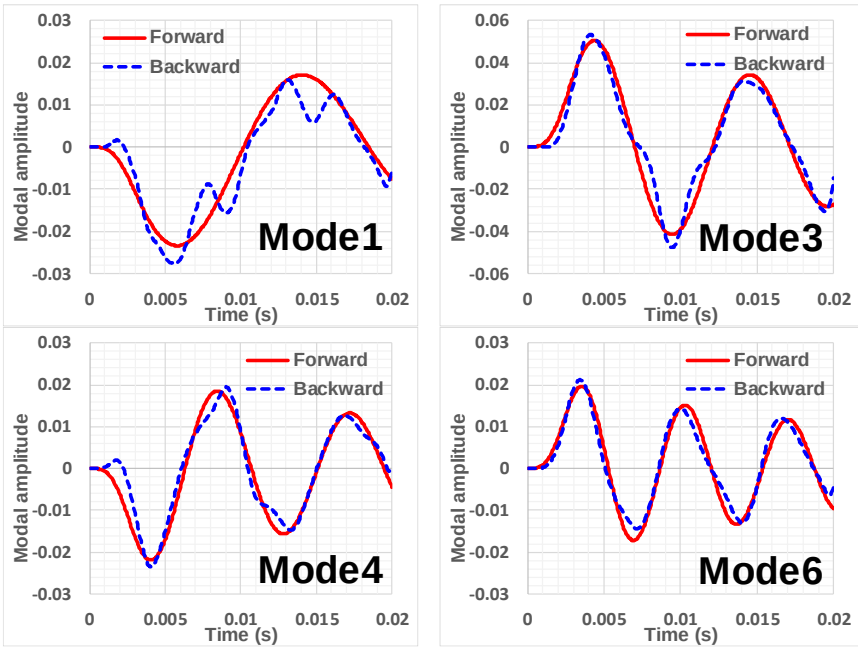

Fig. 78. Calculated modal amplitude ($\{q(t)\}$)

Eq. (34) is utilized to calculate the modal amplitude velocity and modal amplitude acceleration corresponding to the modal amplitude. Figures 79 and 80 illustrate the calculated modal amplitude velocity and modal amplitude acceleration results. It can be seen that the effect of some noise present in the modal amplitude is amplified in the process of numerical difference. Thus, there is a large difference between the sloshing pressure predicted from Eq. (35) and the actual applied pressure (see Fig. 81).

Various smoothing techniques are widely used to reduce the instability due to numerical difference. Since sloshing pressure manifests in various types, providing specific guidance on a smoothing technique for sloshing pressure prediction is not realistic. Thus, the mode superposition method has limitations for prediction

of sloshing pressure.

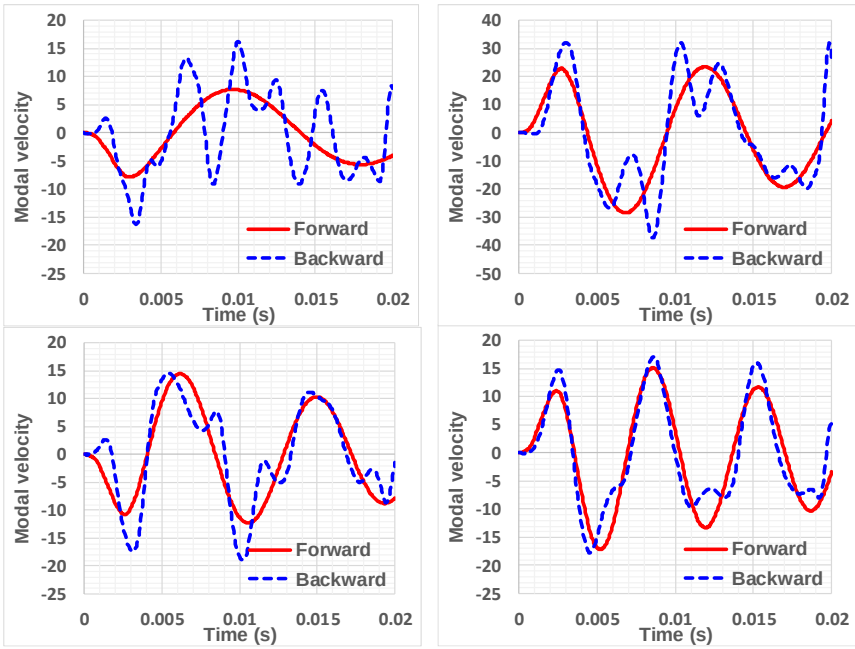

Fig. 79. Calculated velocity of modal amplitude ($\{\dot{q}(t)\}$)

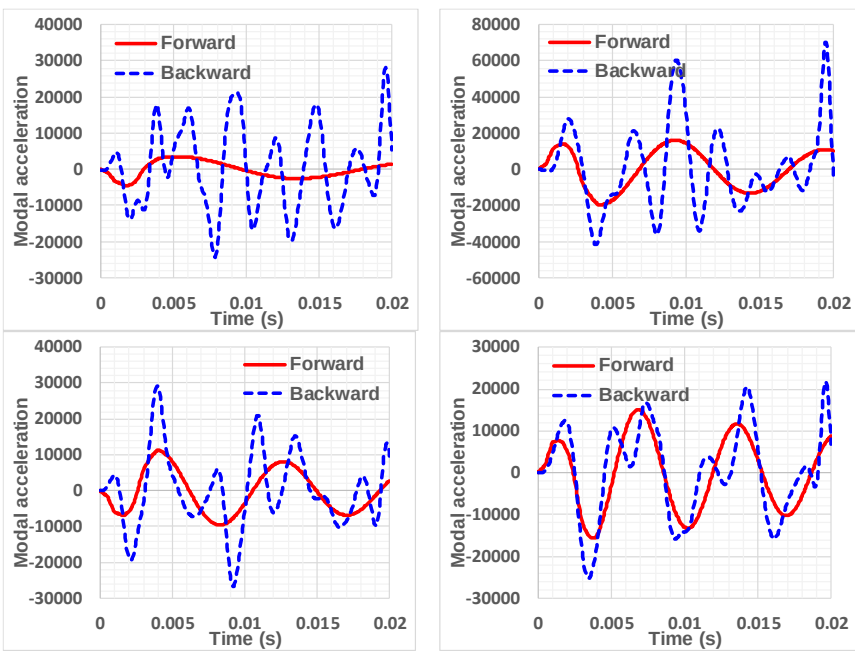

Fig. 80. Calculated acceleration of modal amplitude ($\{\ddot{q}(t)\}$)

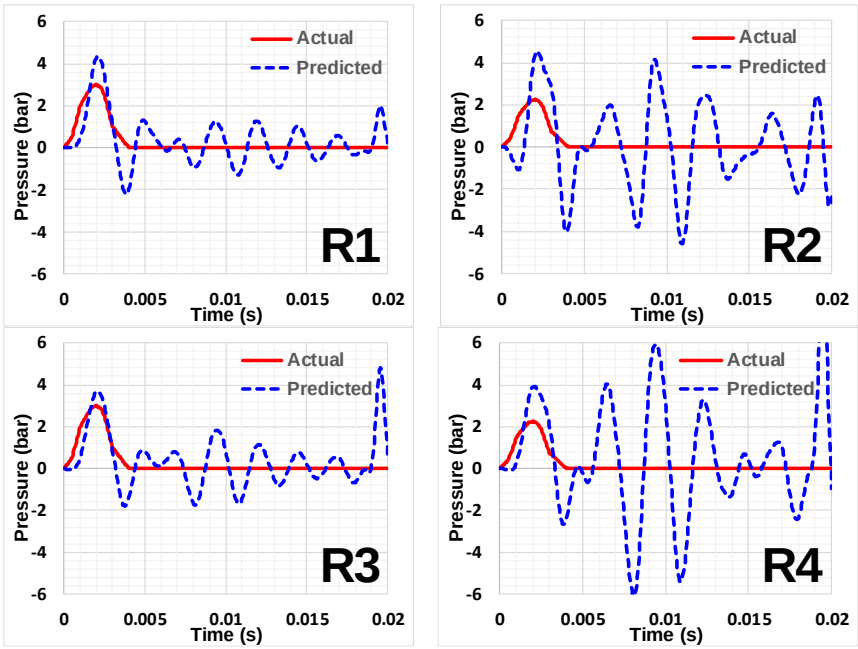

Fig. 81. Predicted sloshing pressure using mode superposition method

4.3.3. Prediction of hot spot stress response

As shown in Fig. 78, prediction of modal amplitude was performed appropriately. The stress response at the hot spot was calculated from the modal amplitude without any numerical difference process. The relationship between modal amplitude and hot spot stress response can be expressed as Eq. (38). A matrix $[\hat{\phi}_{hs}]$ representing the relationship between the two values was obtained from the modal analysis. The stress at the hot spot generated in each mode constitutes the matrix $[\hat{\phi}_{hs}]$. The first column of $[\hat{\phi}_{hs}]$ corresponds to the hot spot stress response obtained in the 1st model. In the present study, 7 hot spot stress responses were chosen for a total of 4 locations, as shown in Fig. 69. $\sigma_{1,1}$ is the z−stress of PUF in the

1st mode, and $\sigma_{p,1} = \sigma_{7,1}$ is the zx-stress of plywood2 in the 1st mode.

$$\{\sigma_{hs}(t)\} = [\hat{\phi}_{hs}]\{q(t)\} \cdots (38)$$

$$[\hat{\phi}_{hs}] = \begin{bmatrix} \sigma_{1,1} & \cdots & \sigma_{1,\gamma} \\ \vdots & \ddots & \vdots \\ \sigma_{p,1} & \cdots & \sigma_{p,\gamma} \end{bmatrix}$$

where,

p: *The number of predicted hot spot stress response*

γ: the number of modes to consider

$[\hat{\phi}_{hs}]$: generalized modal matrix(at the hot spots)

The stress response prediction process using the mode superposition method can be summarized in two steps (see Fig. 82).

- Calculation of modal amplitude from the measured stress
- Calculation of hot spot stress from the modal amplitude

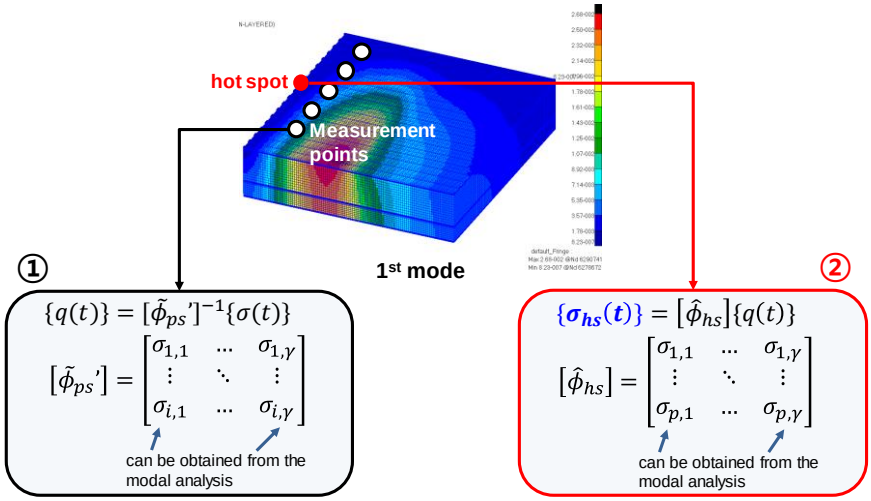

Fig. 82. Prediction of stress response using mode superposition method

There are no constraints on loading conditions in these processes. Unlike the impulse/space superposition approach, the effect of continuous impact also can be considered. Nevertheless, inevitable errors appear during mode selection and mode truncation.

4.4. Application of Suggested Method

Tables 10 and 11 compare the impulse/space superposition method and the mode superposition method for sloshing pressure prediction and stress response prediction, respectively. In Section 3.2, it was confirmed that prediction of sloshing pressure using the mode superposition method is difficult due to the instability inherent in the numerical difference of modal amplitude. By applying suitable mode selection and mode truncation, hot spot stress response using the mode superposition method becomes possible. For prediction of the hot spot stress response of an LNG CCS, each of the two approaches has advantages and disadvantages.

To verify the validity of the proposed methods, analysis for uniform/discrete pressure distribution and FSI analysis were performed using the finite element method. The sloshing pressure was predicted from the stress responses at the measurement points calculated in the analysis for uniform/discrete pressure distribution, and this was compared with the actual applied pressure. From the predicted sloshing pressure, the hot spot stress response was estimated using the impulse/space superposition method. A comparison of the estimated hot spot stress response with the

response directly calculated from analysis for uniform/discrete pressure distribution was carried out.

In the FSI analysis, applied pressure was generated from the impact between the water block and the membrane of the LNG CCS. A continuous pressure distribution appeared on the membrane, due to the influence of fluid motion. The generated sloshing pressure and the sloshing pressure predicted from the measured stress data were compared. In order to predict the hot spot stress response, not only the impulse/space superposition method but also the mode superposition method was applied. The stress responses predicted through the two approaches were compared with the stress response obtained from the FSI analysis.

Table 10. Comparison of two approaches

(prediction of sloshing pressure)

Approach	Given	Data used to calculate $\{\boldsymbol{P}(t)\}$	Sources of error in uniform & discrete pressure distribution	Sources of error for continuous pressure distribution (FSI analysis)
Impulse/space superposition	Measured stress responses $\{\sigma(t)\}$	Stress histories for unit impulse pressure $[\delta(t)]$	No error	Assumption of uniform pressure within each zone
Mode superposition		Predicted modal amplitudes and derivatives $\{q(t)\}$, $\{\dot{q}(t)\}$, $\{\ddot{q}(t)\}$	▪ Calculation of $[\tilde{\phi}_{ps}{}']^{-1}$ ▪ Calculation of $\{\dot{q}(t)\}$ and $\{\ddot{q}(t)\}$ (large instability)	

Table 11. Comparison of two approaches

(prediction of stress in CCS)

Approach	Given	Data used to calculate $\{\sigma_{hs}(t)\}$	Sources of error in uniform & discrete pressure distribution	Sources of error for continuous pressure distribution (FSI analysis)
Impulse/space superposition	Measured stress responses $\{\sigma(t)\}$	Predicted sloshing pressures $\{P(t)\}$	No error	Assumption of uniform pressure within each zone
Mode superposition		Predicted modal amplitudes $\{q(t)\}$	Calculation of $[\tilde{\phi}_{ps}']^{-1}$	

4.4.1. Application: analysis for uniform/discrete pressure distribution

A total of 6 analysis cases were generated as shown in Fig. 83. Various rising times were selected in order to consider both the dynamic loading condition and the quasi-static loading condition. In Case3, the time at which pressure was applied differed between R1 and R2. The effect of the pressure occurrence time on the prediction of sloshing pressure could be checked. The same pressure was applied to each of R1, R2, R3 and R4. Thus, there was no effect of sloshing pressure change within each region.

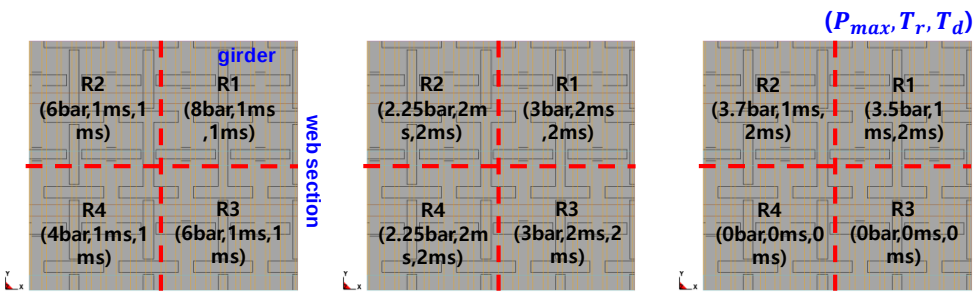

Case1 (T_r=1ms) Case2 (T_r=2ms) Case3 (T_r=1ms)

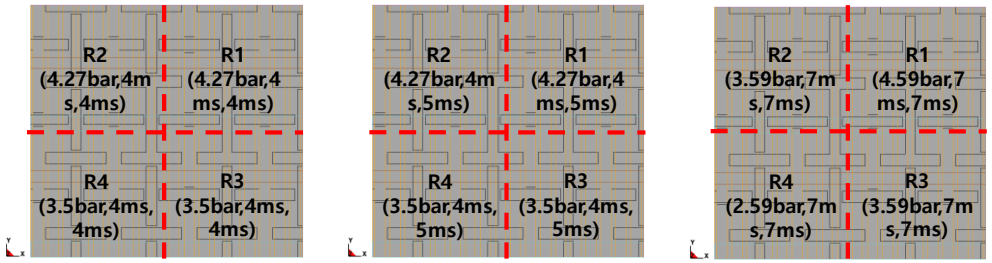

Case4 (T_r=4ms) Case5 (T_r=4ms) Case6 (T_r=7ms)

Fig. 83. Selected load cases for analysis

Figure 84 shows a schematic of the analysis for Case5. After applying the selected pressure to the membrane(R1~R4), the in-plane stress was calculated at the 25 measurement points on the supporting structure. In this way, the sloshing pressure was predicted.

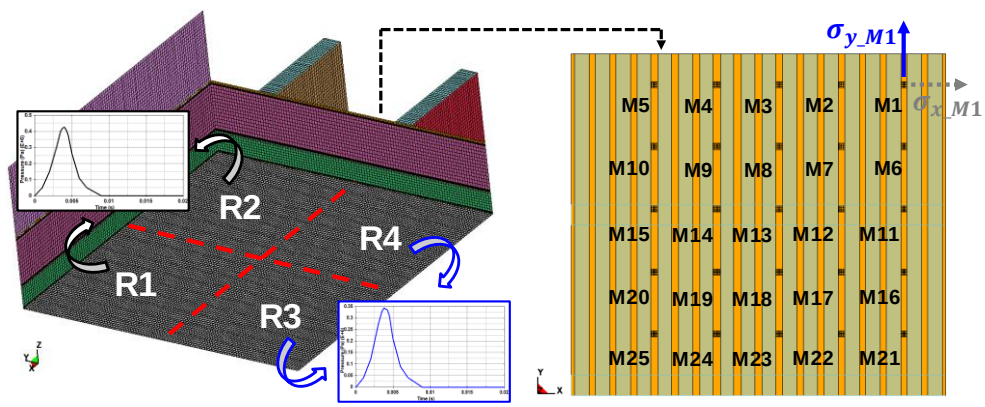

Fig. 84. Pressure application regions and stress measurement locations

The sloshing pressure prediction results for a total of 6 selected cases are illustrated in Figs. 85 to 90. In all of the cases, peak pressure, rising time and pressure profile were predicted

appropriately. Looking at the result of Case1, where the rising time of sloshing pressure was 1ms, the resolution for the peak region was low. The amplitude of sloshing pressure was calculated at the intervals of the rising time of unit pressure ($\Delta t = 0.5ms$). If the rising time of unit pressure is adjusted in detail, the accuracy of prediction will be improved.

Due to the nature of the method of inversely predicting sloshing pressure from measurement data, any slight noise in the measurement data has a significant effect on the prediction results. The stress response of the supporting structure as calculated from the numerical analysis contained numerical noise. Because of this noise, in cases4 and6, the smoothness of the predicted sloshing pressure profile was relatively low. A slight underestimation of peak pressure also was observed.

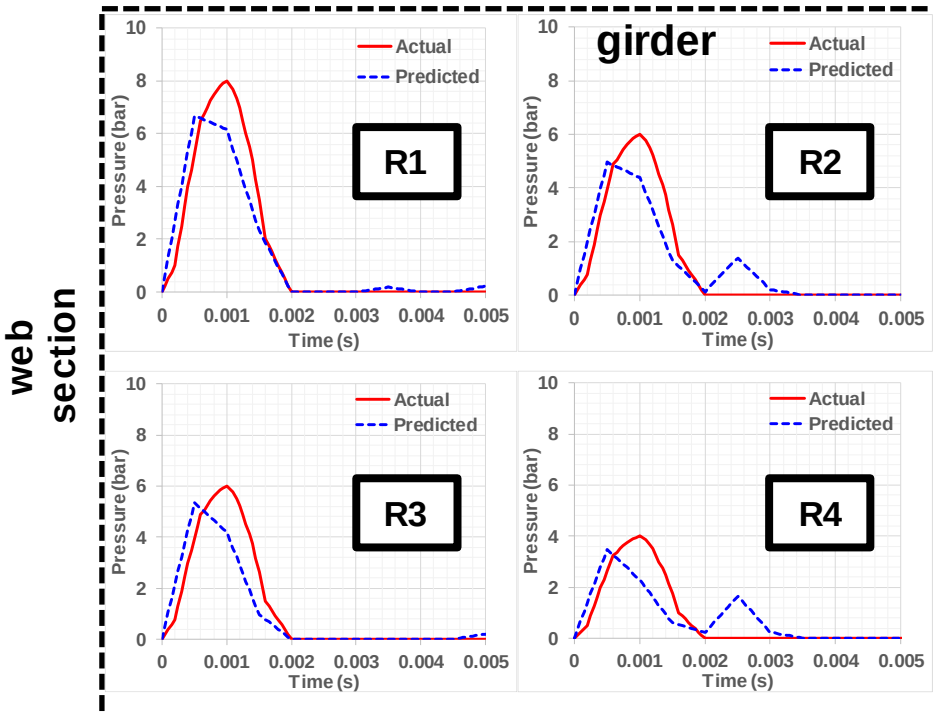

Fig. 85. Predicted sloshing pressure(Case1)

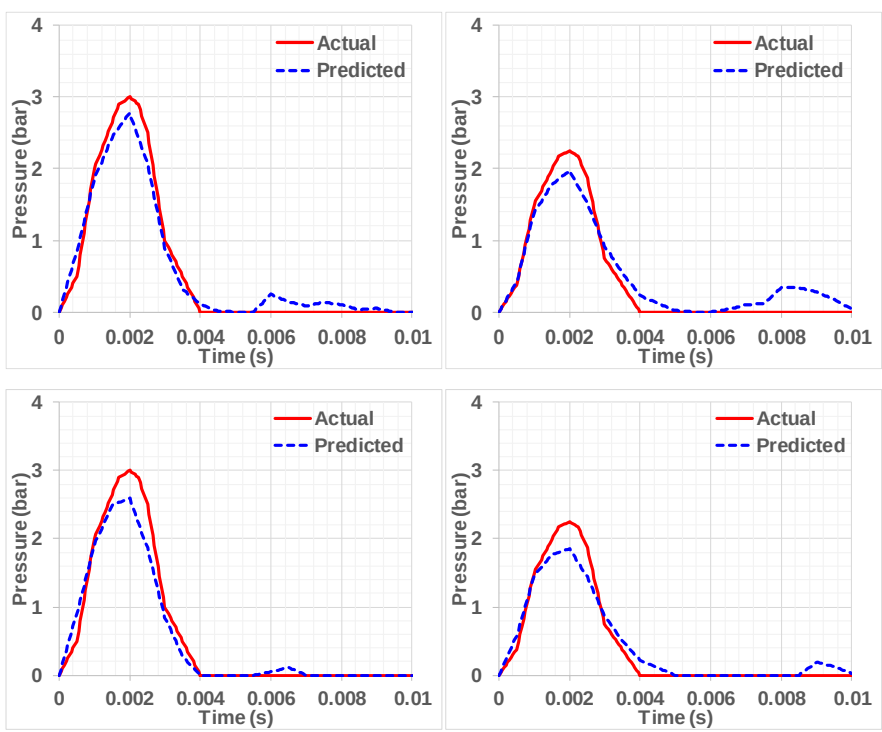

Fig. 86. Predicted sloshing pressure(Case2)

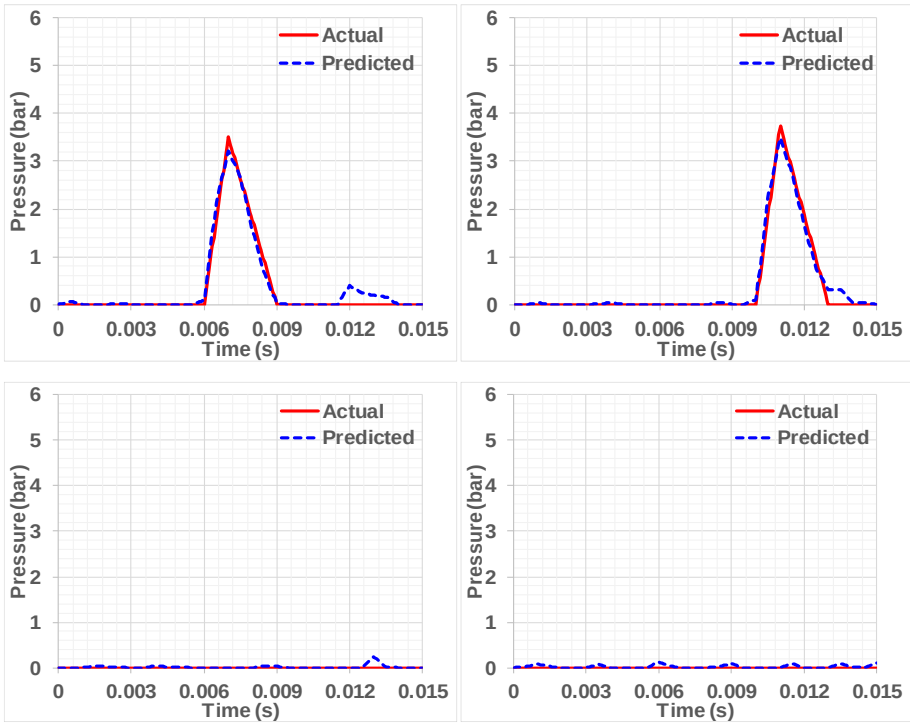

Fig. 87. Predicted sloshing pressure (Case3)

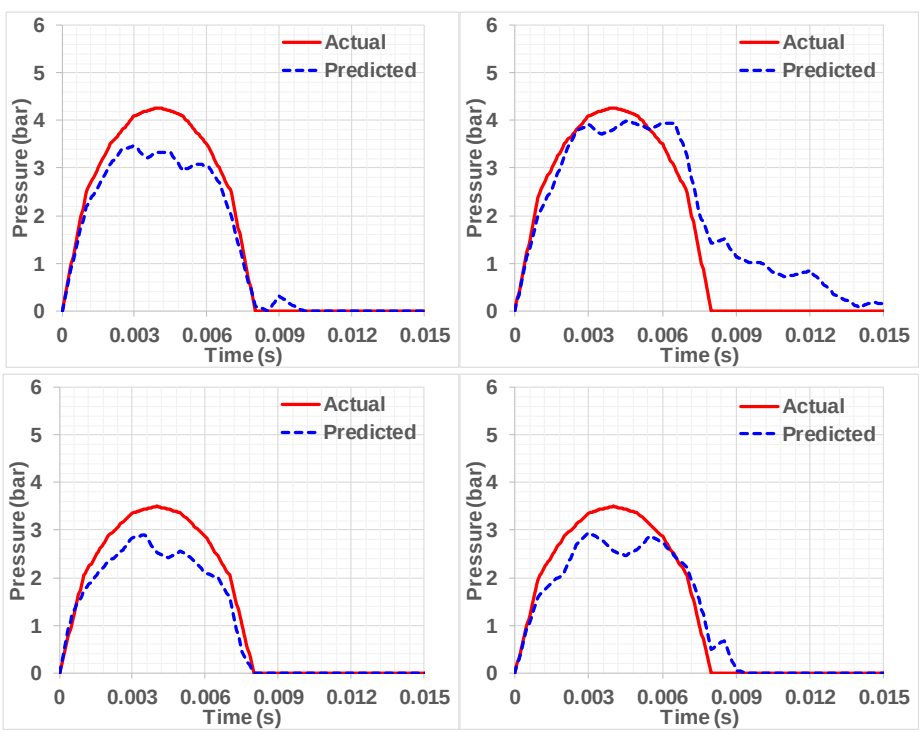

Fig. 88. Predicted sloshing pressure (Case4)

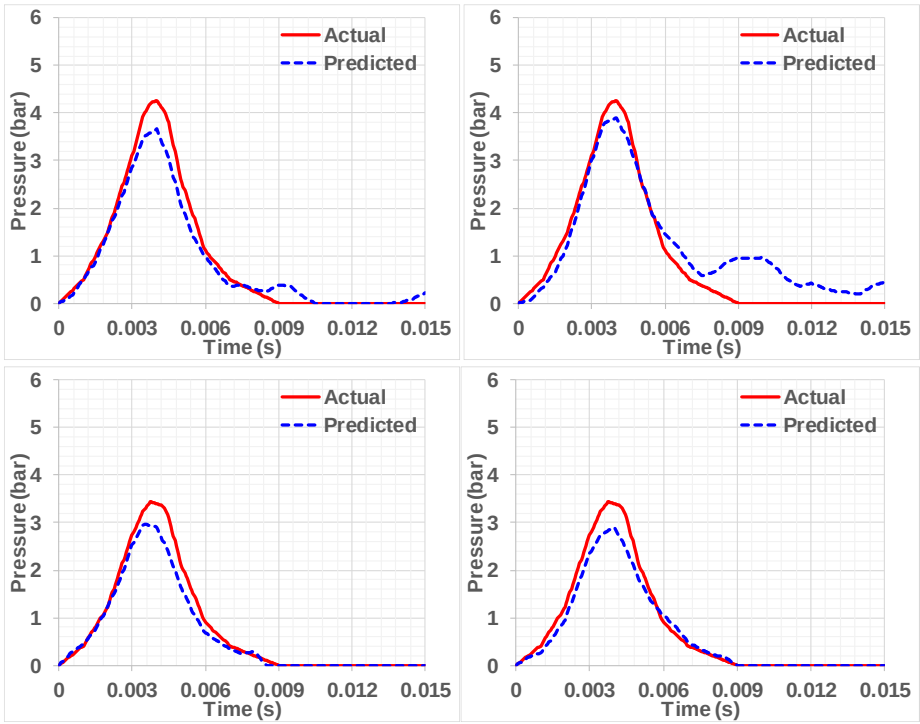

Fig. 89. Predicted sloshing pressure (Case5)

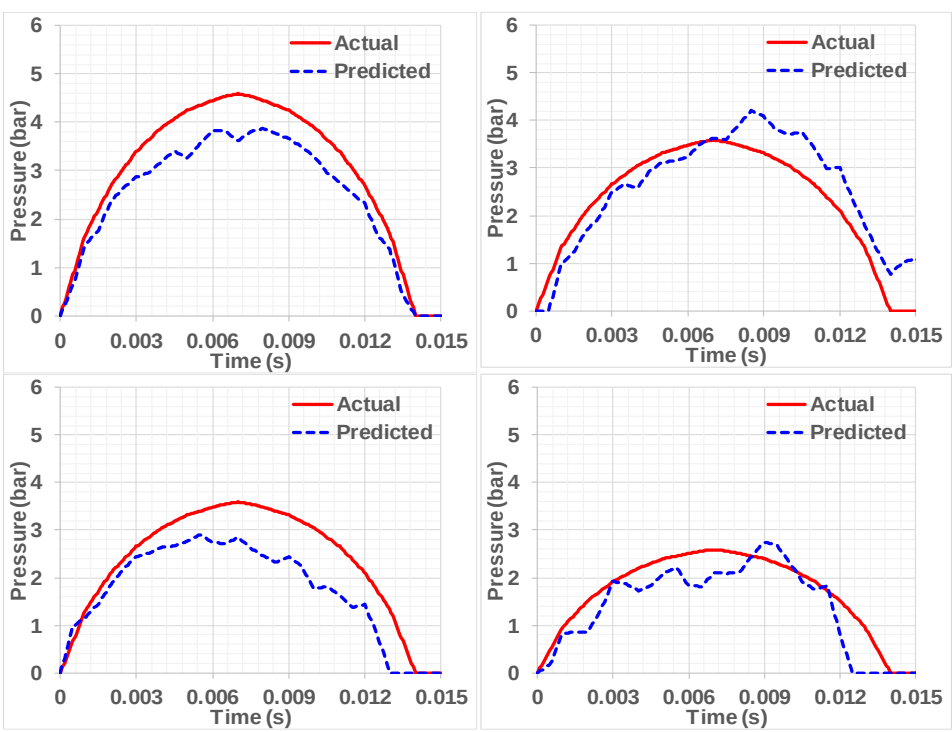

Fig. 90. Predicted sloshing pressure (Case6)

Figure 91 plots the predicted hot spot stress response results for Case2. The impulse/space superposition method was used to calculate the hot spot stress response. In the cases for uniform/discrete pressure distribution, the effect of pressure change within the regions of R1~R4 did not arise. For this reason, the hot spot stress responses predicted through the impulse/space superposition method were in good agreement with the results calculated from the numerical analysis. For both vertical crushing and shear failure, the first peak as well as the overall time history were accurately predicted. The stress response prediction was done properly in all of the other cases. This means that effective monitoring for fatigue failure can be achieved from the predicted stress response.

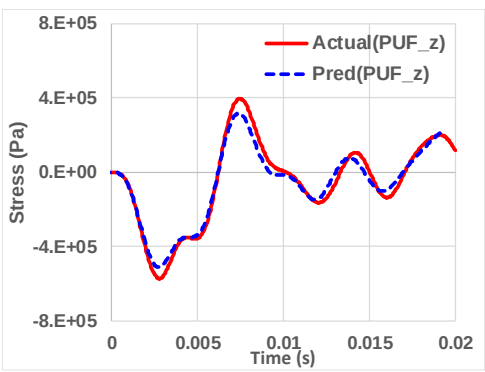

Vertical crushing(PUF)

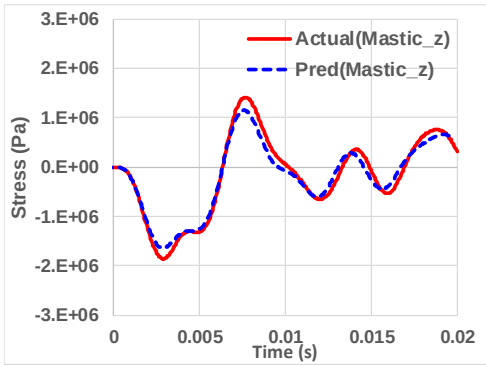

Vertical crushing(Mastic)

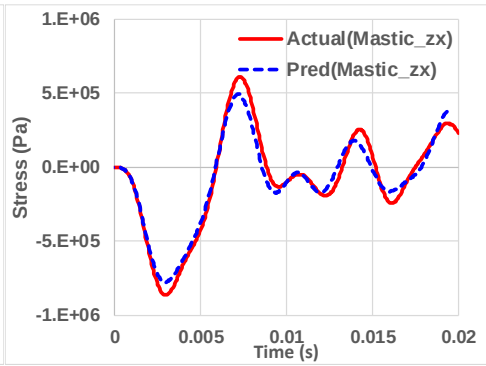

Shear failure(Mastic)

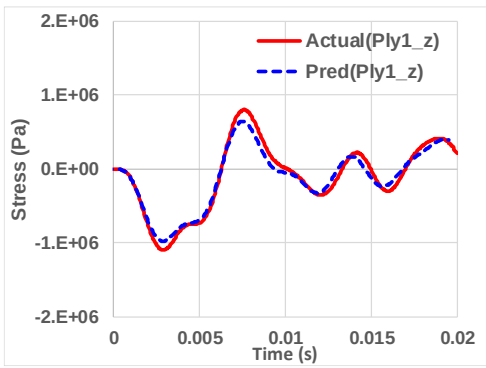

Vertical crushing(Plywood1)

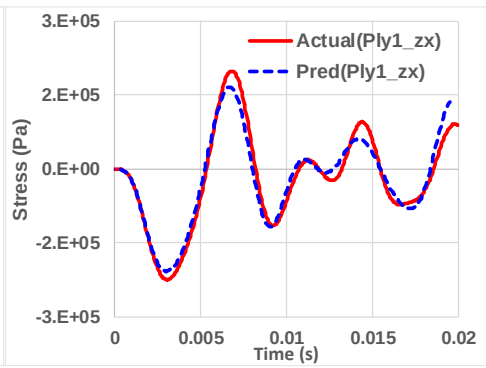

Shear failure(Plywood1)

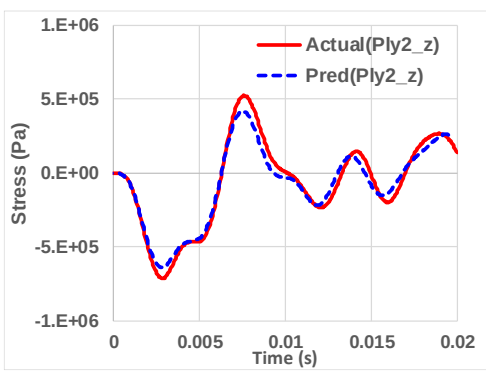

Vertical crushing(Plywood2)

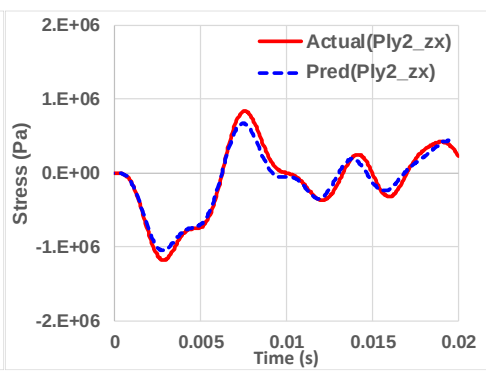

Shear failure(Plywood2)

Fig. 91. Predicted hot spot stress response(Case2)

Figures 92~95 plot the sloshing pressure and stress response prediction results for 6 cases of analysis for uniform/discrete pressure distribution. The results are summarized for peak value and

rising time of pressure and stress. Looking at the pressure prediction results, the peak value and rising time were generally well predicted. In Case6, some overestimation of rising time was observed. As shown in Fig 90, this was the effect of noise generated in the peak region. Rising time was significantly affected by the pressure profile shape of the peak region. The duration time and overall pressure profile were well predicted, and thus, it was judged that the error of rising time was acceptable.

As was the case for sloshing pressure, hot spot stress response was predicted properly in all cases. In the analysis for uniform/discrete pressure distribution, both sloshing pressure and hot spot stress response were well predicted using the impulse/space superposition method, because the same pressure was applied in each region.

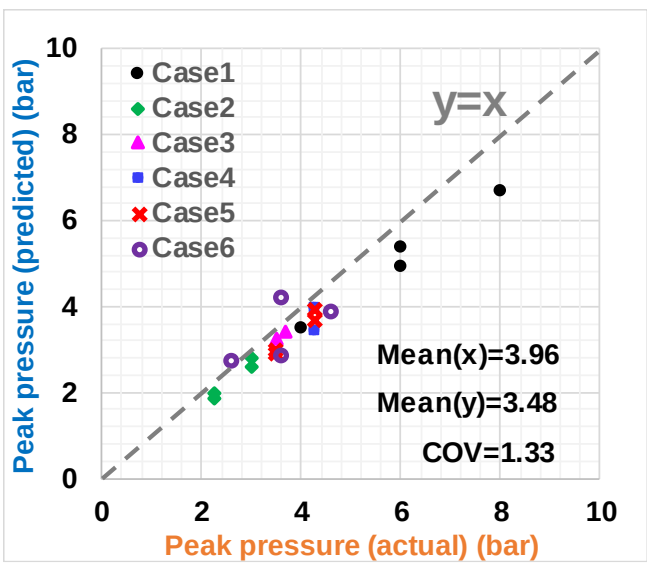

Fig. 92. Predicted sloshing pressure(peak)

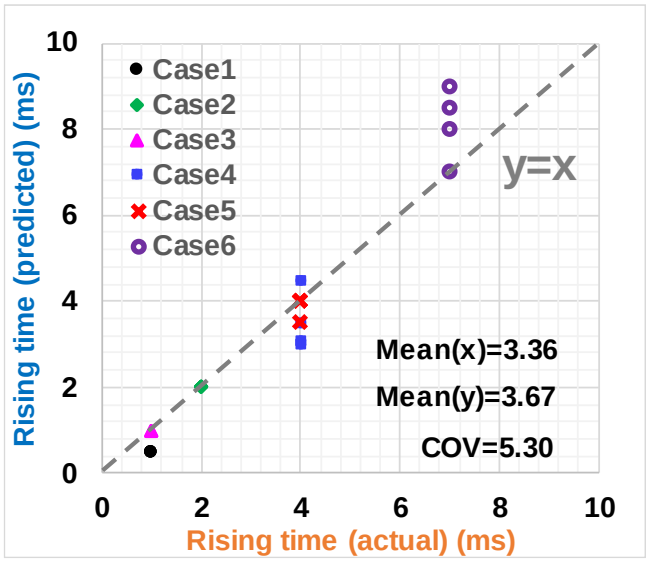

Fig. 93. Predicted sloshing pressure(rising time)

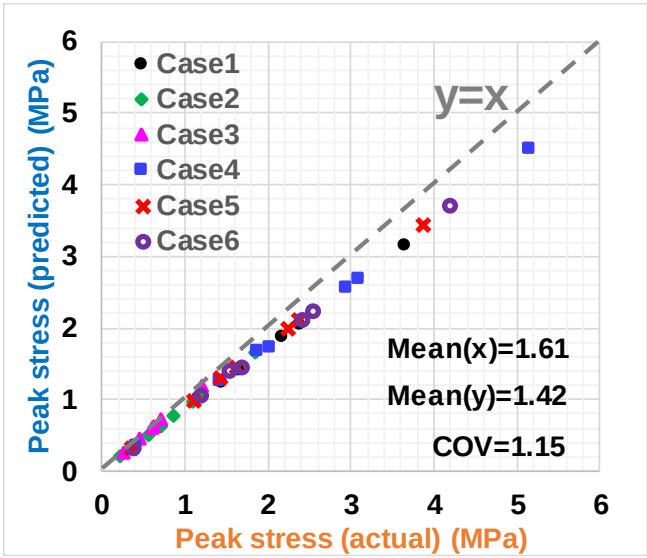

Fig. 94. Predicted stress response(peak)

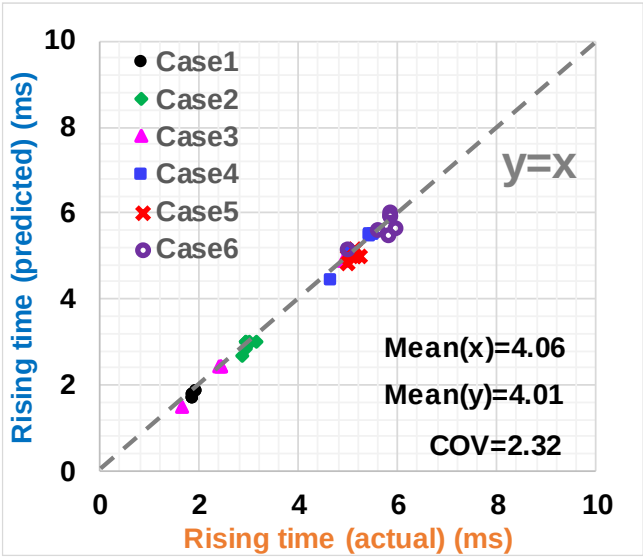

Fig. 95. Predicted stress response(rising time)

4.4.2. Application: analysis for continuous pressure distribution (FSI analysis)

The FSI analysis model was created, as shown in Fig. 96, to understand the impact phenomenon occurring at the upper corner of the LNG tank. The modeling range for the insulation panel and the supporting structure were selected in the same way as in the analysis for uniform/discrete pressure distribution. The inner wall of the LNG tank was assumed to be a rigid plate. The effect of deformation of the inner wall on the impact pressure could be assumed to be not large. The fluid domain was selected to include all the structure domain.

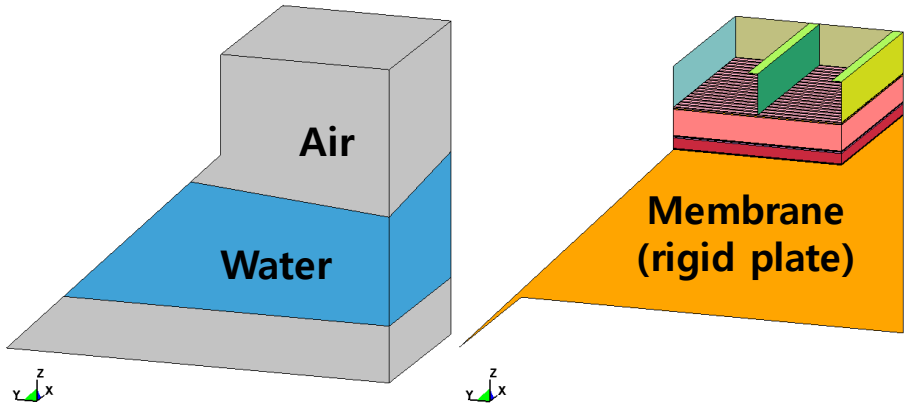

Fluid domain Structure domain

Fig. 96. FSI analysis model

Figure 97 illustrates the dimensions of the FSI analysis model. The angle of the upper corner is 135 degrees, and the upper hopper of the LNG tank is modeled up to 2m. Since the size of the fluid domain is limited, the air volume was inserted under the water block to prevent additional inflow. The impact phenomenon was realized by applying the initial velocity in the vertical direction to the water block.

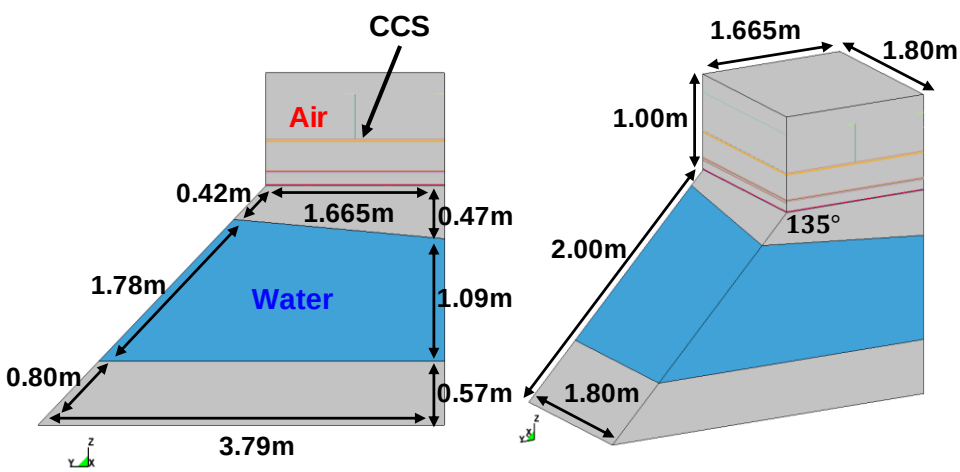

Fig. 97. Model dimensions for FSI analysis

To create various hitting conditions, two deadrise angles of water block were changed as shown in Fig. 98. As the deadrise angle approached 0 degrees, load was simultaneously generated on the membrane of the LNG CCS. On the other hand, when the deadrise angle was increased, impact first occurred in R1 (the corner region), and then the impact area expanded to R4. A continuous pressure distribution over the membrane of LNG CCS appeared.

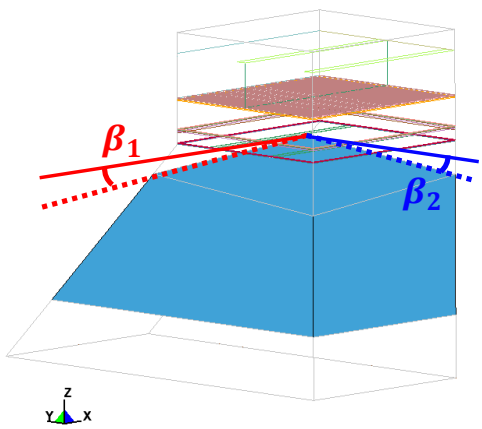

Fig. 98. Two deadrise angles of water block

Figures 99 and 100 show the boundary conditions applied to the FSI analysis. The same boundary conditions as for the analysis for uniform/discrete pressure distribution were applied to the LNG CCS. Symmetric boundary conditions were applied in each direction for the rigid plate representing the inner wall of the LNG tank. In order to maintain the symmetric boundary conditions of the membrane and insulation panel, node equivalence between the rigid plate and the LNG CCS was not carried out. The non-reflecting boundary condition

was applied to the inner surface of the fluid domain (see Fig. 100).

There is a limitation in using a detailed model of an LNG tank corner for FSI analysis, because the influence of fixture structures existing in the corner area is not taken into account. Looking at the corner shape of the Mark III type (Miana et al [74]), the insulation panel was continuously connected. For simplicity, the part bent at 135 degrees was treated as a symmetric boundary condition.

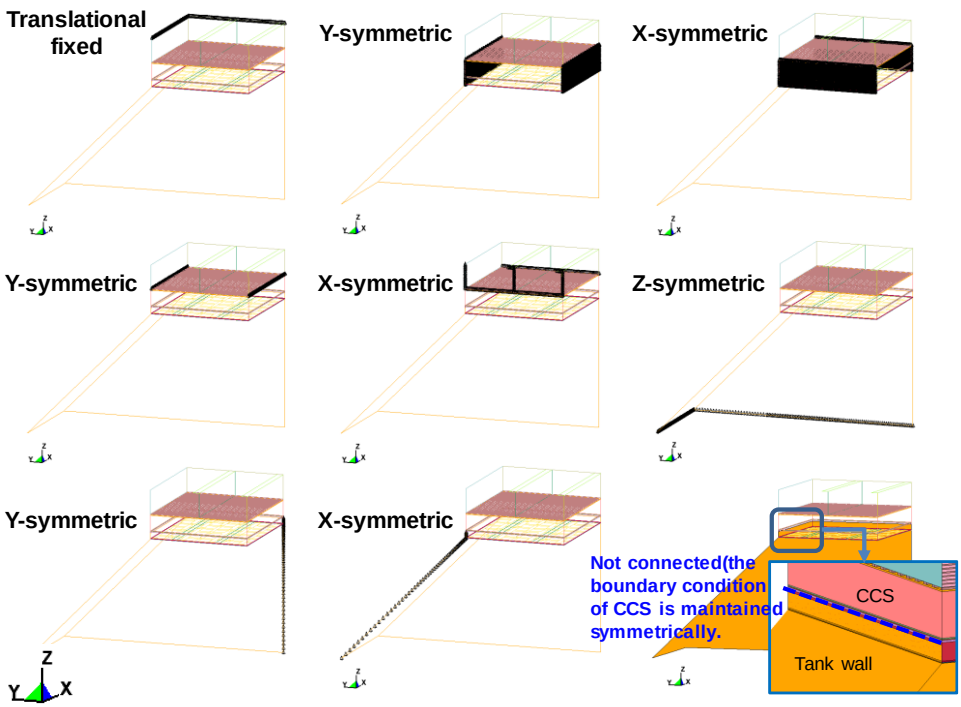

Fig. 99. Boundary conditions for structure domain

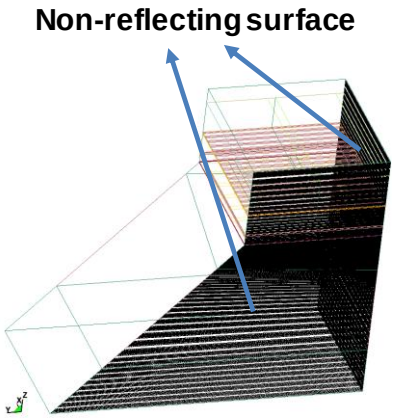

Fig. 100. Boundary condition for fluid domain

As shown in Table 12, a total of 5 FSI analysis cases were generated. Various hitting conditions were realized by changing the deadrise angles and initial velocity of the water block. A value of 1g of gravitational acceleration was applied in all cases.

Figure 101 shows the motion of the water block in Case1. Impact occurs first at the corner, and then the impact area expands. The deadrise angle is close to 0 degrees on the surface of the water block that impacts R4, due to the effect of water spreading. Thus, in R4, an impact similar to the hitting of a water column of 0 deadrise angle appears.

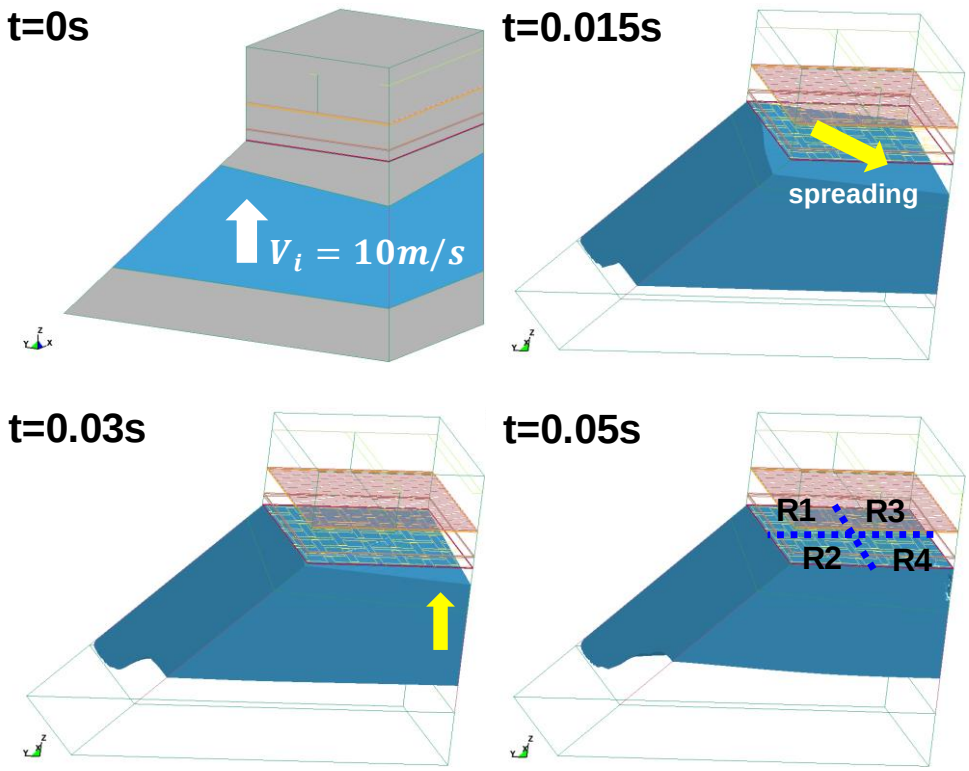

Fig. 101. Fluid motion in FSI analysis(Case1)

The characteristics of fluid motion were reflected in the calculated impact pressure (see Fig. 102). The peak pressure was first observed at R1. Since the two deadrise angles representing the free surface of the water block were the same, almost the same pressure was generated in R2 and R3. In R4, the latest peak pressure was observed.

Additional consideration of an FSI analysis model that can more precisely simulate the sloshing phenomenon occurring in the upper corner is needed. The non-reflecting boundary condition cannot completely replace the effect of domain size. If the fluid domain size applied to FSI analysis is expanded, a more accurate hitting

phenomenon can appear. The effect of the deadrise angle of water block will be properly reflected. Thus, the magnitude of pressure generated in R4 will be reduced.

The range for pressure prediction in the FSI analysis was selected as 50ms, as shown in Fig. 102.

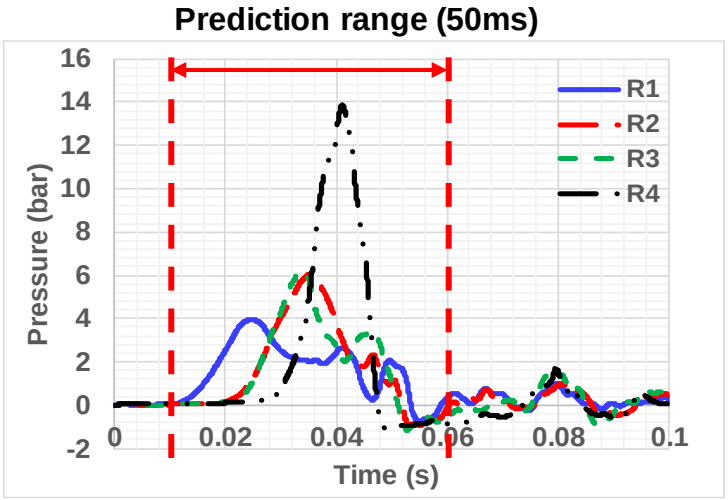

Fig. 102. Calculated impact pressure(Case1)

Table 12. Generated cases for FSI analysis

	FSI case1	FSI case2	FSI case3	FSI case4	FSI case5
Free surface	(5deg, 5deg)	(2deg, 2deg)	(0deg, 0deg)	(2deg, 5deg)	(5deg, 2deg)
Applied velocity	Initial velocity 10m/s	Initial velocity 7m/s	Initial velocity 5m/s	Initial velocity 8m/s	Initial velocity 8m/s
Vertical acceleration	1g	1g	1g	1g	1g
FE model					

The sloshing pressure prediction results for the 5 selected FSI analysis cases are plotted in Figs. 103 to 107, respectively. Unlike the case in the analysis for uniform/discrete pressure distribution, the FSI analysis showed a continuous pressure distribution on the membrane of the LNG CCS. The effect of pressure change in each pressure prediction region generated error in the prediction of sloshing pressure. A slight underestimation appeared in R1 and R2 in cases 1, 2, 4 and 5. However, the magnitude of error in the sloshing pressure prediction was not large. From the results of the analysis for uniform/discrete pressure distribution and FSI analysis, it could be judged that sloshing pressure prediction using the impulse/space superposition method is reasonable.

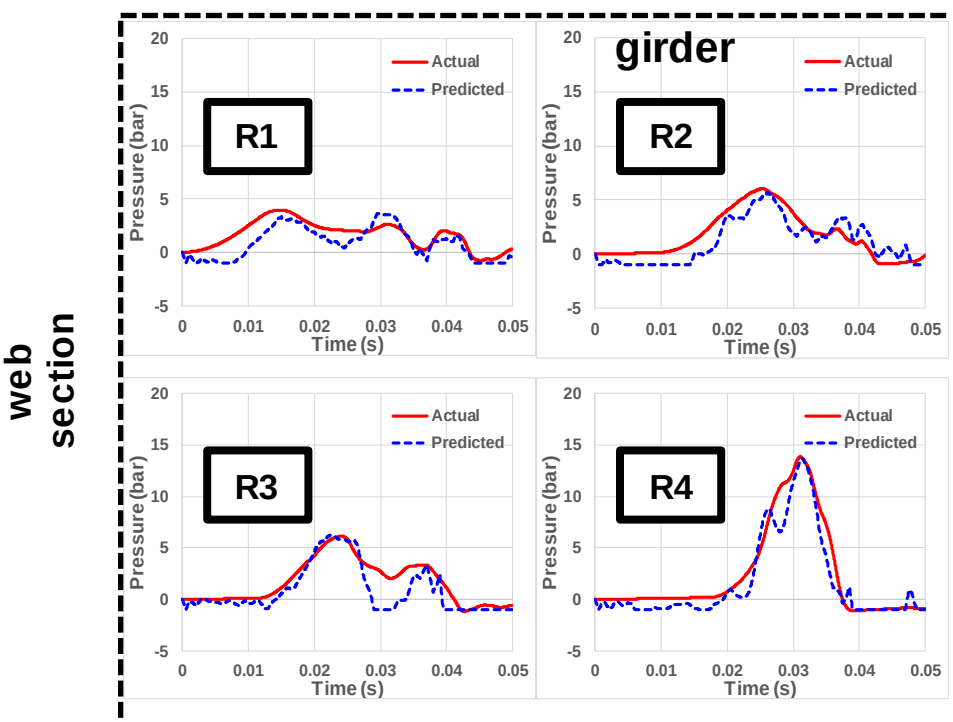

Fig. 103. Predicted sloshing pressure(Case1)

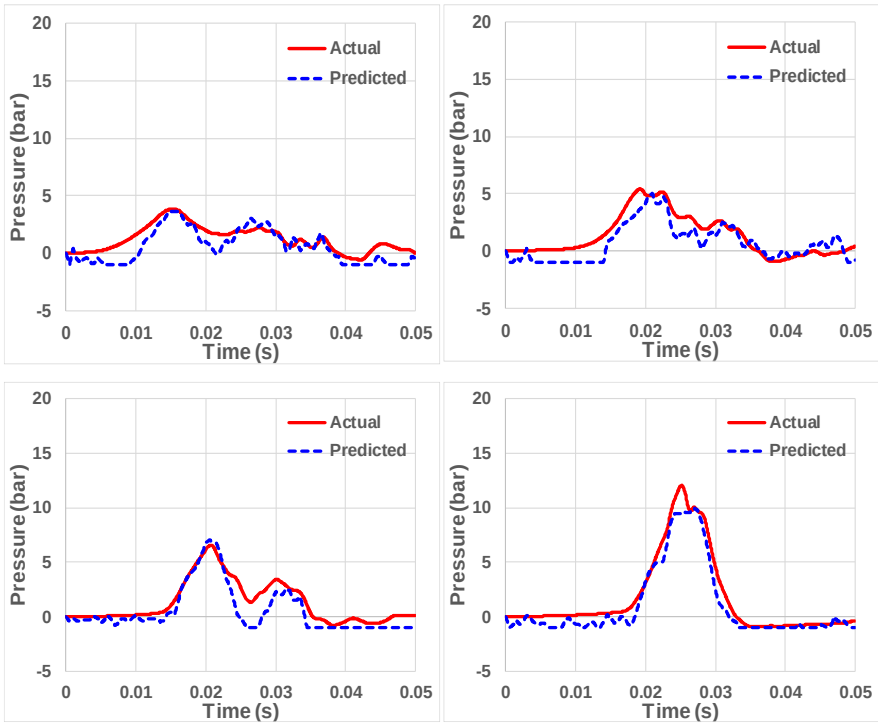

Fig. 104. Predicted sloshing pressure (Case2)

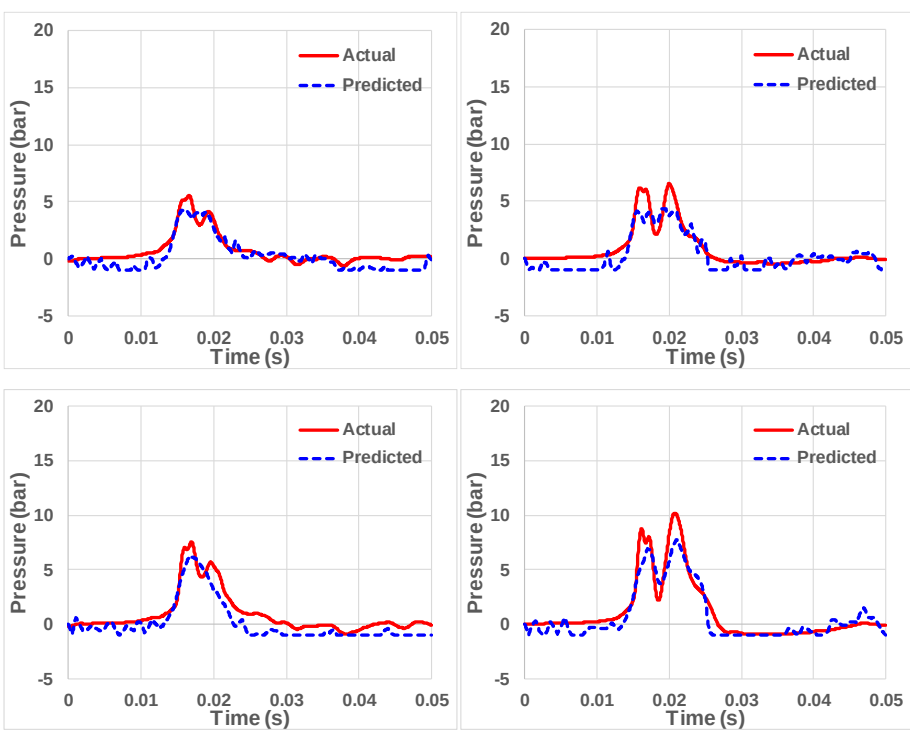

Fig. 105. Predicted sloshing pressure (Case3)

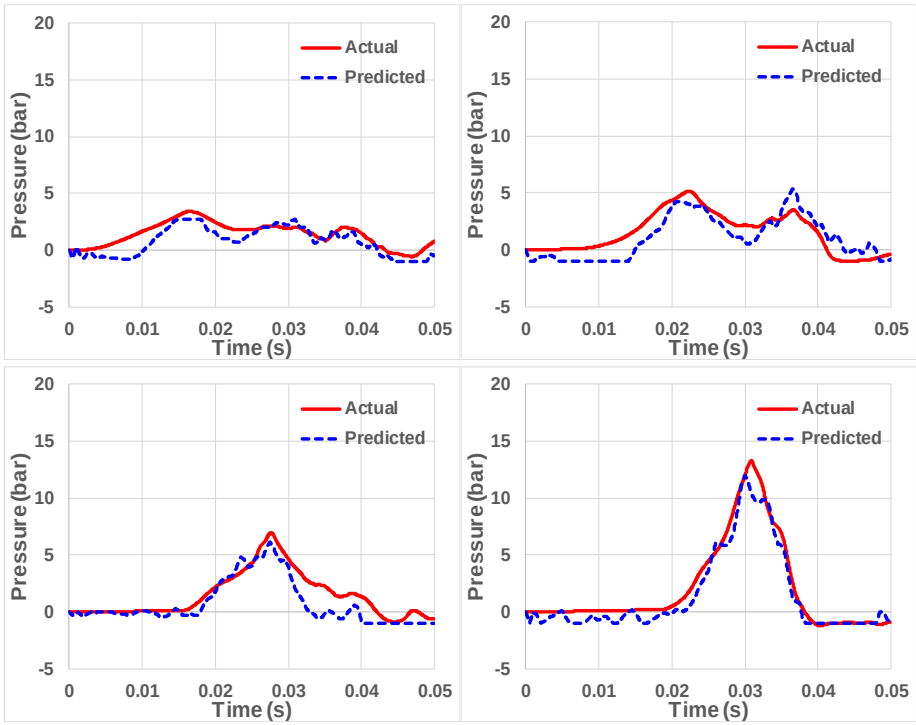

Fig. 106. Predicted sloshing pressure(Case4)

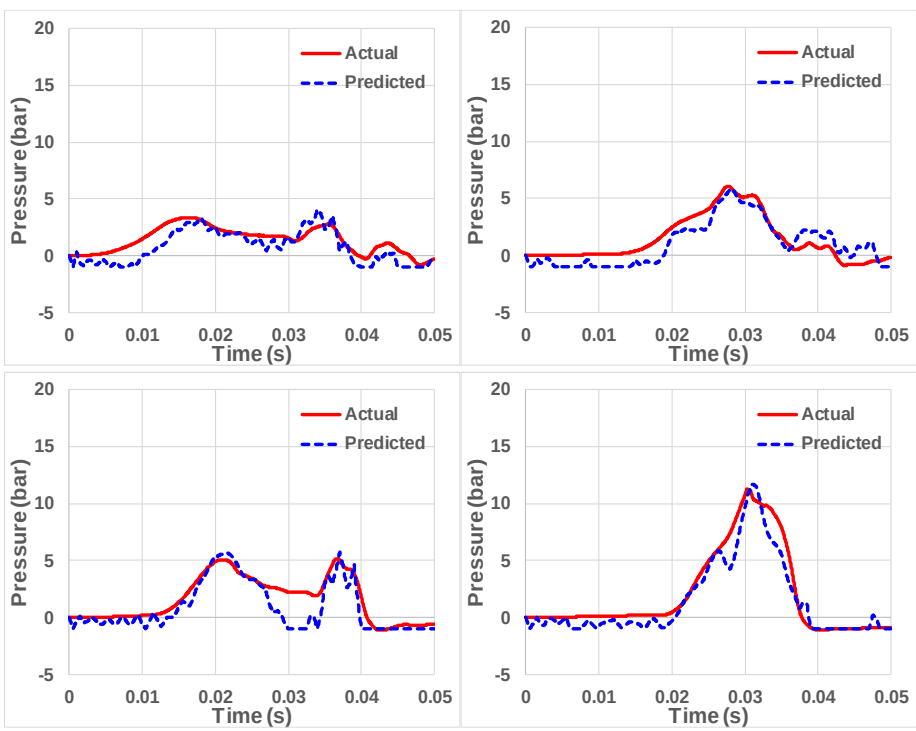

Fig. 107. Predicted sloshing pressure(Case5)

To confirm the effect of continuous impact as it appeared in the FSI analysis, the stress responses at the measurement points were calculated from the predicted pressure. The same process was applied to the analysis for uniform/discrete pressure distribution. As shown in Figs. 108 and 109 respectively, in the analysis for uniform/discrete pressure distribution, the measurement stress data was calculated accurately, whereas in the FSI analysis, some differences were observed. Note that in both figures, the x-axis represents time and the y-axis represents the amplitude of stress.

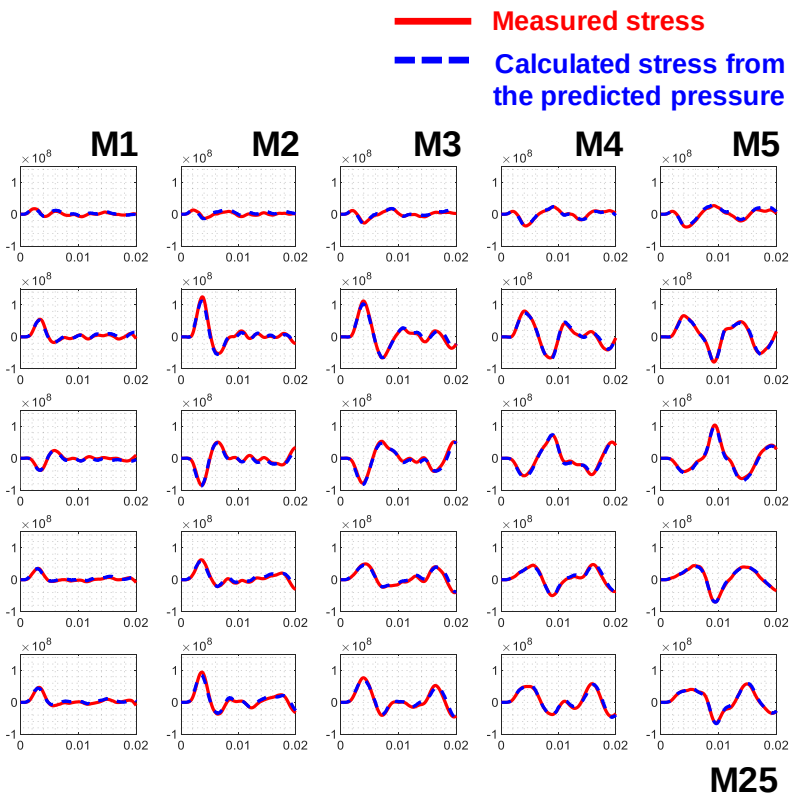

Fig. 108. Accuracy of pressure prediction (Uniform/discrete pressure distribution, Case2)

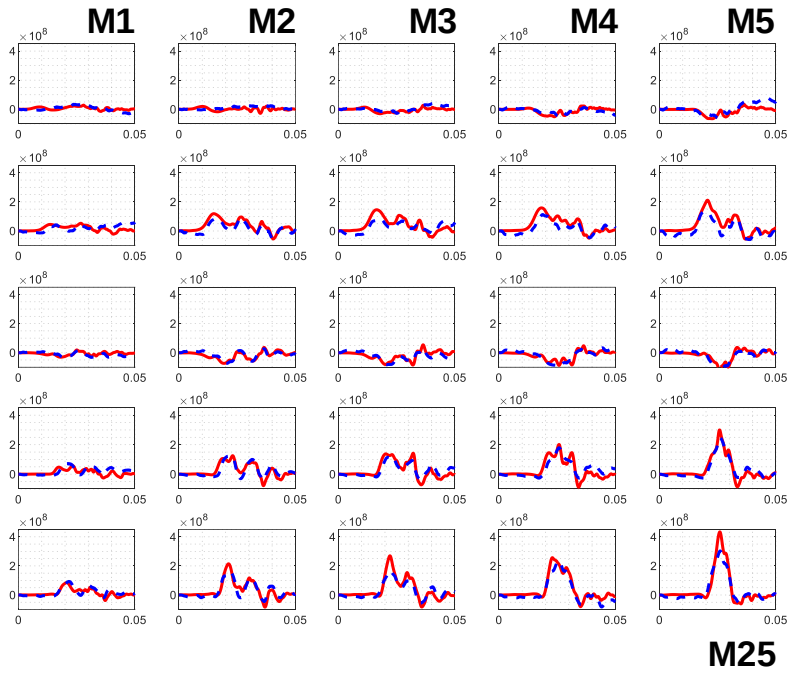

Fig. 109. Accuracy of pressure prediction (Continuous pressure distribution(FSI), Case2)

Both the impulse/space superposition method and the mode superposition method were used to predict hot spot stress response. Figure 110 illustrates these results for the impulse/space superposition method. In Case3, where the impact occurs simultaneously on the membrane, the hot spot stress response is predicted properly. On the other hand, in cases 1, 2, 4 and 5, the accuracy of stress response prediction is relatively low. When predicting sloshing pressure, error occurs near the first peak in R1 and R2, and the effect of this error is maintained in hot spot stress response prediction. Error arises from the continuous impact, which is a fundamental limitation of the impulse/space superposition method.

If the area for prediction of sloshing pressure is set in more detail, the accuracy of the prediction of sloshing pressure and hot spot stress response through the impulse/space superposition method can be improved.

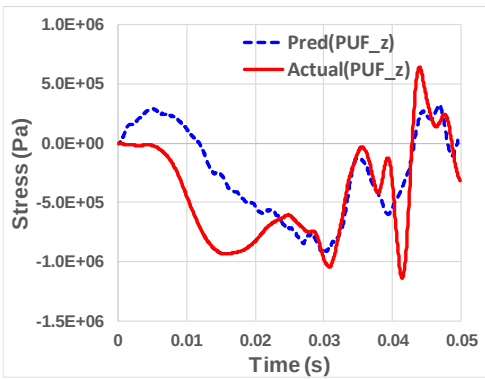

Case1

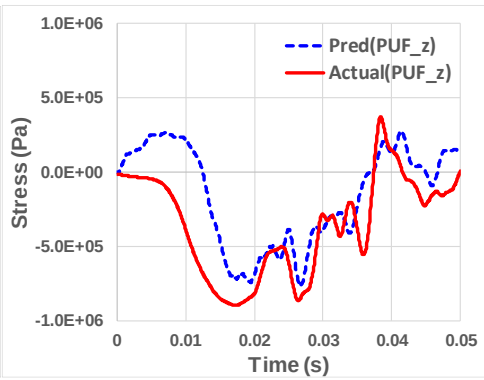

Case2

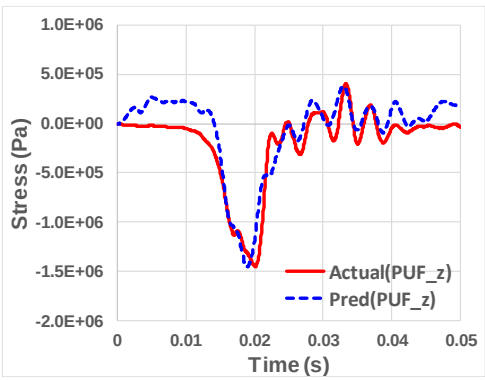

Case3

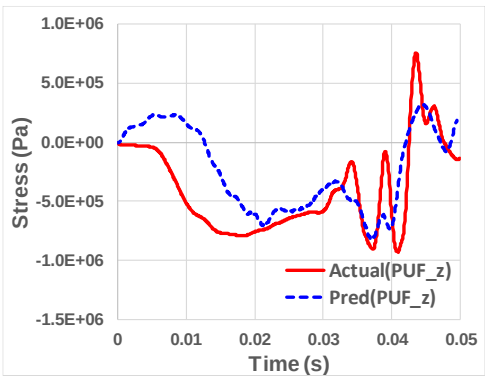

Case4

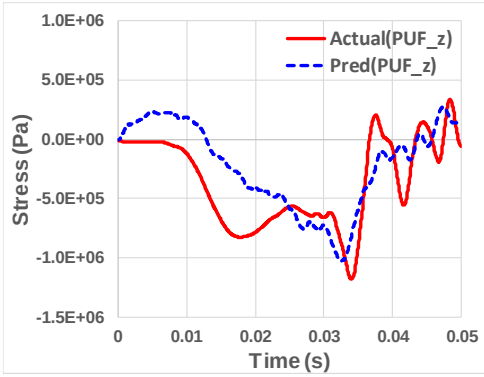

Case5

Fig. 110. Predicted stress response(PUF σ_z) using impulse/space superposition method

Figure 111 plots the results for prediction of hot spot stress response by the mode superposition method. In this method, the behavior of the LNG CCS is transformed to modal amplitude for each time step. In this way, the effect of continuous impact can be taken into account. Therefore, in FSI analysis cases, the mode superposition approach offers higher accuracy than does the impulse/space superposition approach.

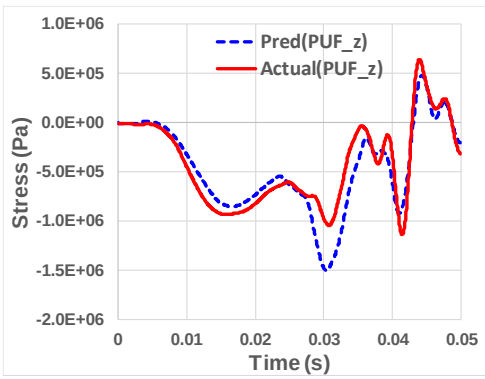

Case1

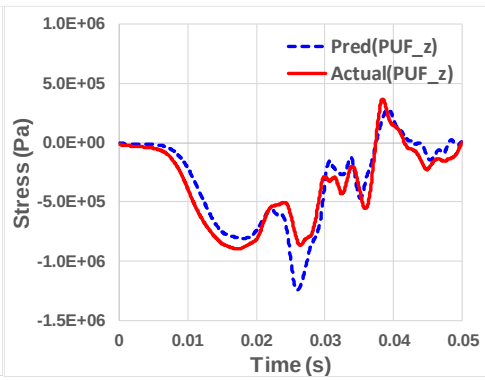

Case2

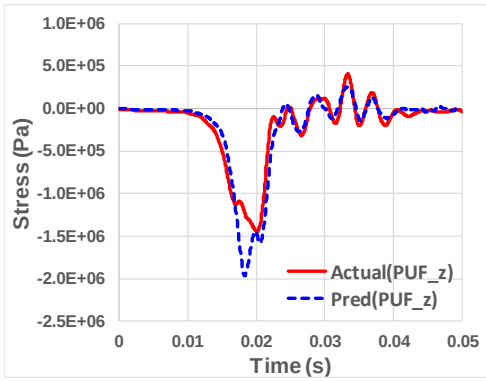

Case3

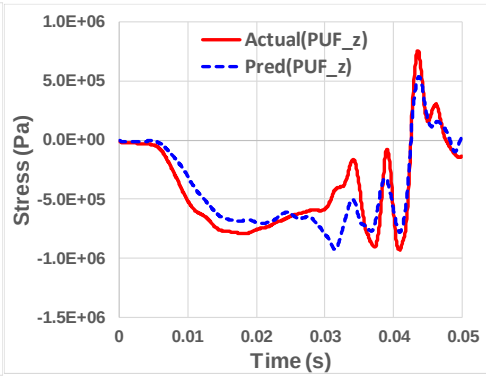

Case4

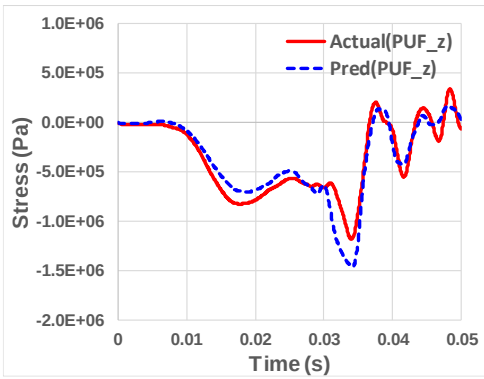

Case5

Fig. 111. Predicted stress response(PUF σ_z) using mode superposition method

Figures 112 to 117 plot the results for prediction of sloshing pressure and stress response for the 5 FSI analysis cases. The results are summarized for the peak and rising time of pressure and stress. The peak value and rising time were selected based on the first peak. The sloshing pressure could be predicted accurately enough with the impulse/space superposition method. In the case of stress response prediction, the accuracy could be increased by additionally applying the mode superposition method.

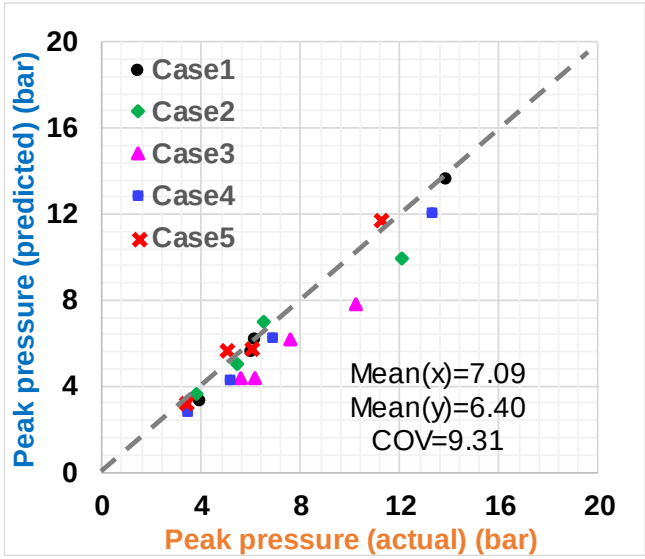

Fig. 112. Predicted sloshing pressure(peak)

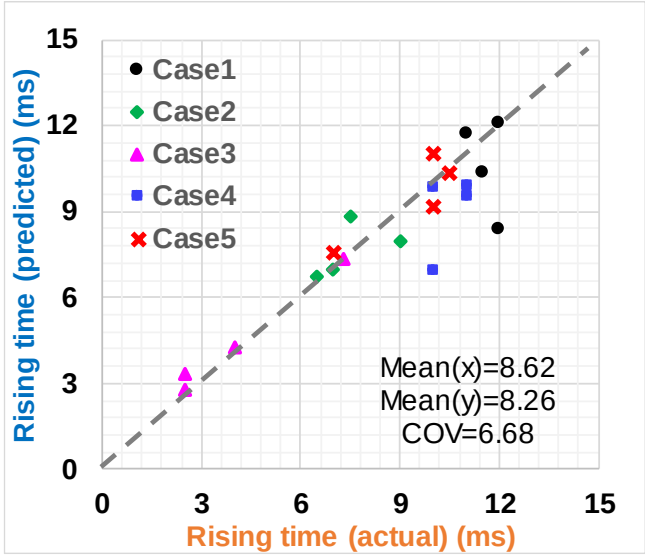

Fig. 113. Predicted sloshing pressure(rising time)

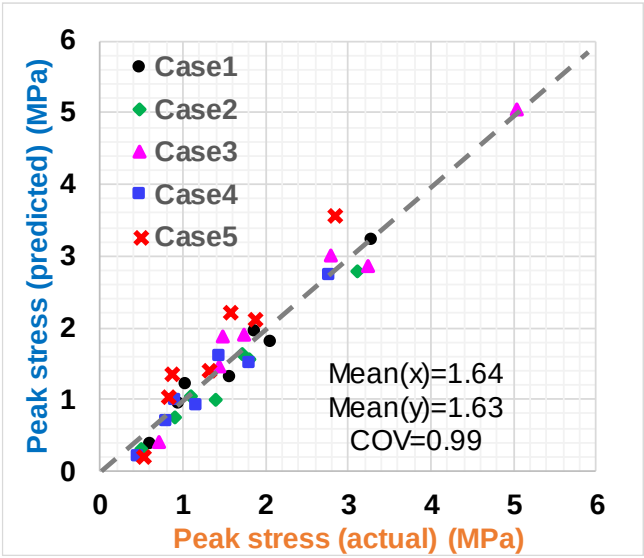

Fig. 114. Predicted stress response(peak) using impulse/space superposition method

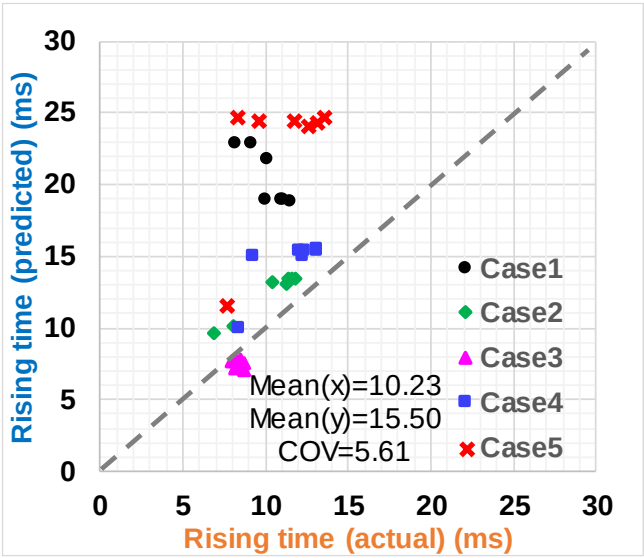

Fig. 115. Predicted stress response(rising time) using impulse/space superposition method

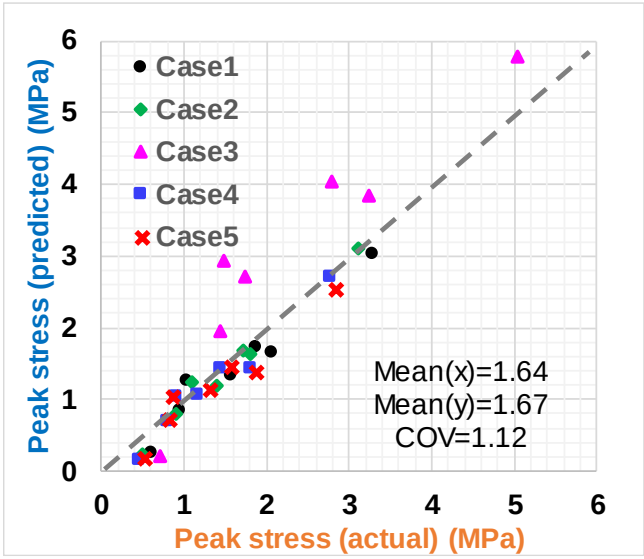

Fig. 116. Predicted stress response(peak) using mode superposition method

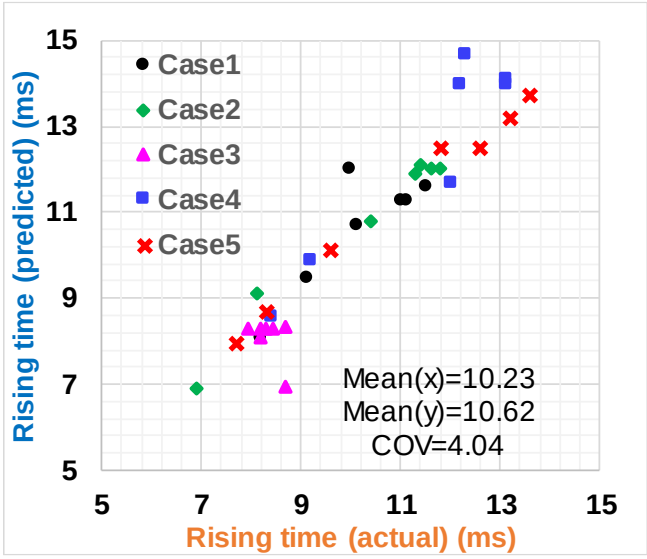

Fig. 117. Predicted stress response(rising time) using mode superposition method

4.4.3. Subdivision of pressure prediction region

When using four pressure prediction regions, there is a limit to accurately predicting the continuous pressure distribution generated on the membrane. Since the effect of pressure change is not considered in the selected pressure prediction regions, it is necessary to subdivide the regions for high-resolution pressure and stress response prediction. In order to minimize the numerical uncertainty caused by the presence of stiffeners, a total of 16 regions were selected as subdivided pressure prediction regions as illustrated in Fig. 118. After applying unit pressure to each of 16 regions (see Fig. 44), stress time histories were obtained at the 25 measurement points. From the calculated unit pressure stress responses and the measured stress responses by sloshing pressure, pressures for 16 selected regions can be calculated. In Eq. (23) to (25), K has a value of 16 and I has a value of 25.

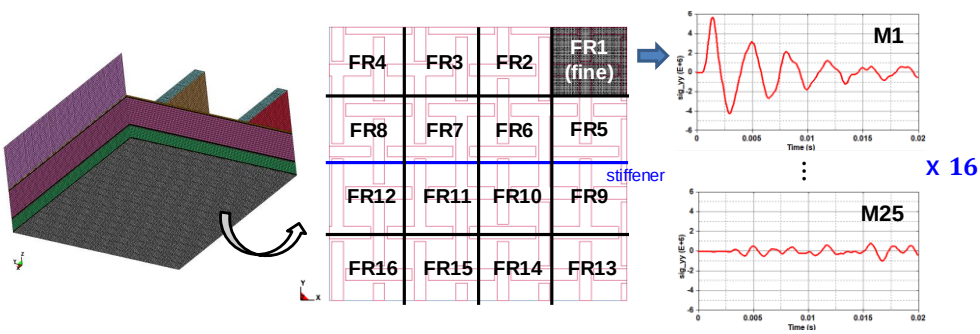

Fig. 118. Subdivided pressure prediction region

Two fluid-structure interaction analysis cases (Case1 and Case2 in Table 12) are adopted for application of subdivided pressure

prediction region. These two cases have non-zero deadrise angles which induce the continuous pressure distribution on membrane. Looking at Fig. 103 and Fig. 104, the accuracy of prediction for pressure occurrence time in R1 and R2 regions is low. This represents that the four pressure prediction regions are quite rough to consider the effect of continuous pressure distribution.

The results of applying subdivided pressure prediction region (a total of 16 pressure prediction regions) to Case1 are shown in Fig. 119. In each region, not only the peak pressure but also the pressure occurrence time are well predicted. The distribution of continuously generated pressure along the water spreading direction is well shown. Fig. 120 illustrates the stress responses of 25 measurement points calculated from the predicted pressures. It can be judged that the pressure prediction using the least square method for subdivided pressure prediction region is valid.

The results of applying subdivided pressure prediction region to Case2 are shown in Fig. 121. Like Case1, pressures are predicted well with high resolution. Fig. 122 shows the stress responses of 25 measurement points calculated from the predicted pressures. Compared with Fig. 109 (application of four pressure prediction region), the accuracy of pressure prediction is relatively high.

The hot spot stress responses in CCS can be calculated by applying the impulse/space superposition method to the predicted pressures in subdivided regions. In the two selected cases, the predicted stress responses using the impulse/space superposition method are shown in Fig. 123 and Fig. 124. Compared to the results

of applying the four pressure prediction regions (see Fig. 125 and Fig. 126), the prediction accuracy is relatively improved. In particular, the accuracy of the initial pressure rising period is greatly enhanced. It means that the continuous pressure distribution is well taken into account when applying the subdivided pressure prediction region. The error appearing in the second peak is due to the peak overestimation in FR3.

In summary, when the subdivided pressure prediction region is applied, the resolution of predicted pressures is increased, and thus the accuracy of stress responses through the impulse/space superposition method is also increased. The effect of continuous pressure distribution occurring in the actual sloshing phenomenon can be considered by applying subdivided pressure prediction region.

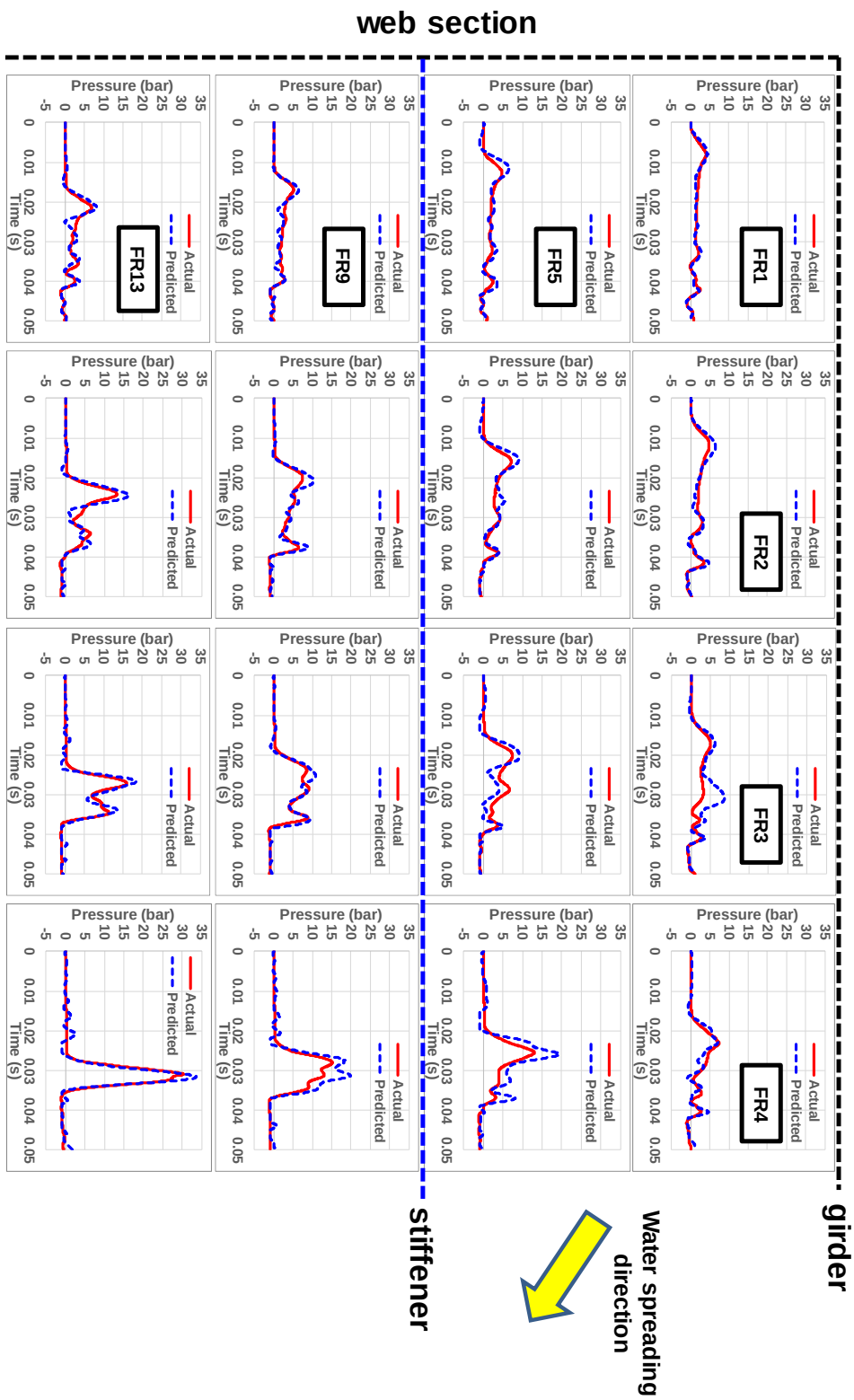

Fig. 119. Pressure prediction results(subdivided/Case1)

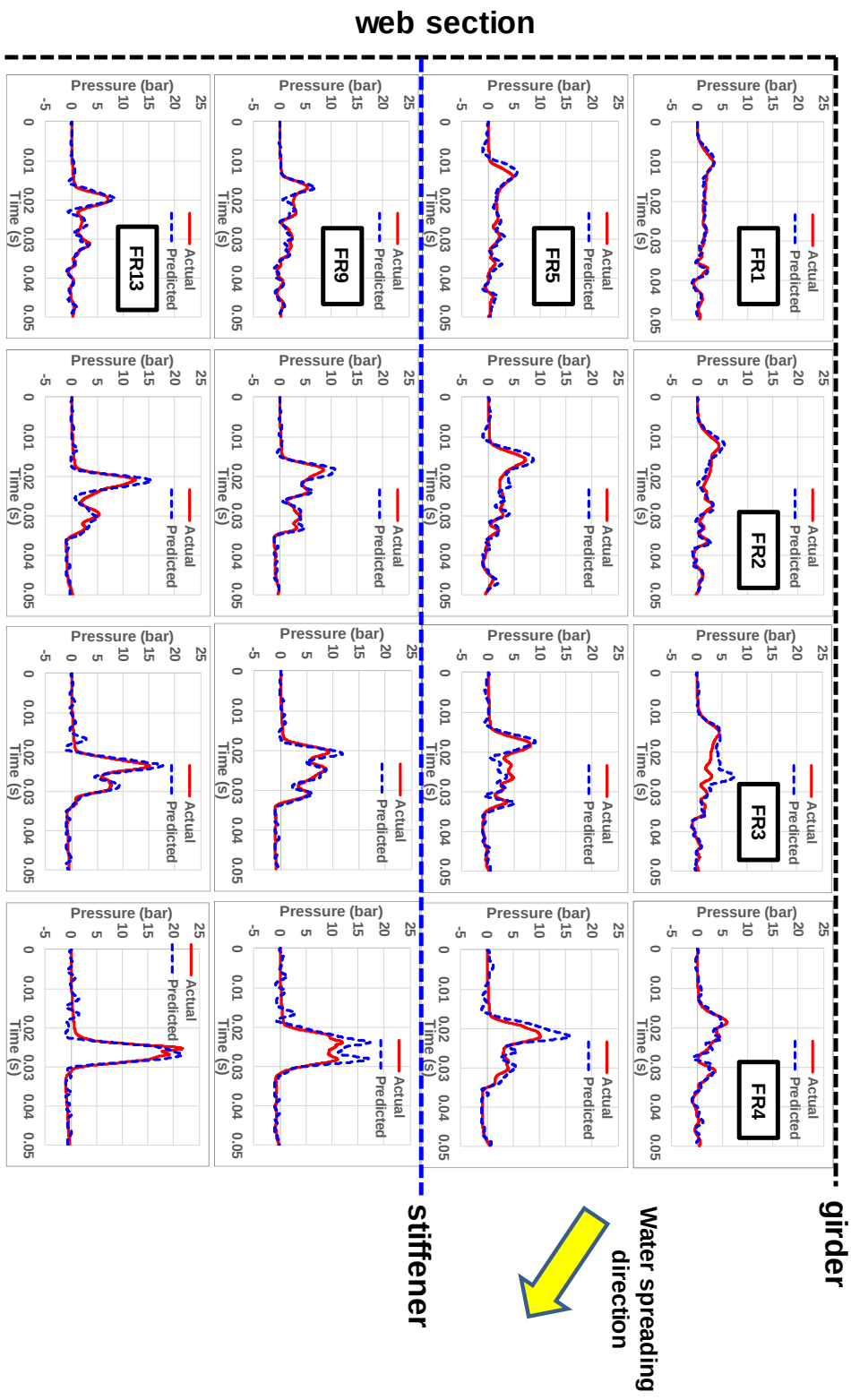

Fig. 120. Pressure prediction results(subdivided/Case2)

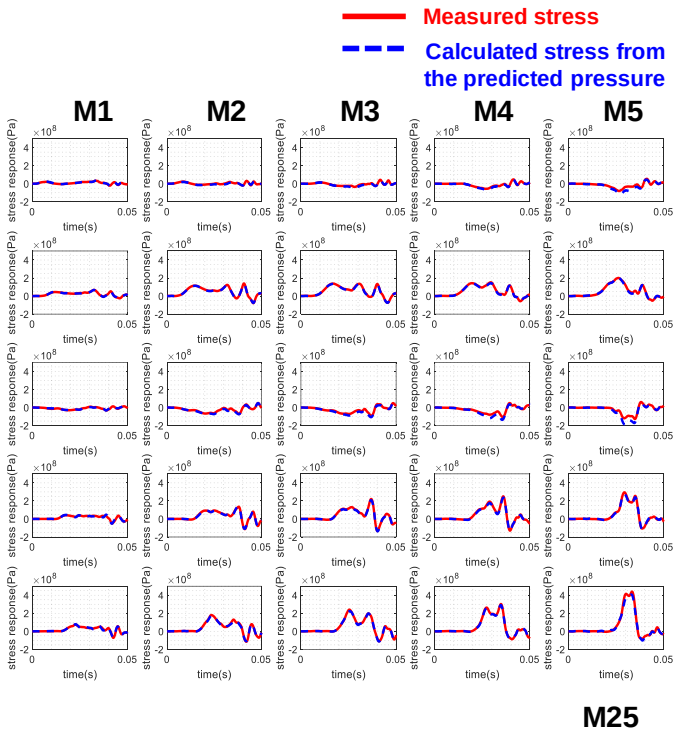

Fig. 121. Accuracy of pressure prediction(subdivided/Case1)

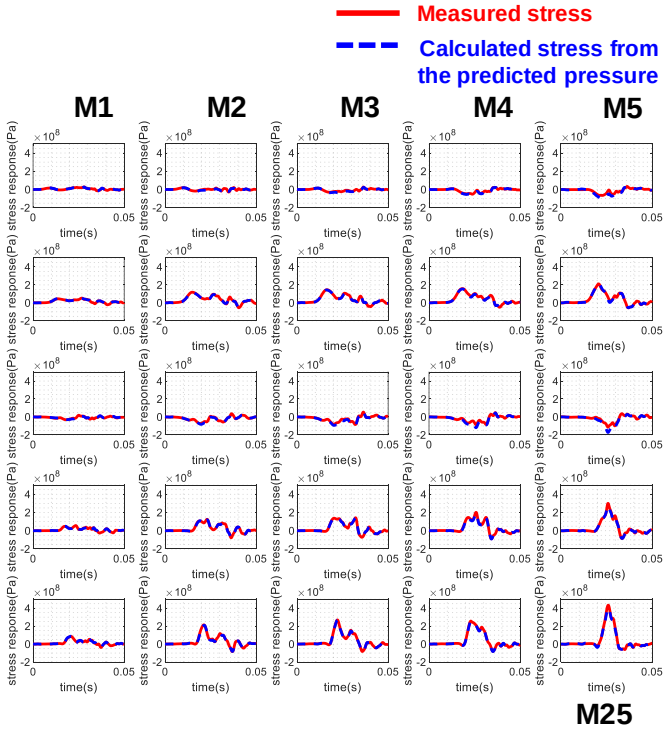

Fig. 122. Accuracy of pressure prediction(subdivided/Case1)

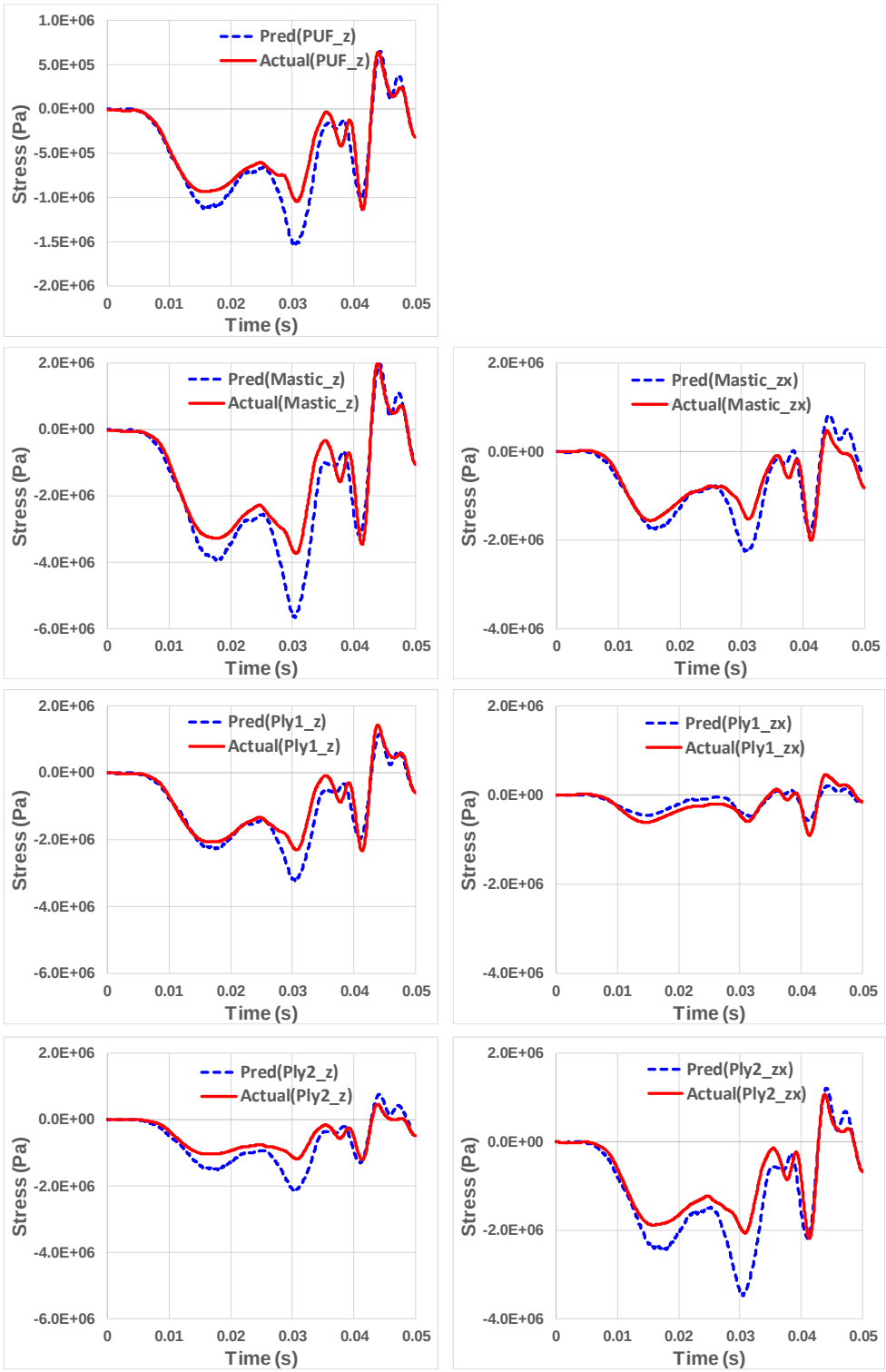

Fig. 123. Stress response prediction results(subdivided/Case1)

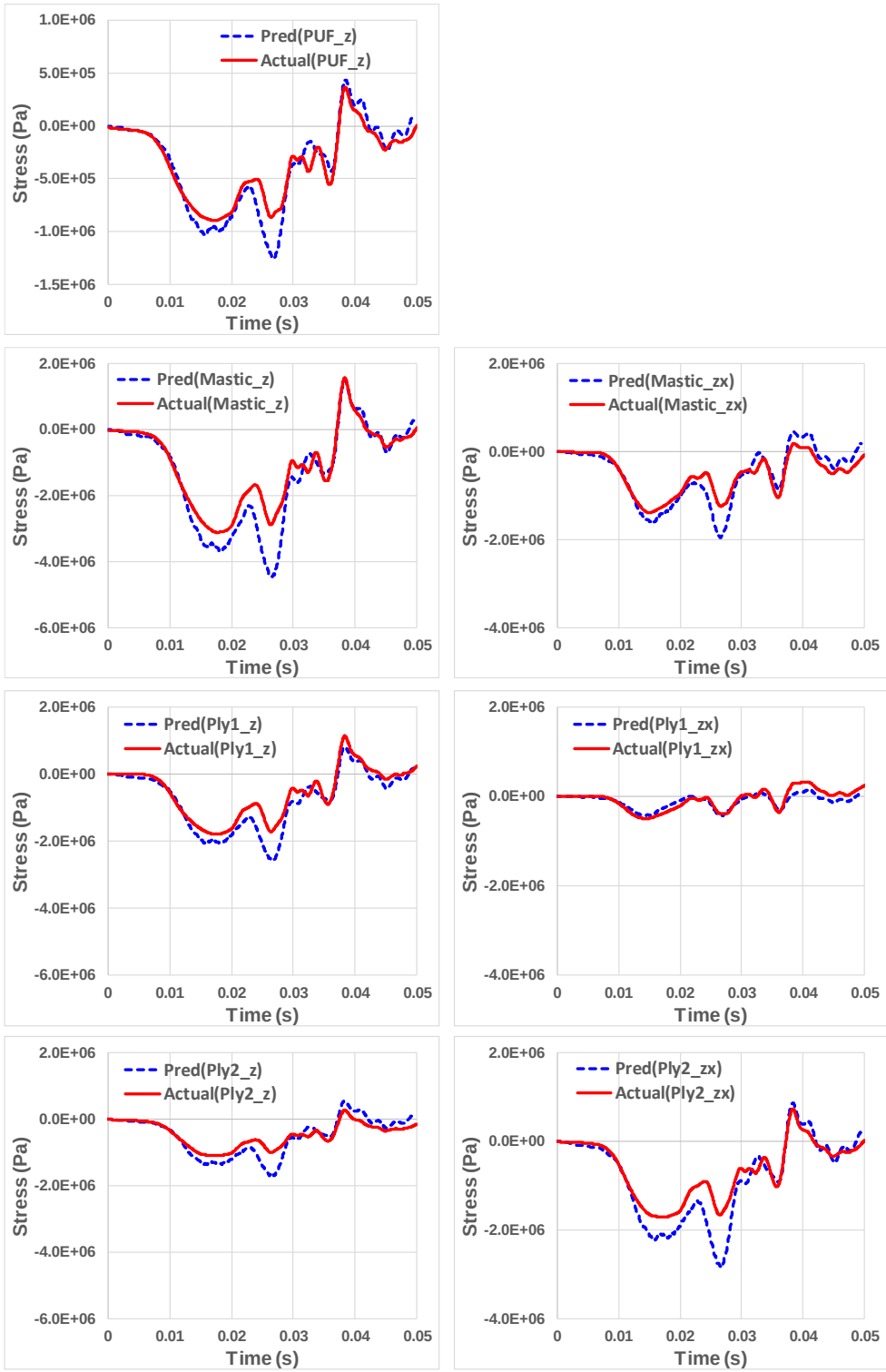

Fig. 124. Stress response prediction results(subdivided/Case1)

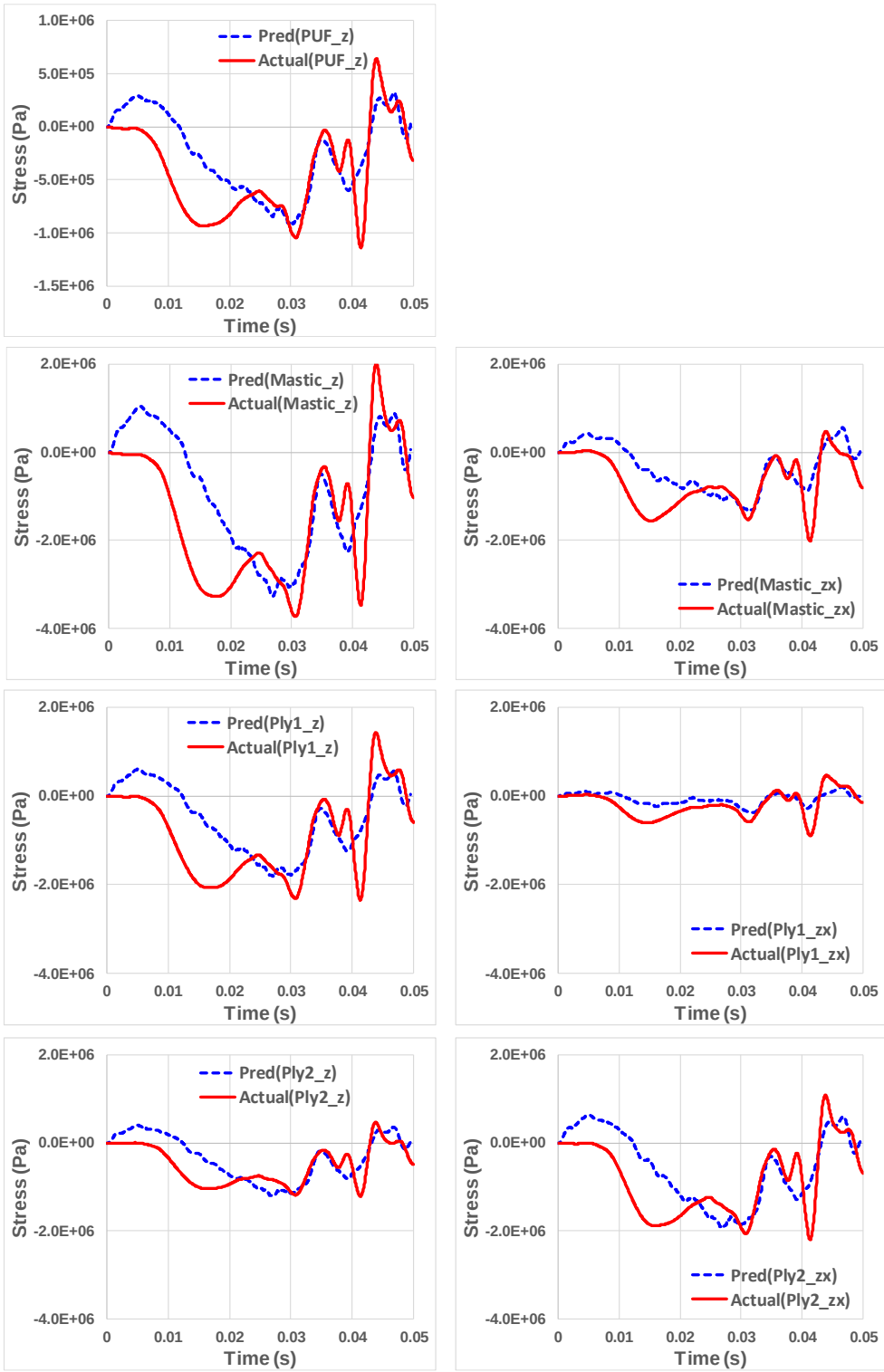

Fig. 125. Stress response prediction results (original/Case1)

(original: four pressure prediction regions)

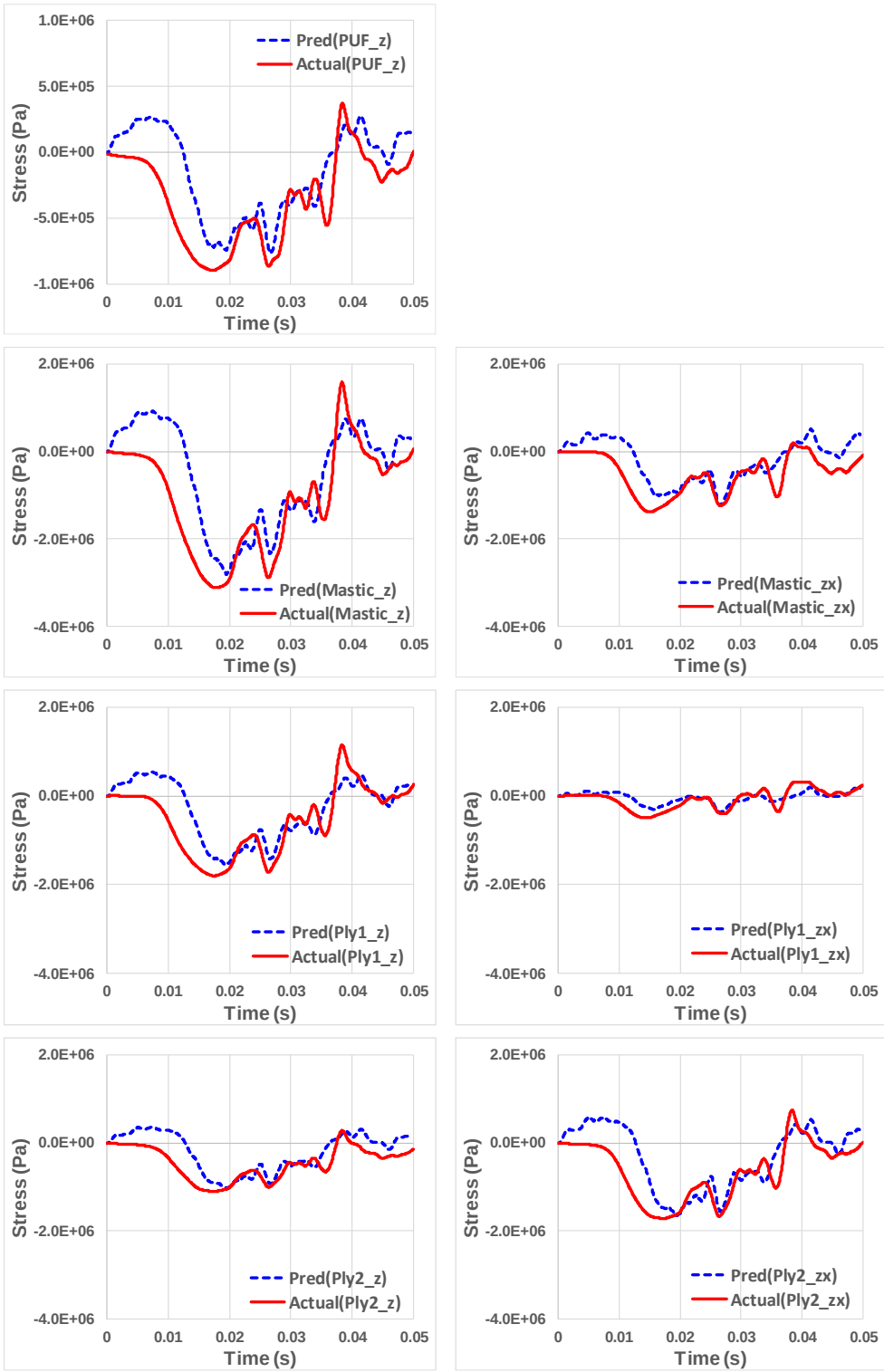

Fig. 126. Stress response prediction results(original/Case2)

(original: four pressure prediction regions)

4.5. Conclusions

Methods for prediction of sloshing pressure and hot spot stress response from stress response measured for the supporting structure of an LNG CCS were suggested. Using the impulse/space superposition method, sloshing pressure prediction was properly achieved. If the effect of pressure change within the area where the sloshing pressure is calculated is not large, the stress response prediction also has high accuracy. When a continuous pressure distribution occurs on the membrane, using subdivided pressure prediction region enhances the accuracy of pressure and stress response prediction. The mode superposition method can be effectively applied to stress response prediction. The specific conclusions drawn from the present research are as follows.

- The concept of space superposition was introduced to consider the effect of pressure applied to multiple regions at the same time. By linear superposition of the impulse superposition results calculated for each region, the structural response at a specific location can be calculated. This approach is named the impulse/space superposition method.
- The relationship between the measured stress response and the stress response by unit pressure can be expressed as the amplitude of sloshing pressure. A mathematical formulation for this was derived.
- The sloshing pressure corresponding to a given measured stress response and a unit pressure stress response can be

determined using the least square method. The lower-bound and curvature constraint conditions are applied for stability of results. Valid sloshing pressures are obtainable using the impulse/space superposition method.

- The mode superposition method also can be utilized to predict sloshing pressure. Appropriate modal amplitude can be estimated from the measured stress response through the mode truncation process. However, significant numerical uncertainty arises from numerical difference of modal amplitude (rendering use of mode superposition in pressure prediction difficult).

- Calculation of hot spot stress response for a predicted sloshing pressure can be carried out using the impulse/space superposition method. Even though the peak stress is estimated well, the effect of pressure change within the selected region is not considered. Application of subdivided pressure prediction region can improve the resolution(accuracy) of predicted pressure and stress response.

- From the modal amplitude, hot spot stress response can be calculated without the numerical difference process. The mode superposition method can additionally be applied for prediction of hot spot stress response. Under continuous impact conditions, the mode superposition method can increase the accuracy of hot spot stress response prediction.

Chapter 5. Summary of research

In the present study, a total of three topics were studied. First, the effect of the hydroelasticity effect on sloshing pressure was investigated and the LNG CCS strength assessment procedure considering the hydroelasticity effect was proposed. Second, the impulse superposition method was applied for screening of given design sloshing pressures. Finally, a method for predicting the sloshing pressure and stress in CCS from the measured stress data on inner deck was suggested.

5.1. Conclusions

The conclusions drawn from each chapter are as follows.

Chapter 2. Strength assessment of LNG CCS considering the hydroelastictiy effect

- The hydroelasticity effect of LNG CCS has a significant influence on the determination of peak value and rising time of sloshing pressures.
- LNG CCS strength assessment considering the hydroelasticity effect can be carried out from the water hitting simulations (FRP, FFC).
- Using the proposed empirical formula, the hydroelasticity effect can be taken into account without fluid-structure interaction analysis.

Chapter 3. Screening of design sloshing pressure using impulse superposition method

- The hot spot stress responses for given design sloshing pressures can be predicted using the impulse superposition method.
- The priority of design sloshing pressures can be determined.

Chapter 4. Prediction of sloshing pressure and LNG CCS structural response

- The sloshing pressure can be predicted well using the impulse/space superposition method.
- The process of numerical difference of modal amplitude contains large numerical uncertainty (hard to use mode superposition method in pressure prediction).
- When the subdivided pressure prediction regions are applied, the accuracy of pressure and stress response prediction is increased.
- The appropriate modal amplitude can be calculated from the mode selection process.
- Mode superposition method also can be used to predict stress response.

5.2. Limitations and future works

The limitations of the research are summarized as follows.

- Uncertainties in numerical based fluid-structure interaction

analysis

- Limited coverage and accuracy of the suggested empirical formulas for the consideration of the hydroelasticity effect
- Occurrence of inevitable uncertainty due to the noise of measurement data

Additional studies on the following issues are required.

- Improving the accuracy of fluid–structure interaction analysis through comparison with various experimental results
- Performing fluid–structure interaction analysis for more hitting cases and enhancing the accuracy of the empirical formulas
- Investigating on optimal sensor arrangement for sloshing pressure prediction and stress response prediction at given hot spots.

References

[1] Jeong H.W., Shim, W.J., 2017, Calculation of boil-off gas generation of KC-1 membrane LNG tank with high density rigid polyurethane foam by numerical analysis, Polish maritime research, 24, pp. 100-114.

[2] Jeong H.W., Kim, T.H., Kim, S.S., Shim, W.J., 2017, Thermal analysis of insulation system for KC-1 membrane LNG tank, Journal of Ocean Engineering and Technology, 31, No. 2, pp. 91-102.

[3] Jin, K.K., Oh, B.T., Kim, Y.K., Yoon, I.S., Yang, Y.C., 2013, An assessment of structure safety for basic insulation panel of KC-1 cargo containment system under sloshing load, Journal of the Korean Institute of Gas, 17, No.2, pp. 85-89.

[4] Kim, M.H., Lee, S.M., Lee, J.M., Noh, B.J., Kim, W.S., 2010, Fatigue strength assessment of Mark-III type LNG cargo containment system, Ocean Engineering, 37, pp. 1243-1252.

[5] Kimmoun, O., Ratouis, A., Brosset L., 2010, Sloshing and scaling: experimental study in a wave canal at two different scales, The 20th International Society of Offshore and Polar Engineering, Beijing, China.

[6] Kuo, J.F., Campbell, R.B., Ding, Z., Hoie, S.M., Rinehart, A.J., Sandstrom, R.E., Yung, T.W., Greer, M.N., Danaczko, M.A., 2009, LNG tank sloshing assessment methodology-The new generation, International Journal of Offshore and Polar Engineering, 19, No. 4, pp. 241-253.

[7] Brar, G.S., Singh, S., 2014, An experimental and CFD analysis of sloshing in a tanker, The 2nd International Conference on Innovations in Automation and Mechatronics Engineering, pp. 490-496.

[8] Bereznitski, A., 2001, Slamming: The role of hydroelasticity, International Shipbuilding Progress, 48, No. 4, pp. 333-351.

[9] Stenius, I., 2006, Finite element modelling of hydroelasticity in hull-water impact, Royal Institute of Technology, Stockholm, Sweden.

[10] American Bureau of Shipping, 2009, Strength assessment of membrane-type LNG containment systems under sloshing loads, Guidance notes.

[11] Bureau Veritas, 2011, Design sloshing loads for LNG membrane tanks, Guidance note, NI 554.

[12] DNVGL, 2016, Sloshing analysis of LNG membrane tanks, Class guideline, DNVGL-CG-0158.

[13] Llyod's Register, 2009, Sloshing assessment guidance document for membrane tank LNG operations, Additional design procedures.

[14] Jin, K.K., Yoon, I.S., Yang, Y.C., 2015, An effect of fluid-structure interaction for KC-1 cargo containment system under sloshing loads, The 25th International Society of Offshore and Polar Engineering, Hawaii, USA.

[15] Wang, B., Kim, J.W., 2007, Strength evaluation of LNG containment system considering fluid-structure interaction under sloshing impact pressure, The 26th International Conference on Offshore Mechanics and Arctic Engineering, California, USA.

[16] Lee, C.S., Cho, J.R., Kim, W.S., Noh, B.J., Kim, M.H., Lee, J.M., 2013, Evaluation of sloshing resistance performance for LNG carrier insulation system based on fluid-structure interaction analysis, International Journal of Naval Architecture and Ocean Engineering, 5, pp. 1-20

[17] Kim, W.S., Noh, B.J., Lee, H., Mravak, Z., Lauzon, J., Maguire, J.R., Radosavljevic, D., Kwon, S.H., Chung, J.Y., 2008, Fluid-structure interaction modeling, relating to membrane LNG ship cargo containment system, The 18th International Society of Offshore and Polar Engineering, Vancouver, Canada.

[18] Lee, S.G., Lee, I.H., Baek, Y.H., 2010, Wet drop impact response analysis of cargo containment system in membrane-type LNG carrier using FSI technique of LS-dyna, The 20th International Society of Offshore and Polar Engineering, Beijing, China.

[19] Faltinsen, O.M., 2000, Hydroelastic slamming, Journal of Marine Science and Technology, 5, pp. 49-65.

[20] Zeng, Q., 2014, MMALE numerical simulation for multi-material large deformation fluid flows, The Journal of Physics: Conference Series, 510 012047.

[21] Aquelet, N., Souli, M., Olovsson, L., 2006, Euler-Lagrange coupling with damping effects: Application to slamming problems, Computer Methods in Applied Mechanics and Engineering, 195, pp. 110-132.

[22] Cheon, J.S., Jang, B.S., Yim, K.H., Lee, H.S.D., Koo, B.Y., Ju, H.B., 2016, A study on slamming pressure on a flat-stiffened plate considering fluid-structure interaction, Journal of Marine Science and Technology, 21, pp. 309-324.

[23] Truong, D.D., Jang, B.S., Ju, H.B., Han, S.W., Han, S.K., 2019, A study on dynamic response of flat-stiffened plates to slamming loads considering fluid-structure interaction, Practical Design of Ships and Other Floating Structures, pp. 75-99.

[24] Truong, D.D., Jang, B.S., Ju, H.B., Han, S.W., 2020, Prediction of slamming pressure considering fluid-structure interaction. Part I: numerical simulations, Ships and Offshore Structures.

[25] Greenhow, M., 1987, Wedge entry into initially calm water, Applied Ocean Research, 9, pp. 214-223.

[26] Khabakhpasheva, T.I., Korobkin, A.A., 2013, Elastic wedge impact onto a liquid surface: Wagner's solution and approximate models, Journal of Fluids and Structures, 36, pp. 32-49.

[27] Luo, H., Wang, S., Soares, C.G., 2011, Numerical prediction of slamming loads on a rigid wedge subjected to water entry using an explicit finite element method, Advanced in Marine Structures, pp.41-47.

[28] Yoshikawa, T., Maeda, M., 2013, Numerical simulation of structural response under bow flare slamming load, Analysis and Design of Marine Structures, pp.25-33.

[29] LSTC, 2007, LS-dyna keyword user's manual version 971, Vol. 1.

[30] Chung, J.Y., Lee, J.H., Kwon, S.H., Ha, M.K., Bang, C.S., Lee, J.N., Kim, J.J., 2006, Wet drop test for LNG insulation system, The 16th International Society of Offshore and Polar Engineering, California, USA.

[31] Chuang, S.L., 1966, Experiments on Flat-bottom slamming, The Journal of Ship Research, 10.

[32] Ahn, K.S., Kwon, S.H., 2017, Experimental study on wedge slamming considering fluid-structure interaction, The Journal of Ocean Engineering and Technology, 31, pp. 22-27.

[33] Aquelet, N., Souli, M., 2003, Damping effect in fluid-structure interaction: Application to slamming problem, Pressure Vessels and Piping Conference, pp. 233-242.

[34] Olovsson, L., Souli, M., Do, I., 2003, LS-dyna – ALE capabilities, fluid-structure interaction modeling, Livermore Software Technology Corporation.

[35] Bogaert, H, Brosset, L., Kaminski, M.L., 2010, Interaction between wave impacts and corrugations of MarkIII containment system for LNG carriers: findings from the Sloshel project, International Society of Offshore and Polar Engineers, Beijing, China.

[36] Malencia, S., Diebold, L., Kwon, S.H., Cho, D.S., 2017, Sloshing assessment of the LNG floating units with membrane type containment system. Where we are?, Marine Structures, 56, pp. 99-116.

[37] Chen, H.C., 2011, CFD simulation of compressible two-phase sloshing flow in a LNG tank, The Ocean Systems Engineering, 1, pp. 31-57.

[38] Loots, E., Pastoor, W., Buchner, B., Tvetnes, T., 2004, The numerical simulation of LNG sloshing with ad improved volume of fluid method, The 23rd International Conference on Offshore Mechanics and Arctic Engineering, Vancouver, Canada.

[39] Arai, M., Karuka, G.M., Ando, H., 2017, Experimental and numerical study of sloshing and swirling in partially filled membrane-type LNG tanks, The 17th International Congress of the International Maritime Association of the Mediterranean, Lisbon, Portugal.

[40] Nho, I.S., Ki, M.S., Kim, S.C., 2011, A study on simplified sloshing impact response analysis for membrane-type LNG cargo containment system, The Journal of the Society of Naval Architects of Korea, 48, No.5, pp. 451-456.

[41] Lee, J.K., Ahn, Y.J., Kim, J.I, Kim, Y.H., 2019, Experimental study of phase transition in sloshing-induced impact in two-dimensional tank, The 35th International Workshop on Water Waves and Floating Bodies, Seoul, Korea.

[42] Nho, I.S., Ki, M.S., Kim, S.C., Lee, J.H., Kim, Y.H., 2017, Sloshing impact response analysis for insulation system of LNG CCS considering elastic support effects of hull structures, Journal of Ocean Engineering and Technology, Vol. 35(5), pp.357-363.

[43] Thomson, W.T., Dahleh, M.D., 1998, Theory of vibration with applications 5th edition, Prentice Hall.

[44] Park, C.J., Kim, Y.T., Noh, K.S., Oh, H.K., Choi, B.K., Lee, K.M., 2018, An enhanced comparative methodology for the structural safety assessment of membrane type CCS under sloshing loads, The 28th International Ocean and Polar Engineering Conference, Sapporo, Japan.

[45] Kim, S.Y., Kim, K.H., Kim, Y.H., 2012, Comparative study on model-scale sloshing tests, Journal of Marine Science and Technology, Vol. 17, pp. 47-58.

[46] Kim, Y.H., Kim, S.Y., Ahn, Y.J., Kim, K.H., Jeon, S.E., Suh, Y.S., Park, J.J., Hwangbo, S.M., 2013, Model-scale sloshing tests for an anti-sloshing blanket system, International Journal of Offshore and Polar Engineering, Vol. 23, No. 4, pp. 254-262.

[47] Kwon, C.S., Lee, Y.J., Kim, H.J., Lee, D.Y., 2019, Comparative experimental study on sloshing impact loads of LNG cargoes in membrane containment system of 160K LNGC, Journal of the Society of Naval Architects of Korea, Vol. 56, No. 2, pp. 103-108.

[48] Kim, S.Y., Kim, Y.H., Lee, J.H., 2017, Comparison of sloshing-induced pressure in different scale tanks, Ships and Offshore Structures, Vol. 12, No. 2, pp. 244-261.

[49] Ahn, Y.J., Kim, Y.H., Kim, S.Y., 2019, Database of model-scale sloshing experiment for LNG tank and application of artificial neural network for sloshing load prediction, Marine Structures, 66, pp.66-82.

[50] Bureau Veritas, 2011, Design sloshing loads for LNG membrane tanks, Guidance note NI 554.

[51] Loysel, T., Chollet, S., Gervaise, E., Brosset, L., Seze, P.E.D., 2012, Results of the first sloshing model test benchmark, The 22th International Offshore and Polar Engineering Conference, Rhodes, Greece.

[52] International Towing Tank Conference, 2017, Sloshing model tests, ITTC quality system manual.

[53] Karimi, M.R., Brosset, L., Ghidaglia, J.M., Kaminski, M.L., 2014, A study on conservation of Froude scaling for sloshing model tests, The 24th international Ocean and Polar Engineering Conference, Busan, Korea.

[54] Karimi, M.R., Kosinski, C., Brosset, L., 2013, Comparison of sloshing model test results at scales 1:10 and 1:40, The 23rd International Offshore and Polar Engineering, Alaska, USA.

[55] Bogaert, H., Leonard, S., Brosset, L., Kaminski, M.L., 2010, Sloshing and scaling: results from the sloshel project, The 20th International Offshore and Polar Engineering Conference, Beijing, China.

[56] Bunnik, T., Huijsmans, R., 2009, Large-scale LNG sloshing model tests, International Journal of Offshore and Polar Engineering, Vol. 19, No. 1, pp. 8-14.

[57] Bogaert, H., Kaminski, M.L., Brosset, L., 2011, Full and large scale wave impact tests for a better understanding of sloshing – results of the sloshel project, The 30th International Conference on Ocean, Offshore and Arctic Engineering, Rotterdam, Netherlands.

[58] Parthasarathty, N., Kim, H.J., Choi, Y.H., Lee, Y.W., 2017, A numerical study on sloshing impact loads in prismatic tanks under forced horizontal motion, Journal of the Korean Society of Marine Engineering, Vol. 41, No. 2, pp. 150-155.

[59] Xie, F.Z., Zhao, W.W., Wan, D.C., 2020, CFD simulations of three-dimensional violent sloshing flows in tanks based on MPS and GPU, Journal of Hydrodynamics, 32(4), pp. 672-683.

[60] Zhuang, Y., Wan, D., 2019, Numerical study on ship motion fully coupled with LNG tank sloshing in CFD method, International Journal of Computational Methods, Vol. 16, No. 6, 1840022.

[61] Ge, Z., Wang, B., Shin, Y.S., 2015, Sloshing simulations of various types of LNG tanks due to ship motions, The 11th International Conference on Computational Methods in Marine Engineering.

[62] Hwang, S.Y., Lee, J.H., 2021, The numerical investigation of structural strength assessment of LNG CCS by sloshing impacts based on multiphase fluid model, Applied Sciences, 11, 7414.

[63] Brizzolara, S., Savio, L., Viviani, M., Chen, Y., Temarel, P., Couty, N., Hoflack, S., Diebold, L., Moirod, N., Igleias, A.S., 2011, Comparison of experimental and numerical sloshing loads in partially filled tanks, Ships and Offshore Structures, Vol. 6, Nos. 1-2, pp. 15-43.

[64] Korean Register of Shipping, 2015, Guidance for assessment of sloshing load and structural strength of cargo containment system, GC-17-E.

[65] Lloyd's Register, 2004, Sloshing loads and scantling assessment, Structural Design Assessment.

[66] Chun, S.E., Hwang, J.O., Chun, M.S., Lee, K.M., Suh, Y.S., Hwangbo, S.M., White, N., Wang, Z.H., 2011, Direct assessment of structural capacity against sloshing loads using nonlinear dynamic FE analysis including hull structural interactions, The 21th International Offshore and Polar Engineering Conference, Hawaii, USA.

[67] Pillon, B., Marhem, M., Leclere, G., Canler, G., 2009, Numerical approach for structural assessment of LNG containment systems, The 19th International Offshore and Polar Engineering Conference, Osaka, Japan.

[68] Arswendy, A., Liasjoe, O., Moan, T., 2010, The effect of inner steel hull flexibility on the responses of the LNG containment system No.96 under static loads, The 20th International Offshore and Polar Engineering Conference, Beijing, China.

[69] Hwang, S.Y., Kim, S.C., Lee, J.H., Nho, I.S., 2014, Study on structural strength of Mark III type LNG cargo containment system by idealized triangular impulse load, Journal of Computational Structural Engineering Institute of Korea, 27(6), pp. 615-624.

[70] Wang, B., Shin, Y., 2009, Full-scale sloshing impact test and coupled fluid-structure FE modeling of LNG containment system, The 19th International Offshore and Polar Engineering Conference, Osaka, Japan.

[71] Lee, S.G., Kim, J.K., Nguyen, H.A., Nam, J.H., 2012, Structural safety assessment of LNGC Mark III membrane type CCS under sloshing impact loading, The 22nd International Offshore and Polar Engineering Conference, Rhodes, Greece.

[72] Cho, S.W., Jung, H.J., Kim, D.O., Lee, I.W., 1999, Efficient mode superposition method for non-classically damped systems, Journal of the Korean Society of Civil Engineers, Vol. 19, pp. 1-6.

[73] Rixen, D.J., 2001, Generalized mode acceleration methods and modal truncation augmentation, The 19th AIAA Applied Aerodynamics Conference.

[74] Miana, M., Legorburo, R., Diez, D., Hwang, Y.H., 2015, Calculation of boil-off rate of liquefied natural gas in Mark III tanks of ship carriers by numerical analysis, Applied Thermal Engineering,93(25), pp. 279-296.

감사의 글

2014년, 아무것도 모르는 제가 연구실에 처음 자리를 잡고 어색했던 기억이 어제 같은데 어느새 인턴 2년, 대학원 6년을 거쳐 박사 졸업을 앞두고 있다는 사실이 잘 믿겨지지 않습니다. 종심을 마친 후에는 그동안 많은 선배님, 후배님, 친구들 및 교수님과 함께 했던 시간들이 주마등처럼 지나가면서 새삼 뭉클한 기분이 들었습니다. 정말 많은 분들이 부족한 저의 졸업에 큰 도움을 주셨고 그 덕분에 무사히 박사 졸업을 완주할 수 있었던 것 같습니다. 이에 대한 감사를 조금이나마 아래와 같이 표현해보려고 합니다.

우선, 오랜 기간 동안 부족한 저의 발전에 많은 노력을 기울여 주신 장범선 교수님께 감사의 인사를 드립니다. 교수님 덕분에 다양한 연구 주제들에 대한 내용을 접할 수 있었으며 연구자로의 실력을 쌓을 수 있었습니다. 때때로 제가 힘들어할 때 진심 어린 조언을 주신 점 정말 감사드립니다. 교수님께서 보여주신 열정 및 노력은 제가 항상 본받으려고 노력하고 있습니다. 향 후에도 교수님의 가르침을 잊지 않겠습니다. 부족한 저의 연구 내용에 대해 섬세한 조언과 더불어 항상 좋은 말씀으로 용기를 불어넣어 주셨던 남보우 교수님, 김도균 교수님, 김유일 교수님, 권승님 박사님께도 진심 어린 감사를 드립니다. 덕분에 박사 연구 내용을 잘 정리할 수 있었습니다. 저도 언젠가는 교수님, 박사님과 같이 후배의 발전에 도움을 줄 수 있었으면 좋겠다는 마음을 품게 되었습니다.

제가 대학원 생활을 재미있게 보낼 수 있었던 원동력은 너무나도 좋은 연구실 구성원 분들이었습니다. 연구실의 초창기 멤버이자 1차 기둥이었던 (강)성욱형, (이)동범형, (임)기호형, (박)용만형에게 감사의 인사를 드립니다. 항상 긍정적 마인드로 제 연구뿐 아니라 연구실

생활에도 큰 도움을 주신 성욱형 감사드립니다. ESD 관련 연구에서 끝까지 책임감 있게 도움을 주신 동범형 감사드립니다. LNG CCS 연구에 있어서 아직까지도 많은 도움을 주시고 계신 기호형 감사드립니다. 박사 과정 중에 주신 기호형의 도움은 잊지 않겠습니다. 같이 충돌 연구 진행하면서 많은 도움을 주신 용만형에게도 감사드립니다.

더불어 비록 연구실 생활을 같이 하지는 못하였지만 항상 친한 동생처럼 대해 주신 (김)재웅형에게도 감사의 인사를 드립니다. 첫 사수로써 많은 도움을 주신 (천)진솔 누나에게도 감사의 인사를 드리며 매번 밝은 표정으로 저에게 용기를 주셨던 (김)해빈형에게도 감사를 드립니다.

연구실의 르네상스 시대를 이끌었던 뛰어난 4인의 88라인 연구자 분들((김)연림형, (김)현진형, (김)정두형, (최)준환형)에게도 진심 어린 감사의 인사를 드립니다. 가장 오랜 시간 연구실에서 같이 시간을 보내면서 연구 내적 및 외적 측면 모두에서 큰 도움을 받을 수 있었습니다. 끊임 없는 고민을 통해 스스로 연구의 돌파구를 찾고 항상 새로운 길을 개척해나가는 연림형에게 감사 및 존경의 인사를 드립니다. 노르웨이에서도 지금처럼 항상 원하는 방향대로 탄탄대로가 이어지길 바라겠습니다. Matlab의 마스터이자 진정한 학자의 모습을 보여주신 현진형에게도 역시나 감사 및 존경의 인사를 드립니다. 어디서나 인정받으실 실력을 가지고 계시기에 어디서든 좋은 결과가 이루어질 것을 믿어 의심치 않습니다. 연구를 수행함에 있어 제가 정말 닮고 싶은 모습 중 하나인 끈기를 보여준 정두형에게도 존경 및 감사의 인사를 드립니다. 뛰어난 추진력으로 현재 회사에서도 인정 받고 계신 모습에 대단함을 느끼고 있습니다. 끝까지 저의 졸업 메이트가 되어주신 준환형의 번뜩이는 아이디어는 항상 놀라웠고 이에 감사 및 존경의

인사를 드립니다. 뛰어난 능력에 노력까지 합쳐져서 앞으로도 계속 좋은 결과만 얻어질 것이라 확신합니다. 항상 형들의 밝은 미래를 기원하겠습니다.

같이 즐거운 연구실에서의 시간을 보낸 Truong 박사님, (류)강희형, (김)재동형, (이)경수형, (유)동현형, (이)재호형, (이)효철형에게도 감사의 인사를 드립니다. Truong 박사님과 같이 연구를 진행하면서 많은 교류를 할 수 있었습니다. 이에 감사의 인사를 드립니다. 항상 유쾌하고 밝은 에너지로 저의 연구실 생활에 큰 도움을 주신 강희형에게 결혼 축하와 더불어 감사의 인사를 드립니다. 같이 과제를 진행하면서 많은 배움과 노력하는 자세를 알려준 재동형에게 감사의 인사를 드립니다. 친 형처럼 항상 스스럼없이 대해주었으며 연구 과정에서 많은 조언을 주신 경수형에 감사의 인사를 드립니다. 연구실의 유머1번지이자 항상 조용하지만 알찬 연구력을 보여준 동현형에게도 감사의 인사를 드립니다. 인생의 선배로써 많은 대화를 나누어 주시고 실무적인 관점에서 큰 도움을 주신 재호형에게도 감사의 인사를 드립니다. 연구실에서 많은 추억을 만들며 생활의 큰 활력소가 되었던 (전)참수리호 선장님 이효철 소령님에게도 진심 어린 감사를 드립니다. 끝까지 노력하는 모습이 존경스러웠으며 곧 앞둔 결혼도 진심으로 축하드립니다.

친구로써 연구실 생활의 지지대가 되어준 (감)민주양, (윤)란희양, (박)정호군, (유)채원양에게도 많은 감사를 드립니다. 연구 내용에 대해 같이 공유하면서 많은 조언과 도움을 준 민주에게 감사를 표합니다. 같이 수업 들으면서 이론적인 부분에 대해 서로 교류한 현 자동차 마스터 란희에게도 감사를 표합니다. 학부생 시절부터 서로 재밌게 지낸 정호에게도 감사를 표합니다. 같이 여러 프로젝트를 수행하면서 많은 우여곡절을 공유한 채원이에게도 진심 어린 감사를 표합니다. 덕분에 큰

힘이 되었고 더욱 재미 있는 연구실 생활을 보낼 수 있었습니다. 곧 앞둔 결혼 진심으로 축하합니다.

현재 같이 연구실 생활을 이어가고 있는 (한)상웅 선임님, (김)경은 선생님, (양)준혁군, (전)호현군, (린)위야오군, (박)동인군 및 얼마 전 졸업한 (이)대영군에게도 감사의 인사를 드립니다. 영원한 연구실의 동반자이자 매번 어른으로써 진심 어린 인생의 조언을 주신 선임님께 진심으로 감사드립니다. 덕분에 박사 졸업 과정을 잘 마칠 수 있었습니다. 매사에 긍정적인 마인드를 닮으려고 노력하고 있습니다. 조용히 연구실의 모든 행정 관련 업무를 완벽히 처리해주시는 경은 선생님께도 감사의 인사를 드립니다. 항상 친절하게 도움을 주셔서 정말 감사드립니다. 앞으로 연구실의 미래를 이끌어나갈 준혁, 호현, 린, 동인이에게 감사와 함께 응원의 말을 전합니다. 짧은 시간이었지만 뛰어난 능력을 보여주는 모습들이 놀라웠습니다. 지난 겨울 같이 졸업 동반자였던 대영이에게도 감사를 표합니다. 뛰어난 연구 능력에 감탄을 하였고 졸업 후 정한 진로에서도 큰 성공이 있기를 바랍니다.

마지막으로 저의 인생에서 가장 소중한 존재인 가족에게 무한한 감사를 드립니다. 평생 동안 묵묵히 저의 선택을 지지하고 응원해준 영원한 조북이, 저희 엄마(조수연 여사님)에게 누구보다 큰 감사의 인사를 전합니다. 항상 몸 건강 관리 잘해서 지금처럼 계속 행복한 생활을 이어 나간다면 더 바랄 것이 없습니다. 앞으로는 보다 자랑스러운 아들이 될 수 있도록 노력하겠습니다. 더불어 현재 조카 안서하양의 육아에 정신이 없을 누나(주한솔님)와 매형(안광석님)에게도 항상 감사한 마음을 가지고 있다고 말하고 싶습니다. 항상 허물 없이 지내면서 든든한 저의 지원군이 되어주기에 제가 힘든 시간들을 이겨낼 수 있었습니다. 우리의 귀염둥이이자 분위기메이커 안서하양의 무한한 행복을 기원합니다. 또한 제가 당당하게 생활할 수 있는 원동력이

되어준 할머니(박광연 여사님)에게도 평생 감사한 마음을 가지고 있습니다. 지금과 같이 건강 하신 모습으로 꾸준히 저희와 즐거운 나날을 보내는 미래를 기대합니다. 제 박사논문을 가족에게 바치며 앞으로도 모두 항상 행복한 나날들을 보내기를 진심을 담아 기원합니다.

이 외에도 저의 박사 졸업에 도움을 주신 모든 분들께 감사의 인사를 드립니다.

주한백 올림

초록

환경 규제가 강화되면서 LNG 및 LNG 운반선에 대한 수요가 증가하고 있다. LNG CCS(LNG Cargo Containment System)는 LNG 운반선에서 가장 중요한 설비 중 하나이며, 현재까지 많은 멤브레인 유형의 LNG CCS가 개발되어 왔다. 전통적으로 설계 슬로싱 압력은 슬로싱 모델 테스트 결과에 일련의 통계적 과정을 적용함으로써 얻어지며 이러한 설계 슬로싱 압력을 활용하여 LNG CCS의 강도 평가를 수행한다. 슬로싱 모델 실험에서는 실제 모델이 아닌 평평하고 단단한 판을 사용하여 LNG CCS를 나타내므로 유탄성 효과를 고려할 수 없다. 본 연구에서는 유체-구조 상호작용 시뮬레이션을 통해 슬로싱 압력에 대한 유탄성 효과를 알아본다. 일련의 유체 타격 시뮬레이션으로부터 슬로싱 압력에 대한 유탄성 효과가 상당한 영향을 미치는 것을 확인하였다. 본 논문에서는 이를 바탕으로 유탄성 효과를 고려한 LNG CCS 강도 평가 절차를 제안한다. 슬로싱 모델 실험에서 산출되는 설계 슬로싱 압력은 그 수가 많다. 모든 설계 슬로싱 하중들에 대해 LNG CCS 강도 평가를 수행하기 위해서는 상당한 시간이 소요된다. 특히 유탄성 효과를 고려하기 위하여 유체-구조 상호작용 시뮬레이션을 적용할 경우 그 부담은 더욱 커진다. 따라서 주어진 설계 슬로싱 압력의 중요성을 미리 판단하여 LNG CCS 구조 설계에 적용하는 설계 슬로싱 압력의 수를 줄이는 과정을 제안한다. 이 과정에는 임펄스 중첩 방법을 적용하였다. 실제 LNG 탱크에서 발생하는 슬로싱 압력의 이력이나 단열 패널의 응력 응답 이력에 대한 정보가 아직 충분하지 않다. 멤브레인 배면 혹은 단열 패널 내부에 센서를 직접 부착하는 것은 현실적으로 어렵다. 반면에 LNG CCS를 지지하는 선체 구조의 응답을 측정하는 것은 충분히 가능하다. 이렇게 측정된 LNG CCS 지지구조물의

응력데이터로부터 슬로싱 압력 및 단열 패널에서 발생되는 응력 값을 예측하는 방법을 제안한다. 예측된 슬로싱 압력 결과는 실제 발생되는 슬로싱 압력의 수준을 이해하는데 도움이 된다. 이 결과로부터 LNG CCS 설계에 사용되는 설계 슬로싱 압력의 타당성도 판단할 수 있다. 예측된 단열 패널의 응력 응답을 사용하여 실시간으로 LNG CCS의 구조 건전성 모니터링을 수행할 수 있다.

Keywords: LNG CCS, sloshing pressure, hydroelasticity, fluid-structure interaction, strength assessment, structure monitoring.

Student Number: 2016-21141